



**TECHNISCHE
UNIVERSITÄT
DRESDEN**



Leibniz-Institut
für Festkörper- und
Werkstoffforschung
Dresden

Scanning tunneling microscopy on low dimensional systems: dinickel molecular complexes and iron nanostructures

Dissertation

zur Erlangung des wissenschaftlichen Grades

Doctor rerum naturalium (Dr. rer. nat.)

der Fakultät Mathematik und Naturwissenschaften

der Technischen Universität Dresden

vorgelegt im Februar 2016 von

Christian David Salazar Enríquez

Geboren am 5. September 1986 in Pasto-Kolumbien

1. Gutachter: Prof. Dr. Bernd Büchner
2. Gutachter: Prof. Dr. Berthold Kersting

Eingereicht am: 29. Februar 2016
Disputation am: 28. September 2016

Abstract

This thesis contains experimental studies on low dimensional systems by means of scanning tunneling microscopy (STM). These studies include investigations on dinickel molecular complexes and experiments on iron nanostructures used for the implementation of the spin-polarized scanning tunneling microscopy technique at the IFW-Dresden. Additionally, this work provides detailed information of the experimental technique (STM), from the theoretical background to the STM-construction, which was part of this doctoral work.

Molecular anchoring and electronic properties of macrocyclic magnetic complexes on gold surfaces have been investigated by mainly scanning tunneling microscopy and complemented by X-rays photoelectron spectroscopy. Exchange-coupled macrocyclic complexes $[\text{Ni}_2\text{L}(\text{Hmba})]^+$ were deposited *via* 4-mercaptobenzoate ligands on the surface of Au(111) single crystals. The results showed the success of gold surface-grafted magnetic macrocyclic complexes forming large monolayers. Based on the experimental data, a growth model containing two ionic granular structures was proposed. Spectroscopy measurements suggest a higher gap on the cationic structures than on the anionic ones. Furthermore, the film stability was probed by the STM tip with long-term measurements. This investigation contributes to a new promising direction in the anchoring of molecular magnets to metallic surfaces.

Iron nanostructures of two atomic layers and iron-coated tungsten tips were used in order to implement the spin-polarized scanning tunneling microscopy technique at the IFW-Dresden. First of all, a systematic study of the iron growth, from sub-monolayers to multilayers on a W(110) crystal is presented. Subsequent to the well-understanding of the iron growth, the experiments were focused on revealing, for the first time at the IFW-Dresden, the magnetic inner structure of iron nanostructures. The results evidently showed the presence of magnetic domains of irregular shapes. Furthermore, SP-STM probed the bias voltage dependence of the magnetic contrast on the iron nanostructures. This technique opens up a new powerful research line at the IFW-Dresden which is promising for the study of quantum materials as molecular magnets and strongly correlated systems.

Table of Contents

1	Introduction	6
2	Experimental technique	10
2.1	Introduction to scanning tunneling microscopy	10
2.2	Concept of scanning tunneling microscopy	12
2.3	Quantum tunneling	13
2.4	Tunneling current.....	15
2.5	Scanning tunneling microscopy	19
2.6	Scanning tunneling spectroscopy	20
2.6.1	The lock-in technique.....	21
2.6.2	Energy resolution of STS at finite temperatures	23
2.7	STM and STS data.....	24
2.8	Spin-polarized STM/STS.....	25
3	Instrumentation.....	30
3.1	General considerations for the two used microscopes	30
3.1.1	The coarse approach system.....	30
3.1.2	The tube scanner.....	31
3.1.3	Electronics basics.....	32
3.2	Variable-temperature STM system (VT-STM)	33
3.2.1	Overview	33
3.2.2	Important working steps	36
3.2.3	Problems.....	37
3.3	Low-temperature STM system (LT-STM).....	42
3.3.1	Overview	42
3.3.2	Important working steps	45
3.3.3	LT-STM for Spin-Polarized STM.....	46
4	Substrates and tips: preparation.....	47
4.1	Substrates.....	47
4.1.1	Highly oriented pyrolytic graphite (HOPG)	47

4.1.2	Au(111).....	50
4.1.3	W(110).....	51
4.2	Tips.....	53
4.2.1	Tungsten (W) tips	53
4.2.2	Platinum-iridium (Pt/Ir) tips	55
4.2.3	Iron coated tungsten (Fe/W) tips	56
4.2.4	Chromium (Cr) tips	57
5	<i>Dinickel molecular complexes on Au(111)</i>.....	59
5.1	Motivation	59
5.2	Synthesis of molecular complexes.....	61
5.3	Characterization	62
5.3.1	Electrochemistry	62
5.3.2	Magnetic properties	63
5.4	Chemisorption on gold surfaces: first hints.....	65
5.4.1	Contact angle measurements	65
5.4.2	XPS studies.....	66
5.5	Results: Monolayers of the complex [Ni₂L(Hmba)]ClO₄ on Au(111).....	68
5.5.1	Sample preparation.....	68
5.5.2	Monolayer characterization <i>via</i> core level spectroscopy (XPS)	69
5.5.3	Monolayer characterization <i>via</i> scanning tunneling microscopy (STM)	70
5.6	Conclusions.....	81
6	<i>Iron nanostructures on W(110)</i>.....	83
6.1	Motivation	83
6.2	Iron nanostructures: physical properties	83
6.2.1	Iron nanowires	84
6.2.2	Iron islands	88
6.3	Results I: Growth of iron nanostructures on W(110).....	91
6.4	Results II: Spin-polarized tunneling on iron nanostructures: magnetic imaging.....	96
6.5	Conclusions.....	104
7	<i>Summary and outlook</i>.....	105
	<i>Bibliography</i>.....	107

1 Introduction

From ancient times, science has played a fundamental role in the development of mankind. For instance, the industrial revolution, which began in the 18th century, was highly benefited by the great knowledge of basic sciences which was applied to industry. At that time, the agrarian and handicraft economy was changed to one that was dominated by industry and machine manufacture. The technological changes included mainly: i) the use of new basic materials, chiefly iron and steel, and ii) the use of new energy sources, including fuels and motive power, such as coal, the steam engine, electricity, and petroleum. These two aspects led to the invention of new machines that permitted increased production with a smaller expenditure of human energy, as well as important developments in transportation and communication [1]. During the 19th century, mankind was rapidly changing according to technological advances which included the invention of useable products such as the steam engine, the locomotive, the telephone, the telegraph and the light bulb, among others [2]. At the beginning of the 20th century, the development of a new science (i.e. physics, chemistry) that focused on the understanding of the internal structure of matter, e.g. the function and organization of atoms and molecules, marked an important shift for the later invention of amazing products such as computers, which have changed our lives. However, all of these incredible products which mankind has benefited from will soon be replaced by others which may be built thanks to our extensive knowledge of the microscopic and nanoscopic world.

“There’s plenty of room at the bottom” was the name of the famous lecture given by Professor Richard Feynman in 1959 at the California Institute of Technology. This prophetic talk showed the imminent entry into a new world, the world of nanotechnology. Richard Feynman, inspired by how biological systems work, suggested that humanity will be able to build machines smaller than biological cells with the same functionality, in the near future. “The principles of physics do not speak against the possibility of maneuvering things atom by atom. It is not an attempt to violate any laws; it is something, in principle, that can be done; but in practice, it has not been done because we are too big”, said Feynman [3]. The revolutionary idea of making usable things at the size of molecules, e.g. the nanometer scale (10^{-9} m), opens the possibility to find interesting applications as well as novel solutions to current problems faced by humanity.

As it was done during the industrial revolution in the 18th century, a new class of materials is being designed nowadays. Such materials are based on the fine control of their internal structure and are commonly called nanostructured materials [4]. The nanomaterials are classified according to their dimensionality in: i) zero-dimensionality, such as quantum dots, clusters, and nanoparticles, ii) one-dimensionality, such as nanotubes and nanowires, iii) two-dimensionality, such as thin films, monolayers, and iv) three-dimensionality, such as nanostructured powders, ceramics with nanometric crystalline size, among others [5–9]. The shrunk materials at nanoscale might exhibit completely different properties to those exhibited at the macro scale (μm , mm , cm , m , km). As a typical example, gold is considered an inert material in the macro scale; in fact, it does not corrode or tarnish. In chemistry, gold would be an inappropriate material to use as a catalyst for chemical reactions. However, gold particles of about 5 nm can act as a catalyst that can do things like oxidizing carbon monoxide. Furthermore, gold changes its color depending on the particle-size; a particle of about 90 nm will absorb colors on the red and yellow end of the color spectrum, making the nanoparticle appear blue-green. But a particle of about 30 nm absorbs blues and greens, resulting in a red appearance [10–12]. All of these and others more fascinating properties of matter, are consequence of the singular quantum effects and surface phenomena exhibited at the nanoworld.

Among all the fields which have been so far explored in the nanoworld, magnetism is especially important. This has a lot of barely understood phenomena and potential applications from data storage to quantum computing [13,14]. In order to know how magnetism works at the nanoscale it is indispensable to study nanometer scale systems, where changes in size or structure might have large effects on the magnetic properties. Additionally, the current demand of higher data storage and processing capacity has increased the need for new usable nanostructured materials as well as capable techniques to work in the nanoworld.

Single molecular magnets (SMM) are a class of molecules that at very low temperature behave like a magnet, showing permanent magnetization and a hysteresis loop coupled with quantum phenomena, e.g. tunneling, that is not possible to find in traditional magnets [15]. The interest in SMMs has grown tremendously in recent years due to their potential applications in high-density information storage devices, Q-bits in quantum computing, and in spin-valves devices, among others [16–20]. SMMs show slow relaxation of their magnetization vector below a certain temperature (blocking temperature) [21], and this is a reason for their promising use in Spintronic devices as chemisorbed or physisorbed on conducting surfaces or electrodes. However, two major problems need to be solved in order to build useful devices. The operation temperature of the SMMs is still far below room temperature and a controlled adsorption and organization on solid-surfaces is desired. Chemists have taken important steps to design

interesting SMMs, which require relatively high temperature for the reversal of their magnetization. Some examples are: the Mn_{12} family of complexes, lanthanide based SMMs, e.g. the Dy_5III cluster, and a monomeric $Tb(III)$ complex with phthalocyaninate ligands, among others [22–25]. However, many of these poly-nuclear clusters are very fragile from a redox point of view and undergo some structural transformations upon adsorption. The surface-molecule interaction in many cases leads to the loss of the SMM characteristics and it has been witnessed in a variety of cases including the archetypal Mn_{12} SMM [26]. In this framework, experimental and theoretical studies at the nanoscale are extremely desired in order to judge the functionality and reliability of new promising SMMs.

One of the finest tools for studying the nanoworld is the scanning tunneling microscopy (STM) [27,28]. This technique uses an extremely sharp tip, ideally just one atom at the tip end, to interact with a sample under investigation through a tiny electronic current (nanoampers or picoampers). The current is produced between tip and sample due to a quantum phenomenon that is so-called tunneling. By moving the tip over the sample, it is possible to reveal the surface “topography” and additionally to probe electronic properties with spatial resolution of angstroms. Such a nice tool lets us have a direct look at the nanoworld and helps us with the understanding of different physical systems such as atoms, molecules, thin films and others in terms of their structural and electronic properties. The experiments with scanning tunneling microscopy are in general challenging and require special instruments to provide the optimal conditions for a successful data acquisition. Among them, the ultra-high vacuum environment of the order of 10^{-10} mbar and low-temperature setups which allow temperatures of milli-Kelvins up to few Kelvins. Originally, the scanning tunneling microscopy was not able to study magnetism; however, it was adapted to study surface magnetism by using magnetic probe tips [29]. The contrast mechanism of this so-called spin-polarized scanning tunneling microscopy (SP-STM) relies on the tunneling magneto-resistance effect, i.e. the tip-sample distance as well as the differential conductance which depend on the relative magnetic orientation of tip and sample [30]. Although the SP-STM technique was demonstrated for the first time in the 90s, just a few groups in the world have been successful in implementing this technique. The challenge relies on the extremely unperturbed environment demanded to detect spin currents originated from nanomagnets. However, nowadays the current research both in basic and applied science needs the capability of such a technique to push the knowledge forward in order to understand and control the nanoscale structural, electronic and magnetic properties of the materials for the 21st century.

This thesis addresses the investigation of surface grafting paramagnetic molecules by means of STM, and describes the implementation of SP-STM at the IFW-Dresden,

providing the basis for resolving unique magnetic properties at the nanoscale. In this sense, the work is organized as follows:

Chapter 2 introduces the basics of scanning tunneling microscopy and spectroscopy (STM/STS) as well as spin-polarized STM/STS. Additionally, in this chapter the acquisition procedure of images and spectroscopic data is explained.

Chapter 3 gives a detailed description of the different devices employed in the experiments. Considering that two different STM-devices were used, the common operating characteristics as well as the special features of both and their contributions to this work are described.

Chapter 4 describes the preparation of different standard samples employed as calibration samples for the STM experiments as well as substrates which host the low dimensional systems under scrutiny. Furthermore, in this chapter the preparation of common tips for STM and novel tips for SP-STM is described.

Chapter 5 is one of the main parts of this thesis; at the beginning of the chapter a motivation of the investigation on organic magnetic materials is presented. It continues with an introduction of the molecular complexes of interest, from their synthesis, carried out by Prof. Kersting's group at the university of Leipzig, to the first deposition experiments on a gold surface. The next part is a detailed study of dinickel molecular complexes deposited on gold single crystals by means of STM/STS. In this study the structural conformation of the organic molecules forming a monolayer as well as the electronic characteristic exhibited once they are in contact with the gold surface is achieved. Furthermore, the tip interaction with the monolayers is evaluated.

Chapter 6 is the other main part of this thesis. It starts with the state of the art in the magnetic nanosystem Fe/W(110). It continues with the demonstration of the systematic growth of two atomic layers of iron on a tungsten single crystal. Finally, it demonstrates the successful implementation of the SP-STM technique at the IFW-Dresden by employing iron-coated tungsten tips and the nanosystem Fe/W(110).

Chapter 7 summarizes the achievements of this thesis and presents the future research directions.

2 Experimental technique

2.1 Introduction to scanning tunneling microscopy

In 1981 the physicists Gerd Binnig and Heinrich Rohrer developed a technique which was able to reveal atoms in real space for the first time (see figure 2.1). This technique, based on the already known quantum tunneling effect and so-called scanning tunneling microscopy (STM), envisaged the possibility of studying nanometric single objects, such as atoms and molecules [31–33].

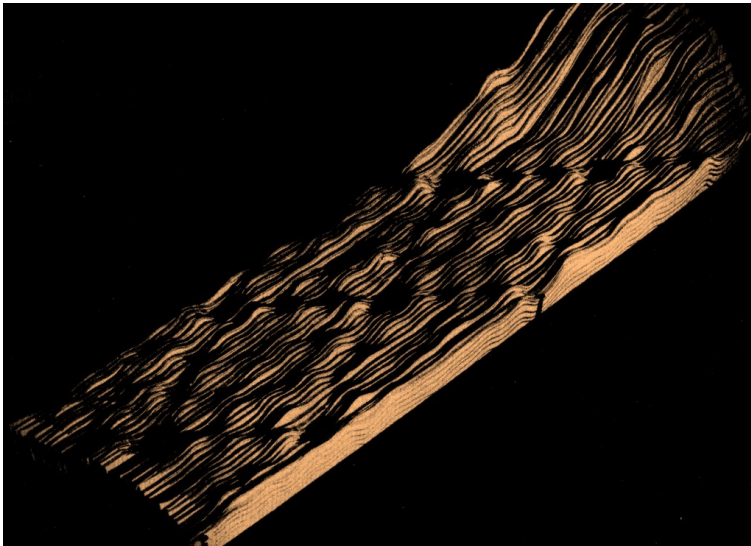


Figure 2.1: 7×7 reconstruction of Si(111). Relief assembled from the original recorder traces taken by Binnig and Rohrer. Characteristic of the rhombohedral surface unit cell are the corner holes and the 12 maxima representing the adatoms. Image taken from reference [33].

In those years, surfaces were often assumed to be perfect, and information about them was gained indirectly by spatially averaging techniques. However, with STM, features such as step edges, dislocations and adsorbed atoms became visible. Eight years later Don Eigler, working at IBM in Almaden, manipulated individual atoms on a surface. In that breakthrough experiment, Eigler arranged thirty-five Xenon atoms depicting the letters “IBM”. Later on, they created the first quantum corrals and nanoscale logic circuits by using individual molecules of carbon monoxide [34,35]. At that time, the old mankind dream of watching and manipulating atoms with human hands became a

reality through STM. In 1988 Pierce considered the possibility of developing an STM that was sensitive to the spin of tunneling electrons by using spin-sensitive tip materials [36], an approach theoretically predicted by Minakov *et al.* [37]. Two years later, Wiesendanger *et al.* demonstrated the possibility of magnetic imaging at atomic resolution. In that crucial experiment, they observed the vacuum tunneling of spin-polarized electrons with the scanning tunneling microscope. This was made possible by employing a ferromagnetic CrO_2 tip and a surface-antiferromagnetic $\text{Cr}(001)$ sample [38]. Topographic images of $\text{Cr}(001)$ confirmed the presence of terraces separated by monoatomic steps of 0.144 nm height by using a tungsten tip. However, by employing CrO_2 tips, the measured step-height values alternated around the mean value of 0.144 nm due to an additional contribution from spin-polarized electron tunneling (see figure 2.2).

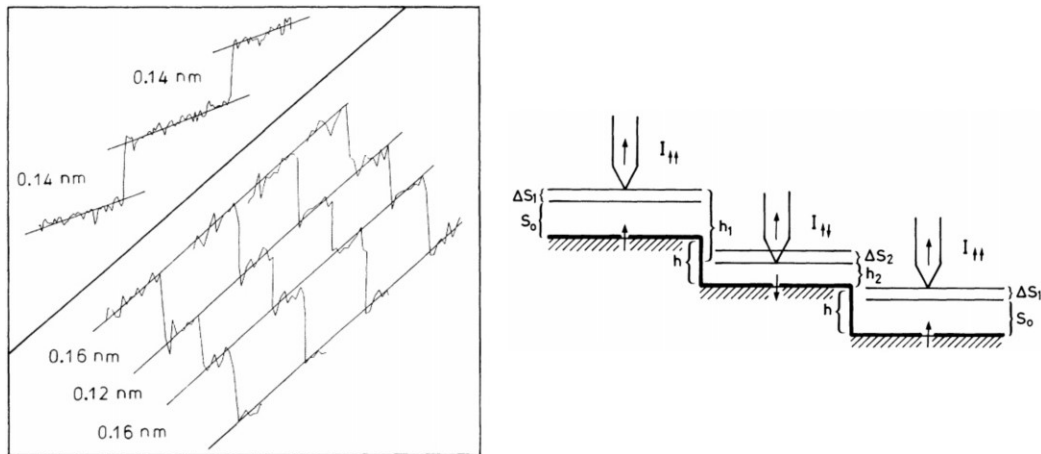


Figure 2.2: SP-STM measurement employing a CrO_2 tip and a $\text{Cr}(001)$ sample. On the left are line profiles of the atomic steps on the $\text{Cr}(001)$ surface taken with tungsten tips (0.14 nm height) and with CrO_2 tips (alternating values around 0.14 nm). On the right is the schematic illustration of the apparent height measured with a magnetic tip on a magnetic sample. Images taken from reference [38].

Since then, SP-STM has become a very important tool not only for its unique capability in the study of basic and fundamental phenomena, but also in potential applications concerning data storage devices. SP-STM has allowed the understanding of intriguing magnetic phenomena at the nanometer scale and revealed new states characteristic of a large variety of magnetic nanostructures [29]. Novel materials such as strongly correlated systems have shown a rich variety of phases, including spin density wave phases and spin textures, where SP-STM is expected to play a crucial role in the discovery and understanding of new physical phenomena [39].

Additional variations to the original scanning tunneling microscopy technique have enriched the spectrum of study, for instance the access to the electronic structure in the momentum space through analyzing Friedel oscillations [40], among others.

In the development of this chapter, the theoretical background of STM, as well as the measuring methods, will be described with the object to provide a base to interpret the scientific results obtained in this thesis.

2.2 Concept of scanning tunneling microscopy

Scanning tunneling microscopy is conceptually simple; it requires the location of a very sharp conductive tip just a few angstroms away from a conductive sample (see figure 2.3); at this distance, the electronic wave functions of the tip and sample can overlap due to the well-known quantum tunneling effect [41]. However, it is necessary to apply a bias voltage between tip and sample in order to achieve a net tunneling current. Additionally, there is the possibility to move the tip over the sample surface being assisted by a piezo electric actuator system that separately controls the tip- x - y movements and the z movement. Figure 2.3 shows the most common operation mode which uses a feedback loop to keep the tunneling current constant while the tip is moved up and down. The changes in z direction are recorded and plotted as a function of x and y , achieving the so-called topography image. Furthermore, by measuring the tunneling current at different bias voltages, STM can provide local information about the electronic properties of the sample.

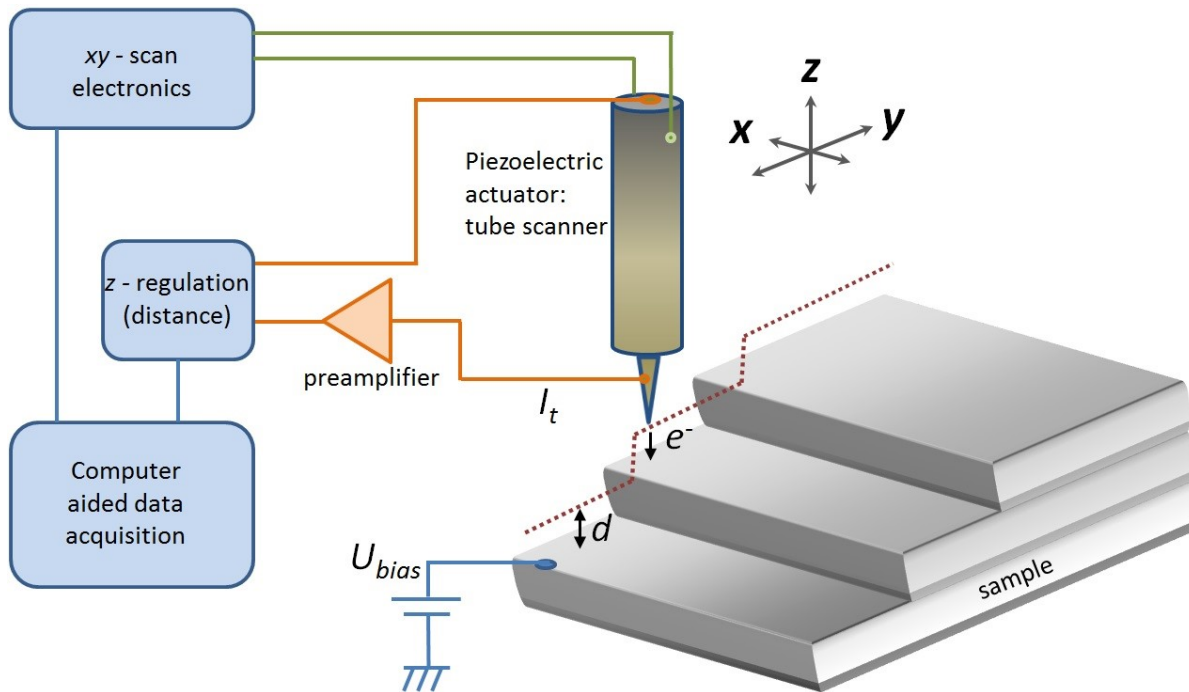


Figure 2.3: Schematic of scanning tunneling microscopy operation.

2.3 Quantum tunneling

To understand the bases of STM, the description of the tunneling process is required. In classical physics a particle with energy E can overcome a potential barrier of V_0 only if $E > V_0$; in the case that this condition is not fulfilled, the particle will be reflected. However at small scales, for instance nanometers or angstroms, particles behave differently, and they may overcome barriers even if $E < V_0$. In order to calculate the probability of a particle (electron in the case of the STM experiment) passing through a potential barrier (most of the time an insulating barrier: vacuum, air, liquid), it is necessary to analyze the problem by considering the quantum physics laws. The simplest way to do so is by solving the Schrödinger equation of a particle with energy E passing through a square potential barrier of height V_0 , as presented in figure 2.4.

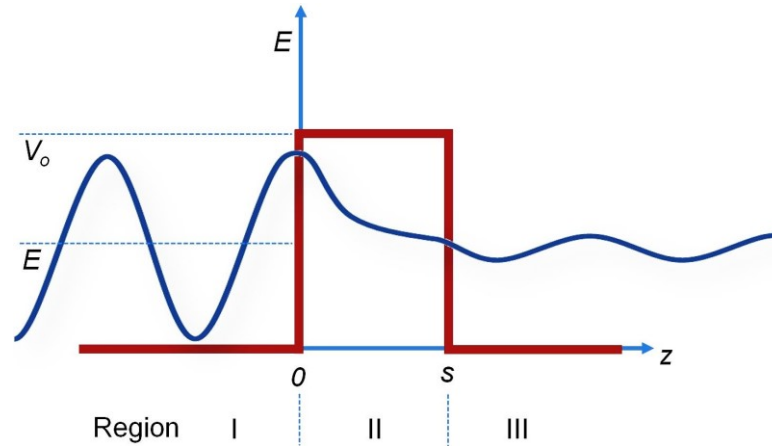


Figure 2.4: Quantum tunneling effect. Solution of Schrödinger equation for a particle of energy E interacting with a square potential barrier of energy V_0 .

There are three regions where the particle might be:

Region I $z < 0$, $V(z) = 0$, in front of the barrier (tip or sample),

Region II $0 < z < s$, $V(z) = V_0$, in the barrier (insulating barrier),

Region III $s < z$, $V(z) = 0$, behind the barrier (tip or sample).

In each region the particle can be described by the solution of the time-independent Schrödinger equation (2.1):

$$\left(-\frac{\hbar^2}{2m} \frac{d^2}{dz^2} + V(z) \right) \psi(z) = E\psi(z), \quad (2.1)$$

where ψ is the electron wave function and \hbar is the Planck constant divided by 2π . Considering a particle of mass m and energy $E < V_0$, the wave functions in the different regions are given by:

$$\psi_1 = e^{ikz} + Ae^{-ikz}, \quad k = \sqrt{2mE/\hbar^2}, \quad (2.2)$$

$$\psi_2 = Be^{-\kappa z} + Ce^{\kappa z}, \quad \kappa = \sqrt{2m(V_0 - E)/\hbar^2}, \quad (2.3)$$

$$\psi_3 = De^{ikz}. \quad (2.4)$$

For region I the resulting wave function shows oscillatory behavior corresponding to an incident particle (or reflected), while in region II the wave function shows an exponential decay. In region III the wave function shows oscillatory behavior again, related to the transmitted particle, as depicted in figure 2.4. The complete solution requires the determination of the constant values A, B, C and D by using the boundary conditions of wave function continuity and soft continuity in the points $z = 0$ and $z = s$. Once the wave functions are obtained, it is possible to calculate the incident current density (j_i), the transmitted current density (j_t) and the transmission coefficient T [42]:

$$j_i = \frac{\hbar k}{m}, \quad (2.5)$$

$$j_t = \frac{-i\hbar}{2m} \left(\psi_3^*(z) \frac{d\psi_3(z)}{dz} - \psi_3(z) \frac{d\psi_3^*(z)}{dz} \right) = \frac{\hbar k}{m} |D|^2, \quad (2.6)$$

$$T = \frac{j_t}{j_i} = |D|^2, \quad (2.7)$$

$$T = \frac{1}{1 + (k^2 + \kappa^2)^2 / (4k^2\kappa^2) \sinh^2(\kappa s)}. \quad (2.8)$$

In the limit of a strongly attenuating barrier (decay constant $\kappa s \gg 1$), the T coefficient is approximately:

$$T \approx \frac{16k^2\kappa^2}{(k^2 + \kappa^2)^2} e^{-2\kappa s}. \quad (2.9)$$

The latter equation shows the exponential dependence of the transmission coefficient T and indirectly of the tunneling current with the tunneling barrier width (s). Furthermore, this result explains the high sensitivity of the tunneling current to the variations of the distance between the tip and the sample (an aspect of crucial importance to achieve atomic resolution). Although the last model describes the concept of electron tunneling very well by treating the electrons as non-interacting particles, it

presents serious problems in describing the tunneling current in a more realistic manner. For instance, there is no dependence of the tunneling current on the density of states of the surface. Therefore, in the next section a more advanced approach based on the time-dependent perturbation theory will be described.

2.4 Tunneling current

In 1961 Bardeen used the first-order time-dependent perturbation theory to describe the tunneling current produced in planar metal-oxide-metal junctions. This approach basically derives the tunneling current of the overlapping wave functions of the two electrodes separated by the oxide layer [43]. In 1985, Tersoff and Hamann applied the Bardeen transfer Hamiltonian to tunneling experiments held by STM, finding the following relation for the tunneling current [44,45]:

$$I = \frac{2\pi e}{\hbar} \sum_{t,s} f(E_t)[1 - f(E_s + eU)] |M_{ts}|^2 \delta(E_t - E_s). \quad (2.10)$$

In the latter relation, $f(E)$ represents the Fermi function, U is the applied bias voltage, and M_{ts} the tunneling matrix element between states ψ_t of the probe and ψ_s of the sample surface. E_t is the energy of the unperturbed state ψ_t . As the tunneling process is considered only elastic in this mathematical treatment, the delta-function is present. Different experimental assumptions were considered in order to simplify the equation 2.10; for instance, at low temperatures the Fermi distribution can be approximated as a step function and in the limit of small bias voltages (~ 10 mV for metals) the tunneling current can be written as:

$$I = \frac{2\pi}{\hbar} e^2 U \sum_{t,s} |M_{ts}|^2 \delta(E_s - E_F) \delta(E_t - E_F), \quad (2.11)$$

where E_F is the Fermi level. The next step is to calculate the tunneling matrix element which is related to the tunneling probability introduced in equation 2.7. Bardeen showed that [43]:

$$M_{ts} = \frac{-\hbar^2}{2m} \int d\vec{S} \cdot (\psi_t^* \vec{\nabla} \psi_s - \psi_s \vec{\nabla} \psi_t^*). \quad (2.12)$$

The integral has to be over any surface, lying entirely within the vacuum barrier region. The quantity in parentheses is simply the current density (j_{ts}). The tunneling matrix element can be calculated only if the exact expressions for wave functions ψ_t and ψ_s of tip and sample are known. However, the wave functions from the tip cannot be determined due to its unknown atomic structure. Taking into account the latter problem, Tersoff and Hamann assumed that the tip presents an arbitrary shape, but a spherical

symmetry at the foremost end (see figure 2.5). Therefore, they assumed only s -like electronic states ($l = 0$) for the tip. Now, if identical work functions ϕ for tip and sample are assumed, the tunneling current can be written as:

$$I \propto U \cdot \rho_t(E_F) \cdot e^{2\kappa R} \cdot \sum_{\nu} |\psi_s(\vec{r}_o)|^2 \cdot \delta(E_s - E_F), \quad (2.13)$$

$$\kappa = \frac{\sqrt{2m\phi}}{\hbar}. \quad (2.14)$$

$\rho_t(E_F)$ corresponds to the density of states at the Fermi level for the tip, R to the effective tip radius, and r_o to the center of curvature of the tip. Equation 2.14 represents the decay rate. Now, by looking at the expression 2.13, the term:

$$\sum_{\nu} |\psi_s(\vec{r}_o)|^2 \delta(E_s - E_F) = \rho(\vec{r}_o, E_F) \quad (2.15)$$

can be assigned to the surface local density of states (LDOS) at the Fermi level, evaluated at the center of curvature r_o of the effective tip.

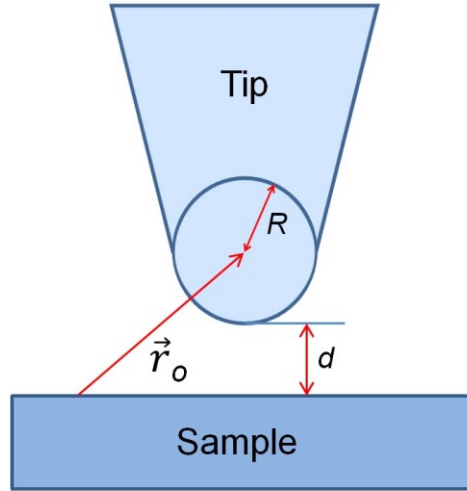


Figure 2.5: Schematic of the STM tip geometry in the Tersoff-Hamann model, where d is the distance from the foremost end of the tip to the sample surface, R is the radius of the spherical tip and \vec{r}_o the distance of any point of the sample to the center of the spherical tip.

Since the wave functions decay exponentially in the z direction normal to the surface towards the vacuum region, the surface wave functions can be written as:

$$\psi_s(\vec{r}_o) \propto e^{-\kappa z}, \quad (2.16)$$

with

$$|\psi_s(\vec{r}_o)|^2 \propto e^{-2\kappa(d+R)}, \quad (2.17)$$

where d is the distance between the sample surface and the front end of the tip (see figure 2.5). Thus the tunneling current becomes exponentially dependent on the distance d :

$$I \propto e^{-2\kappa d}. \quad (2.18)$$

As was previously mentioned, the Tersoff-Hamman theory works at small bias voltages, where the matrix tunneling element is assumed constant in energy. Thus, the tunneling current may be interpreted as proportional to the sample density of states (DOS). However this simple interpretation of the tunneling current is not valid for non-metallic DOS, such as that of a superconductor, which exhibits a gap at the Fermi level. Furthermore, this interpretation is not valid for high bias voltage or for tip wave functions with angular dependence.

The problem of considering high bias voltage raises other issues such as the distortion of the tip and sample surface wave functions as well as a modification of the energy eigenvalues [28]. The calculation of these tip and sample affected wave functions under bias voltages is rather difficult. Therefore, as a first approximation, the undistorted zero-voltage wave functions and energy eigenvalues are usually taken. In that sense, the effect of the finite bias U only enters through a shift in energy of the undistorted surface wave functions or density of states relative to the tip by an amount of eU [27]. Thus, a more general expression to the tunneling current might be considered by converting the sum of equation 2.13 into an integral over quasi continuous states:

$$I \propto \int_0^{eU} \rho_t(E) \cdot \rho_s(E, r_o) dE. \quad (2.19)$$

$\rho_t(E)$ is the density of states for the tip and $\rho_s(E, r_o)$ is the density of states for the sample surface evaluated at the center of curvature r_o of the effective tip. By considering the Wentzel-Kramers Brillouin (WKB) approximation, $\rho_s(E, r_o)$ could be written as:

$$\rho_s(E, r_o) \propto \rho_s(E) \cdot \exp \left\{ -2(d+R) \left[\frac{2m}{\hbar^2} \left(\frac{\phi_t + \phi_s}{2} + \frac{eU}{2} - E \right) \right]^{1/2} \right\}, \quad (2.20)$$

where ϕ_t and ϕ_s are the work functions of tip and sample respectively, and $d+R$ is the effective distance between tip and sample (see figure 2.5). The exponential function in

equation 2.20 is the energy- and bias-dependent transmission coefficient $T(E, eU)$. Consequently, a more general tunneling current has the next form [27,28,46]:

$$I \propto \int_0^{eU} \rho_s(E) \cdot \rho_t(E, eU) \cdot T(E, eU) dE. \quad (2.21)$$

As can be seen, the latter equation takes into account the dependence on energy of the transmission coefficient and thus the tunneling matrix element, which was a limitation of the original Tersoff-Hamann model. Therefore, equation 2.21 can be more accurately used for the tunneling current interpretation at high bias voltages.

The Tersoff-Hamann model is in agreement with the obtained experimental results, revealing the Au(110) surface [44], however it qualitatively fails on closed packed surfaces like Al(111) or Au(111). The latter problem was related to the fact that d-like bands dominate in tungsten, platinum or iridium tips, generally used in STM. These d-like bands contribute about 85% to the tip local density of states (LDOS) at the Fermi level. Chen *et al.* [47] solved the problem by adding to the Tersoff-Hamann model also tip states other than s-like. The derivative rule [28] introduced by Chen and the assumption of d_{z^2} -like tip provided a better agreement with the experiments.

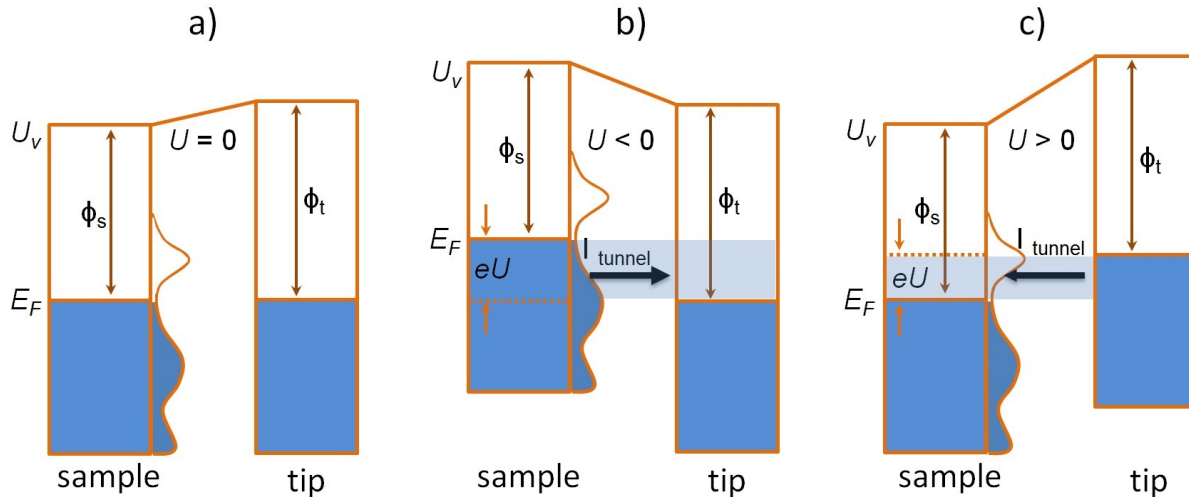


Figure 2.6: Schematic of the sample and tip in tunneling regime. (a) No net tunneling current, (b) negative sample bias, net current from sample to tip, (c) positive sample bias, net current from tip to sample.

A pictographic description of the tunneling current involving the tip and sample density of states is shown in Figure 2.6. The occupied states are indicated by the blue region below the Fermi energy and the sample density of states is highlighted by the curve inside the tunneling barrier. In the case of the tip density of states, considering the ideal case, it is assumed as constant parameter, with the final purpose to investigate the

sample. Moreover, the work functions of the tip and the sample (ϕ_t, ϕ_s) are shown. Figure 2.6 (a) represents the tunneling junction in absence of a bias voltage, which indicates zero net tunneling current. Figure 2.6 (b) shows the effect of a negative bias voltage, where the electrons from the sample in the energy interval between $(E_F - eU)$ and E_F flow into unoccupied states of the tip. Figure 2.6 (c) depicts the junction while a positive bias voltage is applied, showing the opposite case to Figure 2.6 (b).

2.5 Scanning tunneling microscopy

Scanning tunneling microscopy is usually applied for the investigation of the surface structure or “topography” in a sample. By taking advantage of the exponential dependence between the tunneling current and the sample-tip distance (as was shown in equation 2.18), STM allows to resolve atomic structures ($< 1 \text{ \AA}$ in size) [28].

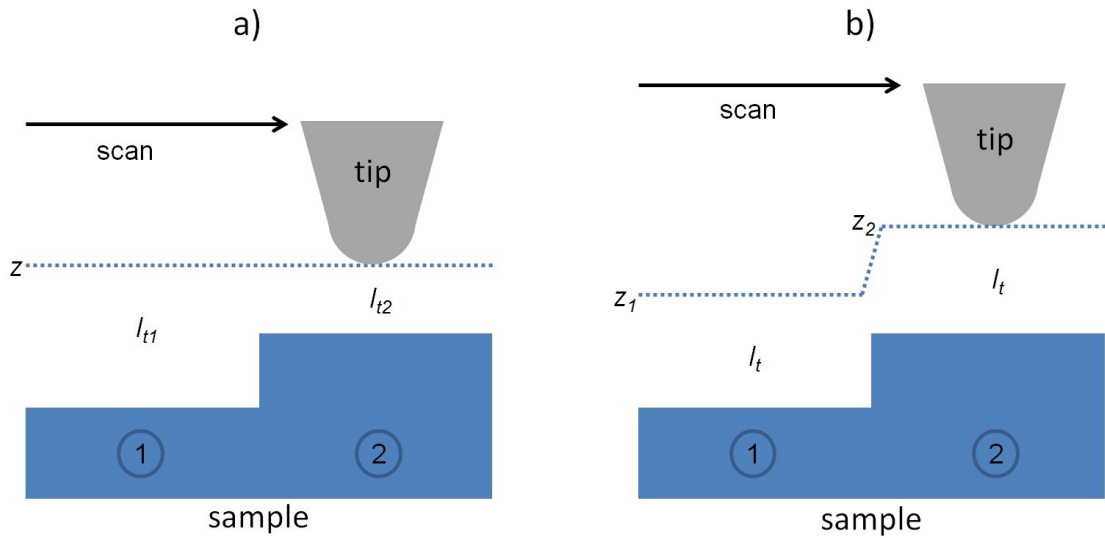


Figure 2.7: STM operation modes. (a) Constant height ($z = z_1 = z_2$), measurement of the current I_t , with $I_{t1} < I_{t2}$, (b) constant current ($I_t = I_{t1} = I_{t2}$), measurement of the height (z) with $z_1 < z_2$.

Figure 2.7 shows two STM working modes. The first mode, illustrated in figure 2.7 (a), measures the tunneling current by keeping the height z constant while the tip scans the sample. Consequently, the topography is revealed by plotting $I_t(x, y)$. This mode requires a flat surface in order to avoid the hitting of the tip with the sample, although this operation mode allows for faster scanning. Figure 2.7 (b) shows the second STM mode, which is more commonly used. It consists of keeping the tunneling current constant through a feedback loop which drives the tip up and down during the tip scan. Thus the variations in z reveal the surface topography by plotting $z(x, y)$ [48].

In this thesis the topographic images were acquired by using the constant current mode. For small voltages, the topographic image of a sample corresponds approximately to the

contour map of constant surface local density of states at E_F (equation 2.13), while for high voltage the dependence of the tunneling current on the electronic structure of the sample has to be considered in order to interpret the STM images (equation 2.21).

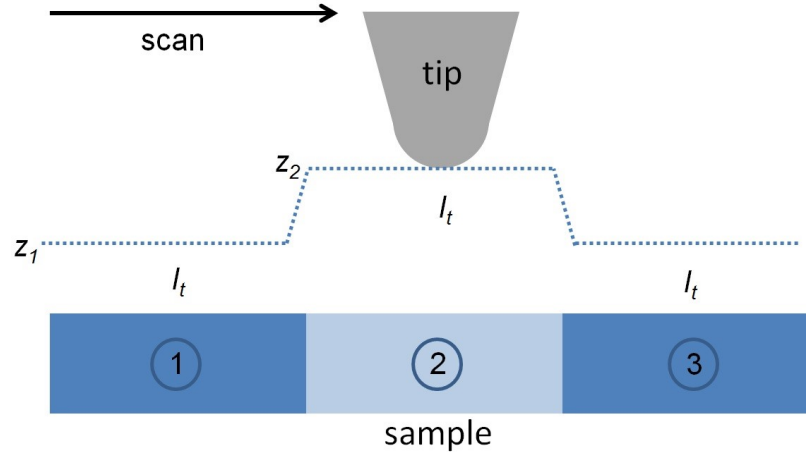


Figure 2.8: Schematic of a no real topography revealed by using constant current mode and showed in areas of the sample surface with different density of states ($\rho_1 = \rho_3 < \rho_2$).

As was shown, the tunneling current depends on the density of states of the sample and tip. By assuming a constant density of states of the tip, the variations of the density of states in the sample surface are shown in the topographic image acquired by STM. However, this means that in order to observe the real topography, the density of states on the surface should commensurate with the structure (e.g. in order to see atoms the electronic density of states should correspond one to one with the atomic structure). Often this is not the case, for example in electronically flat metals where it is especially complicated to observe the atomic corrugation. Furthermore, the presence of charge density waves, defects, or impurities on the sample surface also makes the interpretation of the STM topography difficult [49,50]. Figure 2.8 illustrates an example where a flat sample contains an area (2) with different density of states. In this particular case, the STM operates in constant current mode, and the corresponding topographical plots obtained do not correspond with the real sample morphology.

2.6 Scanning tunneling spectroscopy

STM is not only able to image sample surfaces as contours maps, but it can gain spectroscopic information at localized surface points. Thus, STM allows the study of the electronic structure of single objects such as atoms, molecules, defects and impurities, among others. Of noteworthy, when compared to other average spectroscopic techniques, such fine resolution is not achieved. The spatial resolution can reach the order of picometers (pm) and the energy resolution depending on the temperature

($\Delta E = 3.5K_B T$, see discussion below) might reach the order of microelectronvolts (μeV) at 300 mK [51].

Such spectroscopy study is possible due to the dependence of the tunneling current on the density of states from the tip and sample (see equation 2.21). With the purpose to avoid the influence of the tip, it is necessary to choose a tip with nearly constant density of states around the Fermi level (e.g. metallic tips). As to experimentally probe the sample density of states, the tip is held at a fixed distance from the sample and fixed in a spatial point. Subsequently, the bias voltage is swept from the stabilization point (initial I_t and U_{bias}) until the final desired value while the tunneling current is measured. The latter procedure is, of course, also achievable for several points on the surface, even reproducing the sample topography. The obtained data is generally named spectroscopic map [40]. However, by only analyzing the tunneling current ($I(U)$), it is not easy to come directly to conclusions about the sample density of states, as the integral involved in the tunneling current avoids the direct proportionality between the tunneling current and the local density of states. For that reason, the data in STS experiments is commonly treated by using the first derivative of the tunneling current with respect to the bias voltage (dI/dU), so-called differential conductance, which has a direct dependence with the sample density of states, as shown in equation 2.22:

$$\frac{dI(U)}{dU} \propto \rho_t(0) \cdot \rho_s(eU) \cdot T(z, eU, eU) + \int_0^{eU} \rho_t(E - eU) \rho_s(E) \frac{dT(z, E, eU)}{dU} dE. \quad (2.22)$$

The previous expression is obtained by differentiating equation 2.21 with respect to U . If the tunneling process is carried out in a tiny energy window (by using small bias voltages) in comparison with the work functions of the sample and the tip, and additionally considering metallic tips (constant DOS), the voltage dependence of the transmission coefficient (T) can be ignored and one finds $dI/dU \propto \rho_s(eU)$ [52].

Technically, there are two ways to obtain the dI/dU signal: the first is through a numerical differentiation of the tunneling current ($I(U)$) and the second, which is more sophisticated, through a lock-in technique. Both procedures were employed in this thesis and will be addressed in due course. Nevertheless, considering the special importance of the lock-in technique in the SP-STM experiments, it will be explained in more detail in the following section.

2.6.1 The lock-in technique

The lock-in technique consists of adding a small voltage modulation of the form: $V_m \cos(\omega t + \theta)$ to the bias voltage (U), where V_m is the modulation amplitude, ω the frequency and θ the phase. Therefore, the tunneling current can be written as:

$$I = I(U + V_m \cos(\omega t + \theta)), \quad (2.23)$$

and by using the Taylor and Fourier analysis [53]:

$$\begin{aligned}
 I(U + V_m \cos(\omega t + \theta)) & \\
 &= I(U) + a_o \frac{dI(U)}{dU} V_m \cos(\omega t + \theta) \\
 &+ a_1 \frac{d^2 I(U)}{dU^2} V_m^2 \cos(2\omega t + \theta) + \dots
 \end{aligned} \tag{2.24}$$

being a_n constants.

The task is now to single out the second term in equation 2.24, which is the first harmonic of the tunneling current where the differential conductance takes place. In order to do that, the lock-in technique presents a phase-sensitive detector circuit (PSD) that can extract a signal with a known carrier wave from an environment where several signals are present. The PSD multiplies the excited tunneling current by a well-known (in amplitude (V_r), frequency (ω) and phase (φ)) reference signal: $V_r \cos(\omega t + \varphi)$. The output of the PSD will be:

$$V_{PSD} = V_r \cos(\omega t + \varphi) \times \left[a_o \frac{dI(U)}{dU} V_m \cos(\omega t + \theta) \right], \tag{2.25}$$

by applying the appropriate trigonometric identities, the previous can be written as:

$$V_{PSD} = a_o \frac{V_r}{2} \frac{dI(U)}{dU} V_m [\cos(\theta - \varphi) + \cos(2\omega t + \theta + \varphi)], \tag{2.26}$$

by passing through a low-pass filter, the $2\omega t$ component is removed, becoming the PSD output a DC signal:

$$V_{PSD} = a_o \frac{V_r}{2} \frac{dI(U)}{dU} V_m [\cos(\theta - \varphi)]. \tag{2.27}$$

In order to obtain the maximum output, the phase difference between the excited tunneling current and the lock-in reference oscillator ($\theta - \varphi$) should be 0° or 180° . The modern lock-in amplifiers (i.e. Stanford SR830, used in this thesis [54]), have a second PSD that overcomes this problem. In this case, the excited signal (equation 2.24) is multiplied by the second PSD with a reference modulation shifted 90° , which means by $V_r \cos(\omega t + \varphi + 90^\circ)$. Therefore, the pass filtered output of the second PSD is:

$$V_{PSD} = a_o \frac{V_r}{2} \frac{dI(U)}{dU} V_m [\sin(\theta - \varphi)]. \tag{2.28}$$

Finally, the lock-in amplifier provides a vector output (X, Y):

$$X = a_o \frac{V_r}{2} \frac{dI(U)}{dU} V_m [\sin(\theta - \varphi)], \quad Y = a_o \frac{V_r}{2} \frac{dI(U)}{dU} V_m [\cos(\theta - \varphi)]. \tag{2.29}$$

Technically, by adjusting the amplifier to a phase difference of 90° the Y component is zero and the X component reaches its maximum. In addition, X is the first harmonic of the excited tunneling current and is proportional to the differential conductance (dI/dU) and to the local density of states (LDOS) of the sample probed by the STM tip. Figure 2.9 shows a parallel of the two scenarios of the tunneling junction for the STM experiment: one where the tunneling current is recorded, involving several sample electronic states in the energy range $E_F - eU$ (figure 2.9 (a)), and a second where the sample electronic density of states are probed at a define value of energy eU (figure 2.9 (b)).

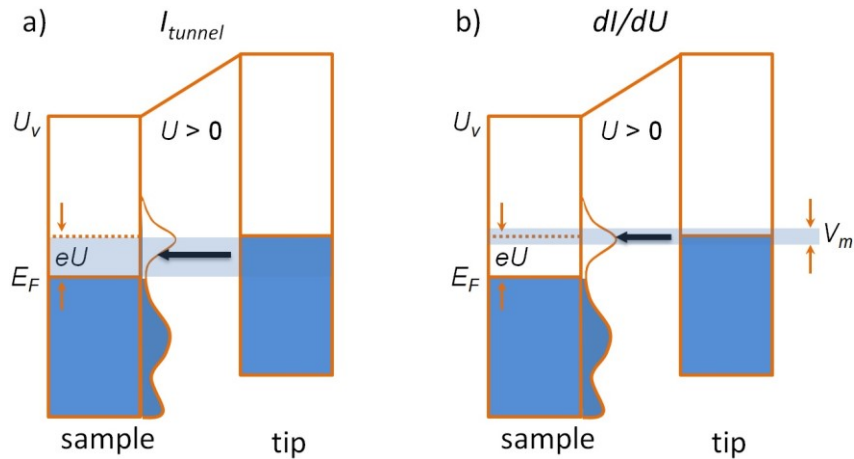


Figure 2.9 Schematic of the comparison between the sample LDOS involved in the tunneling current (a) and the sample LDOS involved in the differential conductivity (b).

2.6.2 Energy resolution of STS at finite temperatures

One important aspect in scanning tunneling spectroscopy is the energy resolution. This refers to the minimum value of energy between two features in the sample-DOS which can be distinguished.

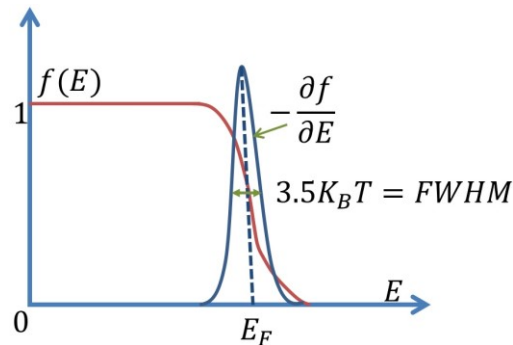


Figure 2.10 Thermal broadening of the Fermi distribution $f(E)$ [55].

Disregarding the influence of the device by assuming a very stable STM, the main contributions to the energy resolution are the finite temperature and the modulation voltage in case of using Lock-in technique. At finite temperature the STS resolution is limited by the thermal broadening of the Fermi distribution, which is calculated through the FWHM (Full width at half maximum) of its derivative as is depicted in figure 2.10. Thus, a good approximation of the energy resolution ΔE_T is $3.5K_B T$. However, as was mentioned before, the amplitude of the modulation voltage V_m , which is added to the bias voltage in order to measure the dI/dU signal by lock-in technique, also contributes to blur the dI/dU signal. Therefore the overall energy resolution can be expressed by [56]:

$$\Delta E = \sqrt{(\Delta E_T)^2 + (\Delta E_{V_m})^2} = \sqrt{(3.5K_B T)^2 + (2.5eV_m)^2}. \quad (2.30)$$

Significantly, the thermal broadening is more influential in blurring the dI/dU signal at room temperature, while at low temperature the modulation voltage V_m becomes more important.

2.7 STM and STS data

Figure 2.11 summarizes the information that was acquired by means of STM and STS in this thesis: Firstly, the acquisition of topographic images was carried out in a constant current mode by plotting $z(x, y)$. The height (z) is represented by a color scale, where dark-color indicates the lowest parts in the sample, while bright-color the highest ones. Topography-acquisition was possible by measuring the tunneling current where several sample-DOS were involved depending on the bias voltage. Secondly, dI/dU -maps were recorded with the assistance of a lock-in technique by plotting $\frac{dI}{dU_{eU}}(x, y)$. In this case the differential conductance ($\frac{dI}{dU_{eU}}$) is represented by the color scale, where sample areas with low differential conductance are dark and areas with high differential conductance are bright. These maps represent the differential conductance of the sample at one specific value of energy (eU), chosen by the bias voltage. Thirdly, single point spectroscopy was obtained by plotting $\frac{dI}{dU_{(x,y)}}(eU)$, which represents the differential conductance tested in a single point by changing the energy (eU).

Another option to obtain further information from the sample is the spectroscopic map; however, it was not used in this thesis. In this case, the single point spectroscopy is taken in several points on the sample surface, sometimes even reaching the same number of points than a topographic image. This process requires high stability of the experiment for long periods of time (i.e. days to weeks).

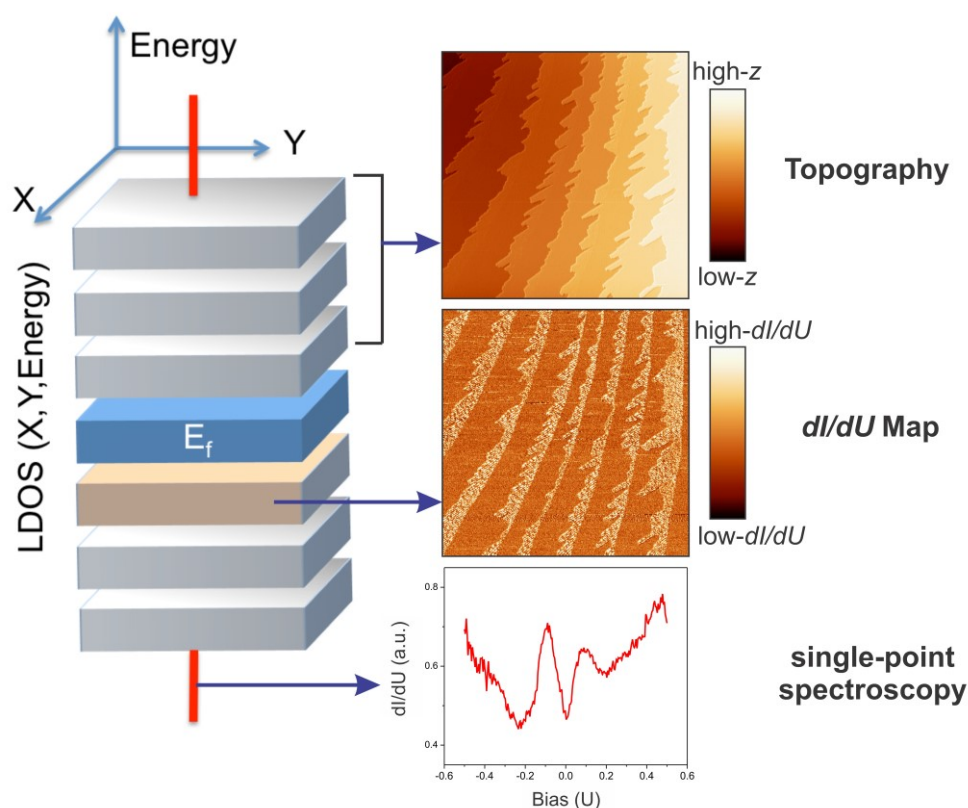


Figure 2.11 Different types of information acquired through STM and STS. By looking at the sample-LDOS, topographic images, dI/dU maps, and single-point spectra can be interpreted. The color scale in the images depicts the differences in height for topography and the differences in differential conductance for dI/dU maps. Dark regions correspond to low-values and bright regions to high-values.

2.8 Spin-polarized STM/STS

Spin-polarized STM/STS is an extension of the above described technique. It is carried out when both electrodes (sample and tip) are magnetic. Therefore, the tunneling current between tip and sample will be affected by the magnetoresistance effect, which means that the relative orientation of the magnetic moments of tip and sample will determine how easily the electronic current flows through the tunneling barrier [57]. From a fundamental point of view, the spin-polarized tunneling can be explained considering the tunneling probability in a magnetic junction where both electrodes exhibit spin-split density of states (see figure 2.12). Figure 2.12 (a) shows the magnetic configuration for the highest tunneling probability, when both sample and tip have parallel magnetization alignment. In this case an electron with spin \uparrow located in an occupied tip state can tunnel into an empty sample state with spin \uparrow , as indicated by the green arrow in figure 2.12 (a). The opposite situation (anti-parallel alignment) is presented in figure 2.12 (b). In this

specific case, the electron with spin \uparrow in the occupied tip state has less \uparrow unoccupied sample states to tunnel. The latter scenario leads to the lowest tunneling probability.

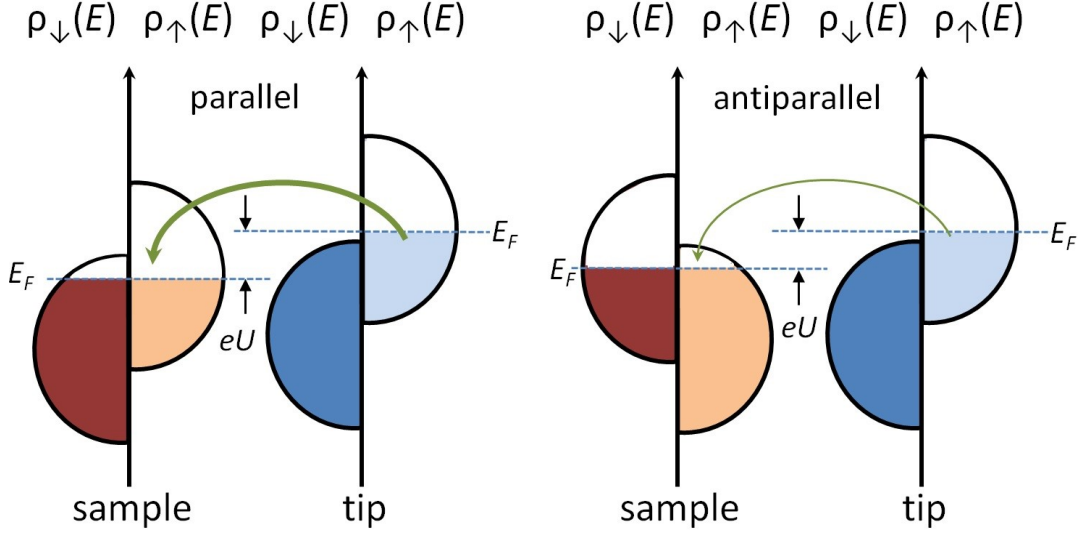


Figure 2.12: Schematic of the spin-polarized tunneling at positive bias. (a) High probability due to large number of unoccupied states (\uparrow), and (b) low probability due to few unoccupied states (\uparrow).

A simple model for the spin-polarized tunneling current was obtained from the theoretical treatment of the electron tunneling between two spin-polarized electrodes by Slonczewski [58]. Therefore, by assuming a free-electron behavior of the conduction electrons and at small bias voltages, the spin-polarized tunneling current I_{SP} can be written in good approximation as [56]:

$$I_{SP}(U_o) = I_o [1 + P_s \cdot P_t \cdot \cos(\vec{M}_s, \vec{M}_t)], \quad (2.30)$$

$$P(E) \equiv \frac{\rho_{\uparrow} - \rho_{\downarrow}}{\rho_{\uparrow} + \rho_{\downarrow}}, \quad (2.31)$$

where I_o is the non-spin-polarized current, P_s and P_t are the spin polarizations of the sample and the tip, respectively, defined in equation 2.31 (where ρ is the DOS). \vec{M}_s and \vec{M}_t are the sample and tip magnetizations, respectively. Equation 2.30 considers the possibility of an intermediate magnetic alignment between electrodes, with a certain angle between \vec{M}_s and \vec{M}_t . Thus, the spin-polarized tunneling current is affected, as is shown in figure 2.13, by a cosine function where the angle α between electrode-magnetizations determines the final value of the spin-polarized tunneling current.

Experimentally, by using a non-magnetic tip and a magnetic sample (see figure 2.14) the sample topography will not reveal any change due to its magnetic structure. However, it might be possible that domain walls can be visible because of the different electronic

density of states with respect to the domains promoted by the spin-orbit coupling effect [59].

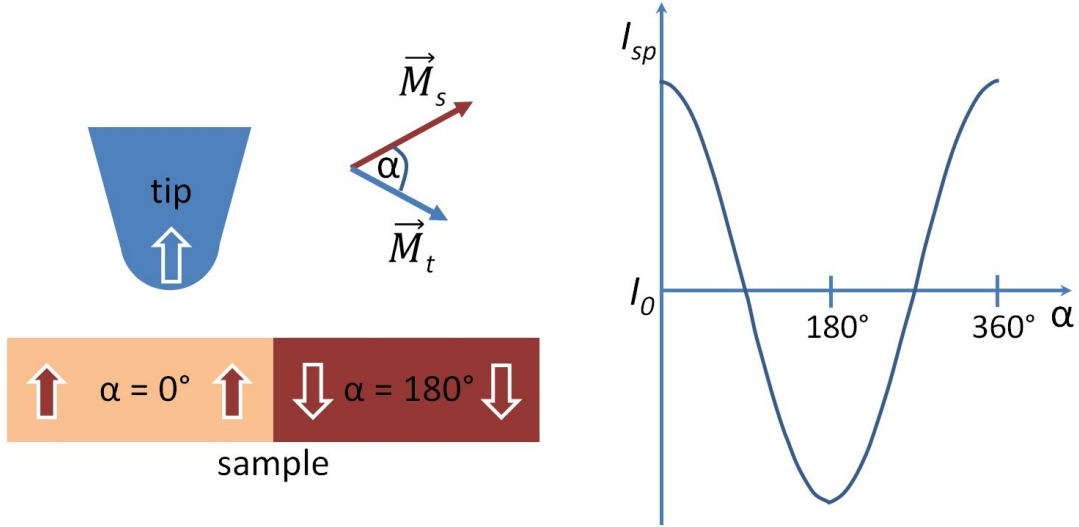


Figure 2.13 Schematic of the sample and tip magnetic alignment. Intermediate alignment characterized for the angle α between tip and sample magnetizations (\vec{M}_t, \vec{M}_s) and the influence on the spin-polarized tunneling current I_{sp} .

The case where a magnetic tip and a magnetic sample are used in the same experiment (see figure 2.15), the magnetic domains of the sample may be visible in the sample topography. This would only happen if the tunneling current has an excellent signal-to-noise ratio, achieved by a high spin polarization in the tunneling and a good alignment between the tip and sample magnetic moments [60]. Nevertheless, the most effective method to reveal the sample magnetic structure is by probing the spin-polarized LDOS through the measurement of its differential conductance [61]. The corresponding theory of Tersoff and Hamann has been generalized by Wortmann *et al.* [62] for the case of magnetic STM imaging obtaining the next expression for the differential conductance:

$$\frac{dI}{dU}(\vec{r}_o, U) \propto \rho_t \rho_s(\vec{r}_o, E_F + eU) + \vec{m}_t \vec{m}_s(\vec{r}_o, E_F + eU) \quad (2.32)$$

where ρ_t, ρ_s are the corresponding non-spin polarized LDOS and \vec{m}_t, \vec{m}_s are the vectors of the spin-polarized LDOS of tip and sample respectively. Thus, the magnetization angle at a specific energy can be probed directly by measuring the differential conductance (dI/dU) [61].

Technically, a similar procedure described in section 2.6.1 (by employing the lock-in technique) allows us to look at the magnetic structure of the sample surface. Taking into account that the sample surface contains magnetic domains with different spin-split LDOS, it is possible to observe spatially the spin-polarized LDOS when a magnetic tip is

implemented in the STM set-up, finally revealing the magnetic domains in a dI/dU map (see figure 2.15).

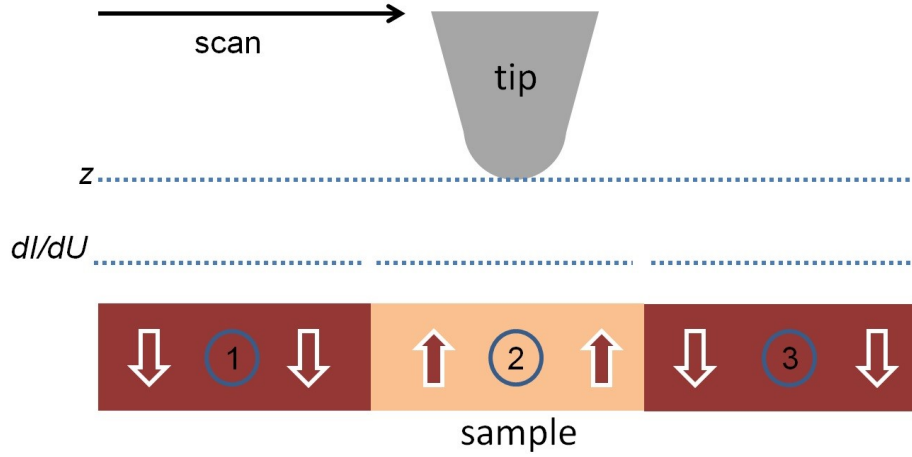


Figure 2.14 Schematic of a nonmagnetic tip and magnetic sample in a tunneling junction, apparent height (z) and differential conductance (dI/dU).

By choosing the appropriate bias voltage it is possible to achieve the highest contrast when highly-polarized sample states are probed. However, in this procedure it is important to distinguish between changes in the normal LDOS and the spin-polarized LDOS. One way to do this is by comparing two simultaneously recorded dI/dU maps, one obtained with a bias voltage where the spin asymmetry defined by equation 2.33 becomes zero (electronic contrast image) and a second obtained with a different bias voltage where the spin asymmetry is maximum (magnetic contrast image) [29].

$$A \equiv \frac{dI/dU_{\uparrow\uparrow} - dI/dU_{\uparrow\downarrow}}{dI/dU_{\uparrow\uparrow} + dI/dU_{\uparrow\downarrow}}. \quad (2.33)$$

The spin asymmetry of equation 2.33 is useful to characterize the spin polarization of the tunneling junction, which is calculated by employing the spin-polarized tunneling current, as is shown in equation 2.34 [63].

$$P = \frac{I_{\uparrow\uparrow} - I_{\uparrow\downarrow}}{I_{\uparrow\uparrow} + I_{\uparrow\downarrow}}. \quad (2.34)$$

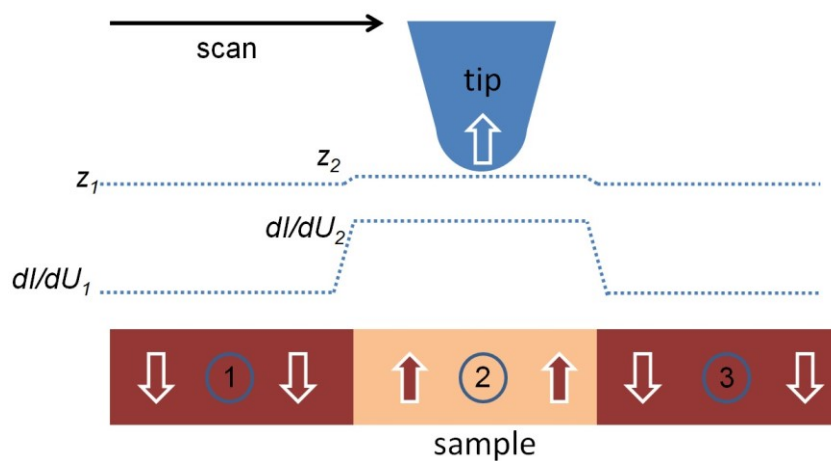


Figure 2.15 Schematic of a magnetic tip and magnetic sample in a tunneling junction. Apparent height (z) and differential conductance (dI/dU) raised from the different spin-polarized LDOS in the sample.

3 Instrumentation

3.1 General considerations for the two used microscopes

3.1.1 The coarse approach system

As was shown in chapter 2, the quantum tunneling phenomenon is possible when the tip is just a few angstroms away from the sample surface. This challenging task is carried out by the coarse approach system (see figures 3.1 and 3.2). The tip is hosted in a sapphire prism, as is shown in figure 3.1. Around the sapphire prism six piezo stacks are installed in a way that each side is in direct contact with two of them. These little motors allow the approach-retract movement of the prism through the “slip-stick” mechanism.

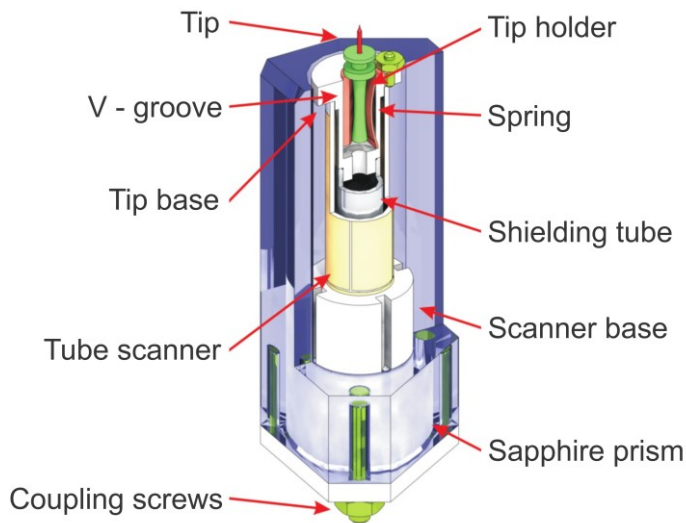


Figure 3.1: Schematic of the sapphire prism, which hosts the tube scanner and the tip (image by Danny Baumann).

The slip-stick approach-retract mechanism is done by moving the sapphire prism through the shear movement of the piezo stacks, whereas a high voltage signal is applied to the stacks (see figure 3.2). The tip approach-retract mechanism is depicted in figure 3.2 (a), showing the three main steps related to the signal outcome, shown in figure 3.2 (b). The first step (1) is based on a negative voltage signal which locates all piezo stacks in a shift position, as is depicted in the corresponding schematic. In the second step (2) the voltage signal increases its magnitude and becomes positive. In this case, the piezo stacks move the sapphire prism some nanometers (up or down) through frictional

sticking. Finally, in the third step (3), the voltage signal returns quickly to the initial state (1), changing the state of the stacks without moving the sapphire prism (slip). The latter described steps allow the user to move the tip from some nanometers to centimeters by employing voltage signals with frequencies in the order of kHz.

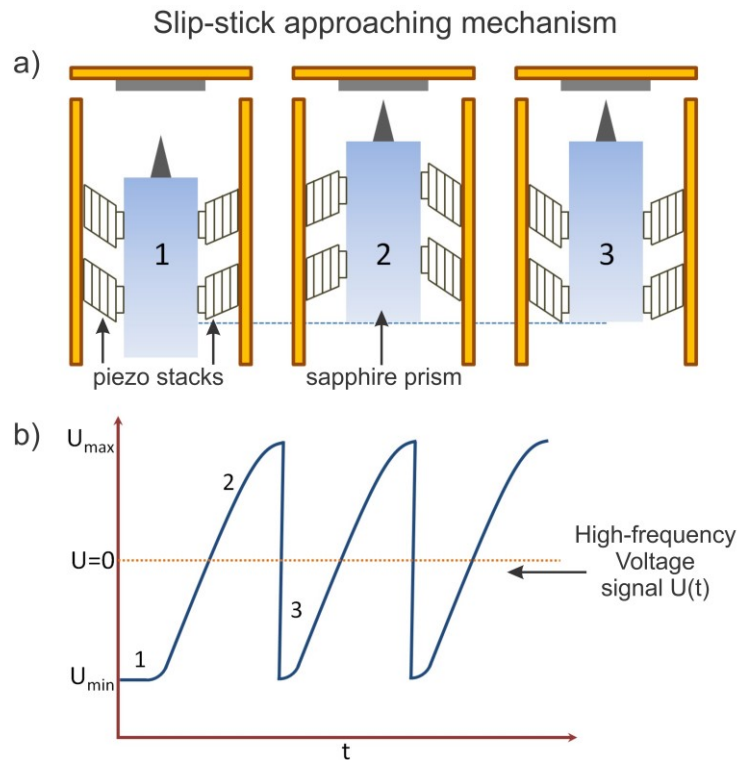


Figure 3.2: (a) Operation scheme of the “slip-stick” approaching mechanism, (b) high-frequency voltage signal usually applied to the piezo stacks.

3.1.2 The tube scanner

Inside the sapphire prism there is the tube scanner (see figure 3.3), which is responsible for the three dimensional movement of the tip. The tube scanner is made of a piezoelectric material composed of lead-zirconate-titanate and officially named PZT-8 [64].

The tube scanner possesses four symmetric outer electrodes and another inner one (see figure 3.3). By applying voltage signals to the electrodes, different bending modes of the tube which is fixed at one end are obtained. For instance, in figure 3.3 (a), the elongation-contraction of the tube scanner in z direction is depicted by applying a voltage signal to the inner-electrode while the outer electrodes are grounded. On the other hand, figure 3.3 (b) shows the bending modes in x direction (similar to y direction) by applying voltage signals to the outer electrodes while the inner electrode is grounded. The most

important characteristics of the scanner unit are: i) high resonance frequencies which lead to high scan speeds, ii) high sensitivity that lead to large scan areas, iii) low cross-talk between x , y , and z piezo drives, which induces distortion-free imaging, iv) low nonlinearities, hysteresis and creep that also contribute to reduce the image distortions, and v) low thermal drift [27,28].

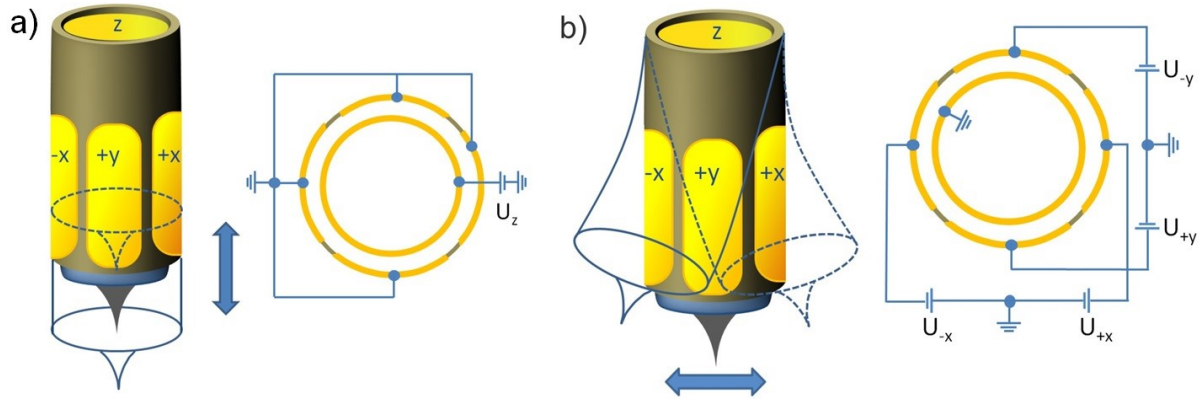


Figure 3.3: Operation scheme of the tube scanner.

3.1.3 Electronics basics

A fundamental part in a STM-system is the electronic control; it ensures the proper and optimum operation of the STM-hardware by the user. It is worth mentioning, however, that a bad design of the electronic control could yield electrical noise and pickup, or feedback loop instabilities which could be catastrophic for high-quality data acquisition. Figure 3.4 shows a block diagram of an STM electronic system. In order to produce a net tunneling current between tip and sample, a bias voltage is applied between these two electrodes. The voltage (typically between 1mV and 4V) is supplied by a computer-controlled digital-to-analog converter (DAC). Once the tunneling current is produced, it is measured by a preamplifier which converts the current signal into a voltage signal with a gain of 10^6 - 10^9 VA^{-1} . The tunneling current, which is exponentially dependent on the separation between tip and sample, as was deduced in equation 2.18 (chapter 2), can be linearized by a logarithmic amplifier to improve the dynamic range. The latter is useful when the scan is carried out on rough surfaces; however, on atomically flat surfaces the logarithmic linearization is no longer needed. The next step in the block diagram is the comparison of the measured current $U_t(I_t)$ with the demanded current or set-point current $U(I_{sp})$, which is introduced by the user through the computer-controlled DAC (typical values between 10 pA and 10 nA).

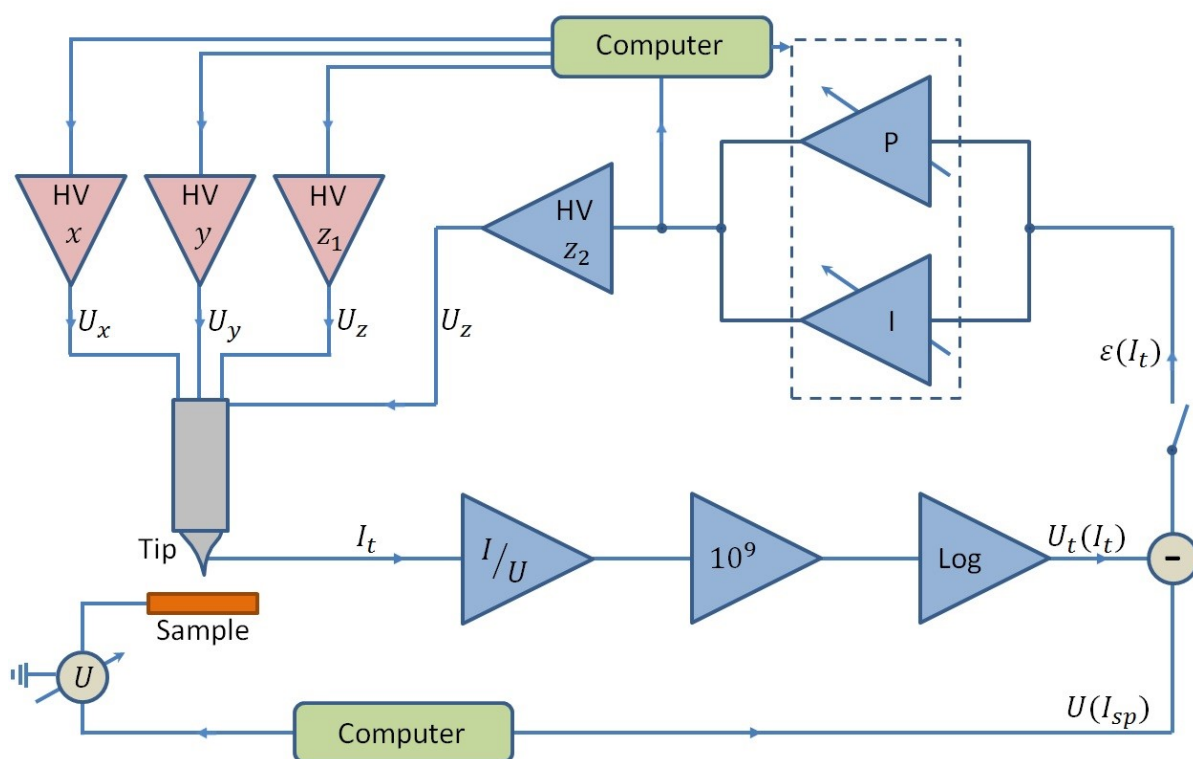


Figure 3.4: Block diagram of STM feedback circuit.

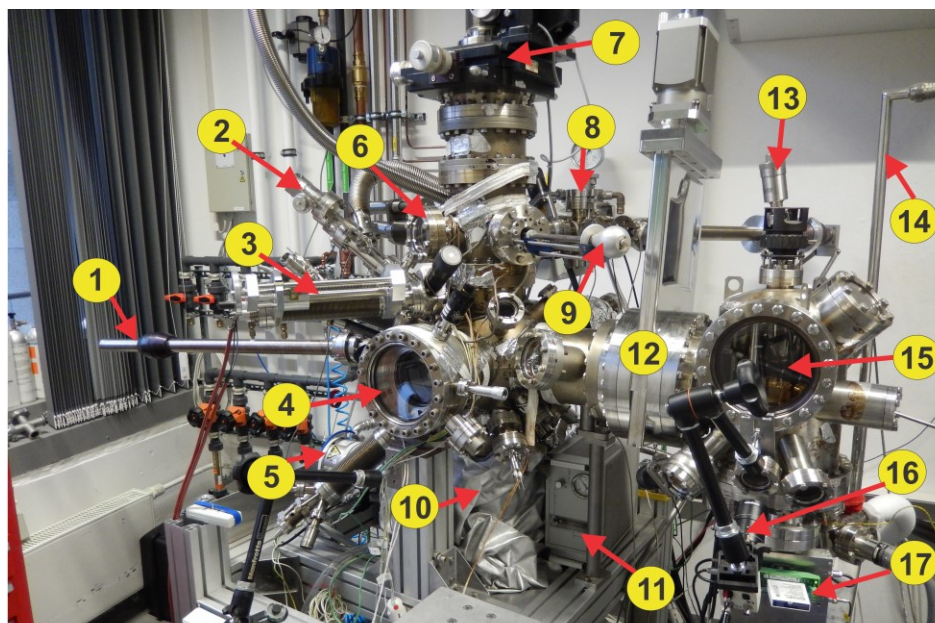
From the comparison of both current signals a resultant error signal is produced $\varepsilon(I_t)$. It contains the information about the deviation of the measured current from the desired one. The error signal is further fed into feedback amplifiers which usually consist of a proportional amplifier (P) and an analog integrator (I). The feedback signal is finally fed into a high-voltage (HV) amplifier which generates the signal, which is applied to the z piezoelectric drive with the purpose to move the tip up-down as is required in the constant-current operation mode (see section 2.5). A different circuit is used in order to let the tip scan in the x - y plane (pink amplifiers in the block diagram). This could be done by a computer-controlled DAC or by a synchronized ramp generators with a subsequent signal amplification by high-voltage amplifiers [27,28,65].

3.2 Variable-temperature STM system (VT-STM)

3.2.1 Overview

The VT-STM system is conceived as an advanced tool for the in-depth investigations of molecular structures on surfaces. It is particularly interesting for studies related to self-assembly, anchoring, nanostructures, as well as the study of orbital distribution in molecules and its local density of states. The VT-STM system is a UHV system ($p \sim 10^{-10}$ mbar) that includes a preparation-analysis chamber with an entry-lock chamber and an STM-chamber (see figure 3.5). The entry-lock chamber (8) is the bridge and door

between the UHV system and the external environment. It is used to get a sample/tip into UHV and vice versa. This chamber has a small volume in order to be vented and pumped relatively fast in comparison to the whole UHV system. The entry-lock chamber is connected via a separation valve and a rod-manipulator with the biggest chamber of the system, which is the preparation-analysis chamber. The vacuum in the preparation-analysis chamber is sustained by a turbo molecular pump (5) and by a combination of titanium sublimation and ion pumps (10). The turbo pump is used mostly when highly degassing processes inside the chamber are carried out. The sublimation pump is used occasionally for improving the vacuum conditions and the ion pump works most of the time due to its power to sustain the vacuum in the whole system and its low noise, which are crucial aspects during STM data acquisition. This chamber has different elements for the sample/tip manipulation, preparation and analysis. Among the main elements, there are three manipulators: the vertical (7), the horizontal (1) and the so-called wobble stick (9). They catch and move the sample/tip to different stations inside the system. The vertical manipulator has a resistive heater for sample/tip treating as well. The stations for sample/tip preparation are: the e-beam heater stage (6), which lets the sample/tip be flashed (see section 3.2.2); the sputtering stage, where the sample/tip is cleaned through the momentum transfer of argon ions which come from a sputter gun (2); the evaporation stages, where nanostructures and films are grown on the sample/tip surfaces. There are commercial e-beam evaporators used mostly for metal-evaporation and home-made evaporators used for molecular-evaporation (3). Additionally, the biggest chamber of the system has tools for chemical and structural analysis, such as in particular: mass spectroscopy, which provides information about the chemical compounds and partial pressures inside the UHV system; Auger spectroscopy, which helps to determine the chemical elements present on the sample; a quartz microbalance used for monitoring the quantity of material deposited on the sample surface; and a low energy electron diffractometer (LEED, 4) for determining the surface structure of the sample. The preparation-analysis chamber is connected *via* a separation valve (12) with the STM chamber (15). The vacuum in the STM chamber is maintained additionally for an ion pump. The stage for the STM-head, the eddy current damping system and the helium flow cryostat are located inside the chamber. Furthermore, a carousel for sample/tip storage and exchange is located in one side of the chamber. This chamber has two short manipulators: one for locating the sample/tip into the STM-head and a second one for connecting-adjusting the sample with the cooling wires (13). Moreover, through the STM chamber the electronic control system is connected (see section 3.1.3). A helium transfer line (14) is plugged in a feedthrough of the STM-chamber, which is further externally connected to a helium flowmeter (11).

**Preparation chamber:**

- 1) Horizontal manipulator
- 2) Sputter Gun
- 3) Evaporator (e-beam)
- 4) LEED
- 5) Turbo molecular pump
- 6) e-beam heater stage
- 7) X-Y positioner
- 8) Entry-lock chamber
- 9) Wobble stick (manipulator)
- 10) Titanium sublimation and ion pumps

Not visible parts:

Auger spectrometer
Mass spectrometer
Quarz microbalance

Microscope chamber:

- 11) Helium flowmeter
- 12) Separation valve
- 13) Sample-stage adjuster
- 14) Helium transfer line
- 15) STM chamber
- 16) Video Camera
- 17) Femto amplifier

Not visible parts:

Ion pump
Helium flow cryostat

Figure 3.5: Variable temperature STM system (IFW-Dresden).

Figure 3.6 is a detailed sketch of the helium flow cooling circuit in the VT-STM. The helium flow system is composed, in principle, of a helium dewar (typically of about 100 liters), the cryostat (inside the STM-chamber), flux-meters and regulators, a rotary pump (which sucks the helium from the dewar), and transfer lines which connect all the mentioned elements as is shown in the schematic. The helium (^4He) cryostat allows for stable temperatures between 300 K and 20 K.

The general characteristics of the VT-STM are listed in table 3.1.

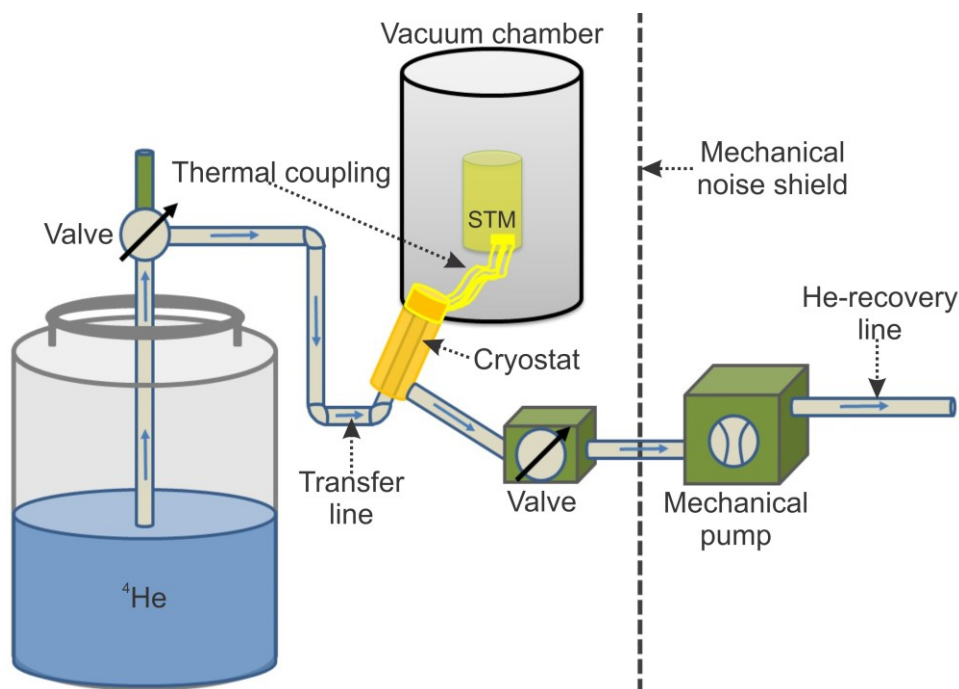


Figure 3.6: ^4He flow cooling system schematic for the VT-STM.

Atmosphere	UHV - $p \sim 10^{-10}$ mbar
Temperature of operation	20 K – 300 K
Measurement time	~ 70 hours
Scanning range	$3.4 \mu\text{m} \times 3.4 \mu\text{m}$
Time of sample\ tip exchange	~ 20 min
Damping system	Metallic springs and eddy current
Energy resolution	> 10 meV

Table 3.1: Characteristics of the VT-STM system.

3.2.2 Important working steps

Sample/tip load into the system: In order to load a sample/tip into the system, the first step is to put the sample/tip into the entry-lock chamber (8). In the entry-lock chamber, the sample is held by a manipulator. After that, the chamber is pumped for approximately 15 minutes until a pressure of the order of 10^{-7} mbar is reached. Subsequently, the

sample/tip should be transferred to the preparation-analysis chamber as fast as possible with the purpose of keeping the UHV in the system. The sample/tip is received in the vertical manipulator (7) of the preparation-analysis chamber to further be transferred at any stage either for preparation or analysis.

Sample/tip transfer into the system: Once the sample/tip is in the vertical manipulator (7), it can be transferred to the e-beam heater stage (6) with the assistance of the wobble stick (9). For the rest of the preparation and analysis procedures, the sample/tip is moved to the corresponding location and held beside by the vertical manipulator. After the desired preparation and analysis, the sample/tip can be picked up and further transferred to the STM chamber by the horizontal manipulator (1). In the STM chamber the sample/tip is first received in a carousel and then moved into the STM-head by a wobble stick.

Sample/tip preparation into the system: A sample/tip can be treated in the e-beam heater stage (6) with the purpose of being thoroughly cleaned by intensive heating to about 2000 °C. It requires, of course, sample/tip materials of high melting temperature at low gas pressure such as tungsten or molybdenum. The e-beam heater stage works with two external power supplies: one heats a tungsten filament in order to produce electronic emission and another accelerates the free electrons to the sample/tip which causes considerable heating. A sample/tip can also be cleaned by the sputter gun. In this case argon ions bombard the sample surface causing the impurities removal as well as surface damages. Therefore, treated surfaces require normally a subsequent annealing procedure. The annealing temperature depends on the nature of the sample/tip material. In the evaporation stages, as was mentioned above, there are commercial evaporators which use a similar procedure of the e-beam heater stage in order to evaporate metals and there are home-made evaporators which use resistive heating for the evaporation of organic material (3). In both cases the growth of films is monitored by a quartz microbalance.

3.2.3 Problems

The VT-STM was originally offered by Omicron [66] as a commercial system, whose most important feature was the possibility to carry out measurements at different temperatures, taking into consideration a temperature range from 1500 K to 25K by cooling down the sample. The VT-STM permits us to perform experiments with a cold sample (down to 20 K), while the tip remains at room temperature. Such conditions render the SP-STM measurements particularly difficult. In order to overcome the mentioned limitation, a home-made tuned STM-head has been developed at the IFW-Dresden (see figure 3.7) [65,67,68]. The STM-head shown in figure 3.7, from the outer to the inner sections, is based on a thermal radiation shield, a stainless steel frame for thermal decoupling, and an STM-body. The body is made of CuSn6P with gold coating, which hosts the sample stage and the coarse approach system (piezo stacks-motors,

sapphire prism, tube scanner, and tip-holder). This design permits the cooling down of every element of the body down to 20 K through the thermal connections located on its top. Furthermore, the radiation shield is cooled down in order to avoid thermal radiation to the body.

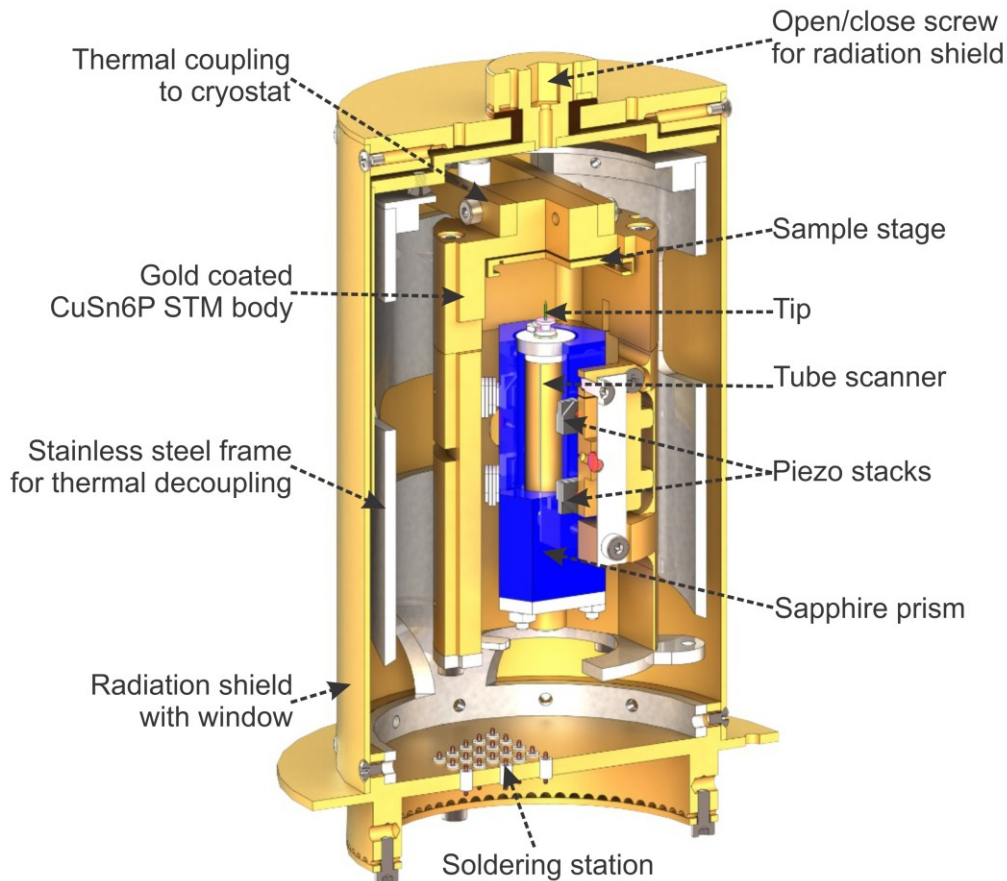


Figure 3.7: STM-head modified for Omicron VT-STM, IFW-Dresden (image by Danny Baumann).

Figure 3.8 shows the home-made STM-head mounted in the original Omicron stage. The stage is based on four cylindrical columns, with springs inside the columns that are employed for hanging the STM-head and thus damping mechanical noise. Additionally, these columns fix the stage to a vacuum flange. There is also an eddy current vibration isolation system that helps the mechanical noise attenuation. The home-made STM-head has a radiation shield which avoids temperature instabilities in the STM-body, as well as electromagnetic noise which potentially decreases the resolution.

The home-built STM-head developed at the IFW-Dresden and further installed in the VT-STM often presented non-optimal operation for the coarse approach system. The

origin of the problem was identified in the damage of the piezo stacks, which are the parts responsible for the tip-approach through the movement of the sapphire prism.

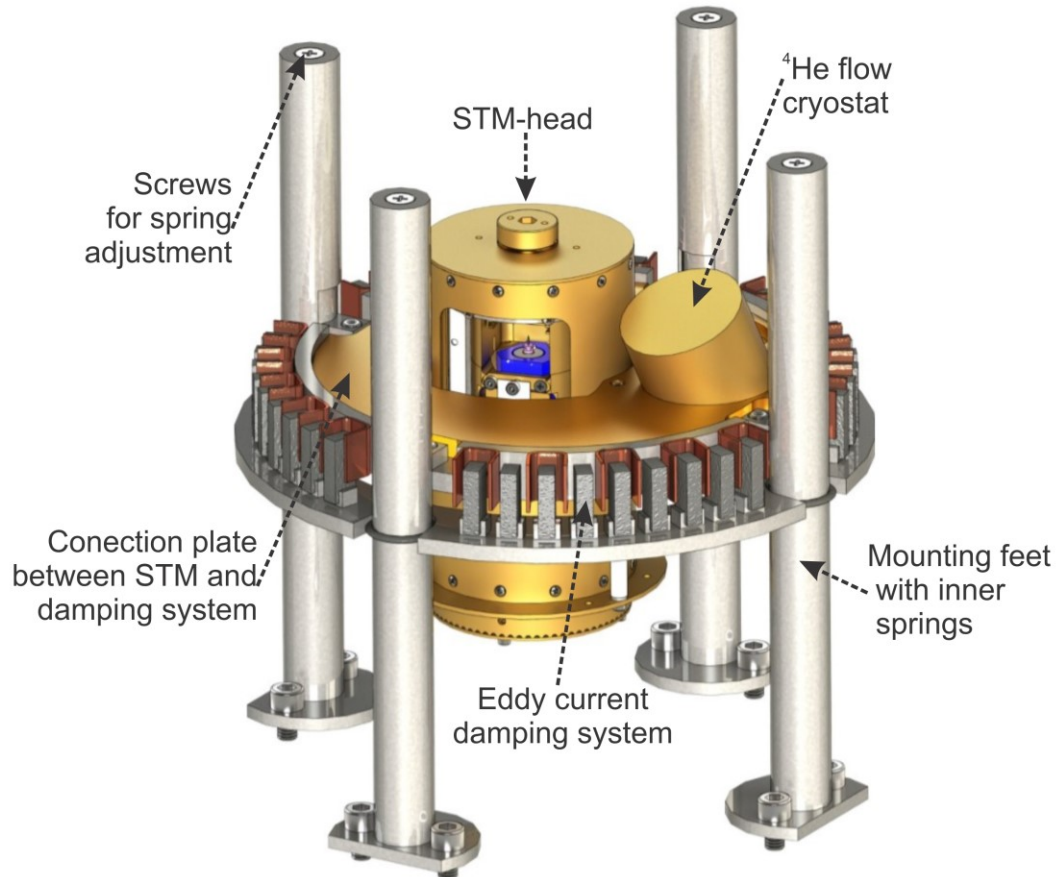


Figure 3.8: Schematic of the modified Omicron VT-STM, IFW-Dresden (image by Danny Baumann).

The piezo stacks are home-made actuators built by gluing four piezo plates, one over the other, and on top a plate of aluminum oxide (Al_2O_3), as it is depicted in figure 3.9 (a). The piezo stack shown in figure 3.9 (a) has an approximate size of $7 \times 7 \times 2 \text{ mm}^3$ and was used for STM experiments at a temperature range of room temperature (RT) to 20K. Figure 3.9 (b) shows a bottom view of the piezo stack, indicating damage in the plates which were in contact with the walls of the STM-body. The latter damage is due to the high stress suffered by the piezo electric material, which is likely to be promoted by different dilatation-contraction properties of the other two materials which are in contact to it, the conductive glue (EPO-TEK H20E [69]) and the walls of the body (made of CuSn6P).

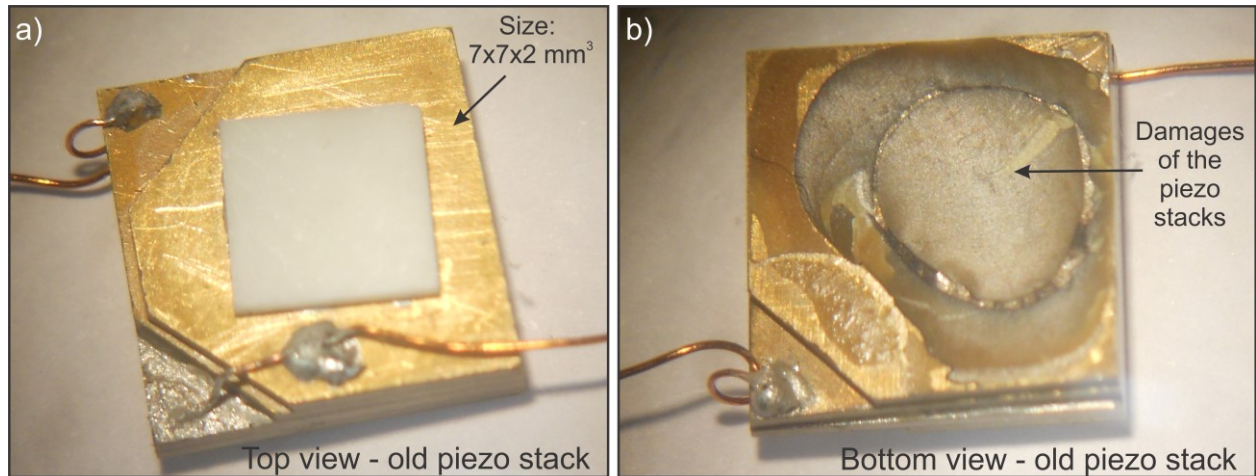


Figure 3.9: (a) Damages in the piezo stacks of the home-built STM-head, top view, (b) bottom view.

With the purpose to extend the life time of the piezo stacks, different strategies were taken into account: i) the cooling down of the STM-head was held slowly (six hours approximately), in order to guaranty an homogeneous cooling of the STM-head and thus avoiding inhomogeneous stress due to improper thermalization in all the parts composed by different materials, ii) before applying the alternating high voltage signal to the piezo stacks which makes them move (see figure 3.2), the capacitance of each piezo stack was verified to be at the correct value according to the temperature of the STM-head (~ 1.2 nF, $T = 20$ K) and iii) new piezo stacks were built smaller ($5 \times 5 \times 2$ mm³) in order to reduce the chance of stress and to facilitate the cooling down process (see figure 3.10).

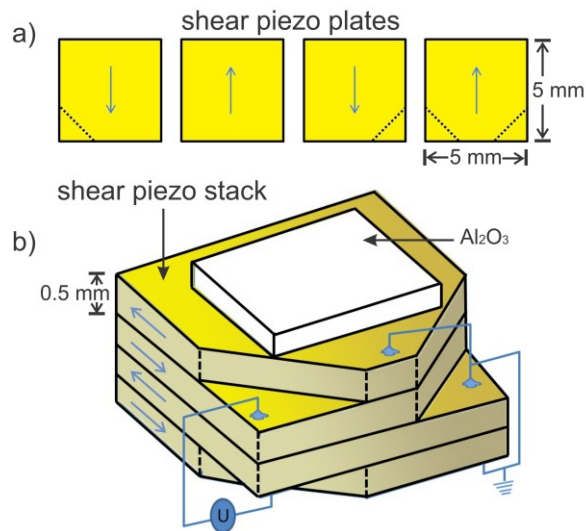
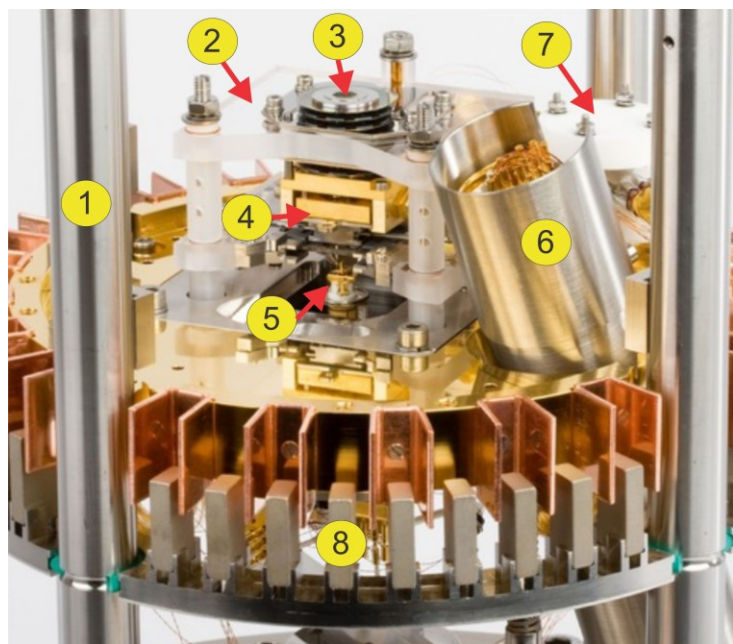


Figure 3.10: Construction of a piezo stack for the home-made STM-head.

Each new piezo stack had a capacitance between 2.08 and 2.27 nF at room temperature and a capacitance of about 1.2 nF at 20 K. Once the stacks were installed in the body, they were also tested in terms of their electrical isolation. The measurements evidenced a resistance associated to every stack of the order of giga-ohms, when connected to a voltage of 500 V.

Although the VT-STM operated correctly at room temperature and for a couple of days at 20 K, it failed again. The problem in this case is not clearly known; it may be due to a geometrical issue in the design of the STM-body. Thus, the solution was to then mount the original Omicron STM-head shown in figure 3.11.

This Omicron STM-head works with the tip at room temperature and the sample between RT and 20 K. Therefore, it is well suitable primarily for studies of relatively big structures such as molecular complexes with broad electronic states. The STM-head in this case does not have a radiation shield, which makes it necessary to cover the window-flanges with aluminum foil in order to prevent the entrance of external electromagnetic radiation.



- | | |
|---------------------|--------------------------------|
| 1) Mounting feet | 5) Tube scanner and tip |
| 2) Omicron STM-head | 6) He-flow cryostat |
| 3) Sample adjuster | 7) Thermal connection bridge |
| 4) Sample stage | 8) Eddy current damping system |

Figure 3.11: Original Omicron STM-head [66].

3.3 Low-temperature STM system (LT-STM)

3.3.1 Overview

The LT-STM is a home-built system [51] that combines ultra-low temperature (down to 300 mK), ultra-high vacuum (UHV), and magnetic field (up to 9 Tesla) in the STM experiment. These experimental capabilities show that the LT-STM is a system suitable for investigations in the field of strongly correlated systems, unconventional superconductors, and quantum matter in general. The UHV environment provides the opportunity to perform SP-STM experiments, which is considered a promising tool in the field of condensed matter to elucidate new physical phenomena and characterize at the atomic scale magnetic structures of interest for future applications in spintronics. In the framework of this thesis, SP-STM has been successfully demonstrated within this machine for the first time.

Figure 3.12 shows the schematic of the LT-STM. A welded metallic frame connects all the components with the damping system, which consists of three equidistant columns (in blue), each with an air-buffer and an air-level regulator on top. The most visible part is the cylindrical cryostat-barrel, which contains a commercially modified Janis cryostat [51,70]. The Janis cryostat counts with three ^4He reservoirs with a total volume of 350 liters which are surrounded by isolation shields. Furthermore, the cryostat possesses a ^3He single shot system. The combined cryostat allows temperatures in the range of 50 K to 300 mK in the STM experiment. In between the cryostat and the metallic hexagon (bottom part of the metallic frame, see figure 3.12) three UHV chambers are located. The central UHV chamber, or the so-called STM chamber, is employed for the sample/tip exchange with the STM-head; additionally, this chamber has a carousel for the storage of samples and tips. A second chamber, the so-called preparation chamber, is used for the standard preparation of tips and samples. This chamber has a connection to an entry-lock chamber employed to exchange the sample/tip between the UHV system and the outer environment. The third chamber is under preparation and will perform structural analysis with low energy electron diffraction (LEED) and chemical analysis with Auger spectroscopy.

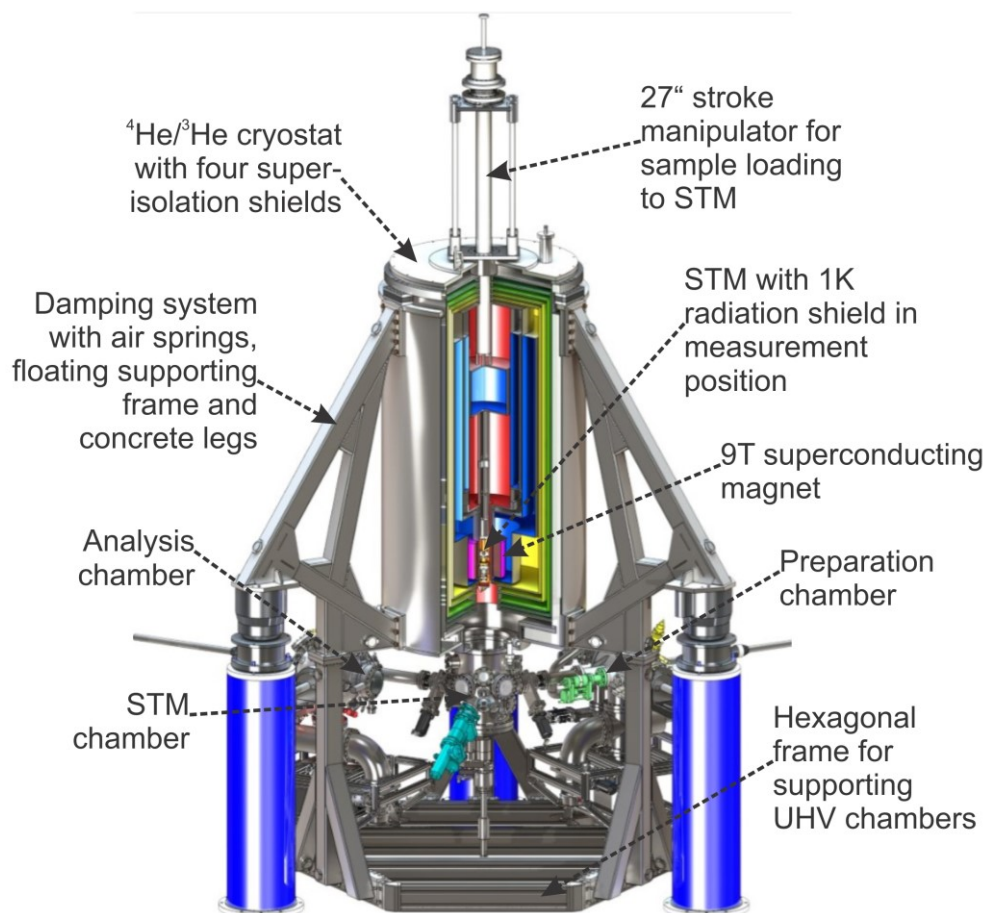


Figure 3.12: Home-built low temperature STM (LT-STM) scheme, IFW-Dresden (image by Danny Baumann).

The preparation chamber shown in figure 3.13 (6-14) contains most of the tools for sample preparation. The vacuum in this chamber is sustained by a turbo molecular pump and an ion pump (6) in a similar way as was described in section 3.2.1 for the VT-STM. The chemical compounds inside the chamber and their partial pressures are monitored by a mass spectrometer. In the preparation chamber there are three manipulators: the horizontal manipulator (14) employed to bring the sample/tip to the STM-chamber; the Y-Z positioner (8), which moves the sample/tip to the different stages of preparation (it also has a resistive heater); and the wobble stick (12) used to put the sample/tip in the e-beam heater stage (7). The different stations for sample/tip preparation are: the e-beam heater stage (7) used for sample/tip flashing, the argon sputtering stage (11, 13) suitable for sample cleaning *via* ion bombardment, and the evaporation stages (e.g. 10) where the nanostructures are grown on the sample/tip surface. A valve (5) connects the preparation chamber with the STM-chamber (1). The STM-chamber is used to exchange the sample/tip with the STM-head, which is located

later in the measurement position (see figure 3.12) for data acquisition. The vacuum in this chamber is sustained additionally by an ion pump (2). This chamber is designed to have evaporators as in (3) with the purpose to grow structures while the sample is at low temperatures. The sample/tip manipulation is carried out by a wobble stick and a vertical manipulator indicated in (4). The latter lets the adjustment of a carousel for sample storage and also opens/closes the radiation shield in the STM-head.

The LT-STM characteristics are summarized in table 3.2.

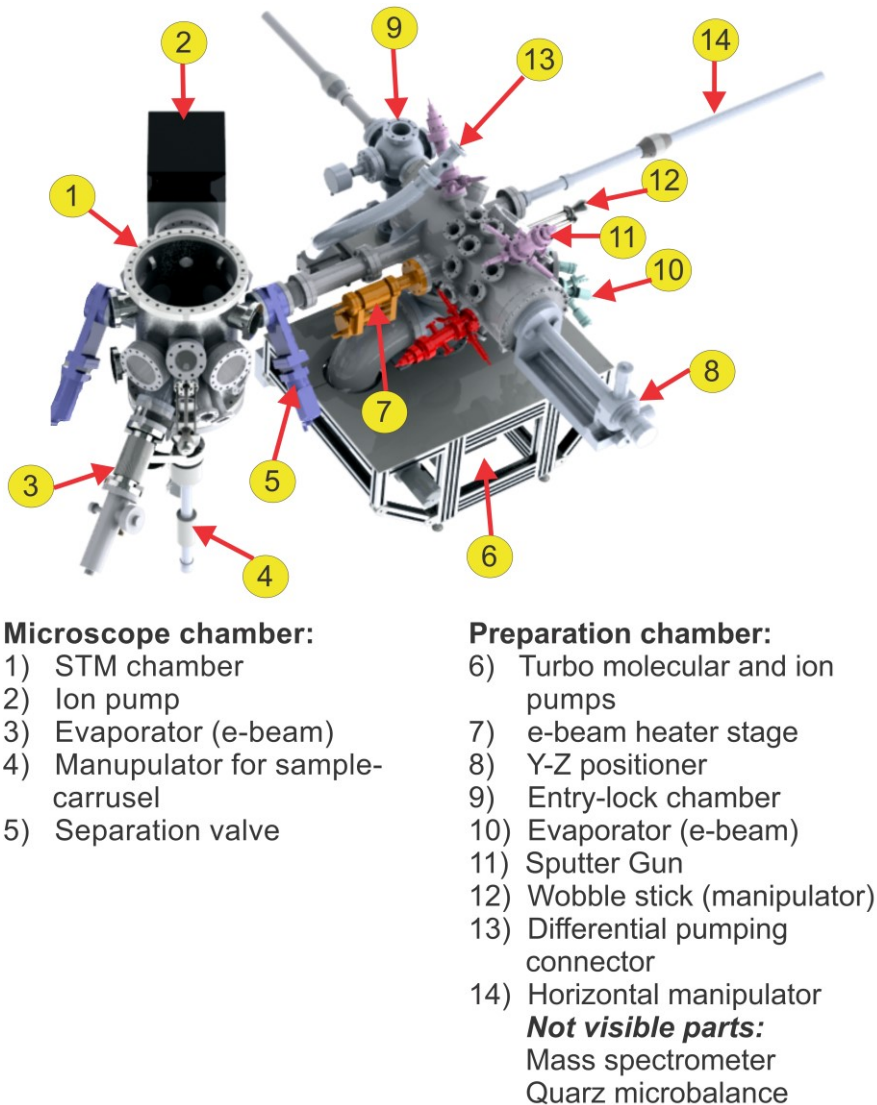


Figure 3.13: Microscope and preparation chambers of the LT-STM, IFW-Dresden (image by Danny Baumann).

Atmosphere	UHV - $p \sim 10^{-11}$ mbar
Temperature of operation	0.3 K – 50 K, 300 K
Measurement time	~ 60 hours
Scanning range	$0.8 \mu\text{m} \times 0.8 \mu\text{m}$
Time of sample\tip exchange	~ 2 hours
Damping system	Air-buffer damping
Energy resolution	0.1 meV

Table 3.2: Characteristics of the LT-STM system.

3.3.2 Important working steps

Sample/tip load into the system: Similar procedure described in section 3.2.2 of the VT-STM is used in the LT-STM. The first step is to put the sample/tip into the entry-lock chamber (9). In the entry-lock chamber, the sample is held by a manipulator. After that, the chamber is pumped for approximately 15 minutes until the pressure decreases at the order of 10^{-7} mbar. Subsequently, the sample/tip needs to be transferred to the preparation chamber as fast as possible in order to keep the UHV in the system. The sample/tip is received in the Y-Z positioner (8) of the preparation-analysis chamber to further be transferred at another stage for preparation.

Sample/tip transfer into the system: The sample/tip hosted in the Y-Z positioner (8) can be transferred to the e-beam heater stage (7) assisted by the wobble stick (12). For the rest of the preparation and analysis procedures, the sample/tip is moved to the corresponding location and held besides by the Y-Z positioner. After the desired preparation, the sample/tip can be picked up and further transferred to the STM chamber by the horizontal manipulator (14). In the STM chamber the sample/tip is received in a carrousel first and then moved into the STM-head by a wobble stick.

Sample/tip preparation into the system: A sample/tip can be cleaned at the e-beam heater stage (7) by short-time high temperature heating to about 2000 °C. The operation is similar to the one described in section 3.2.2. For soft metals the preparation chamber contains a sputtering stage (11). In the evaporation stages, there are commercial e-beam evaporators, for instance the iron evaporator (10). The metal evaporators use the e-beam heating principle to evaporate metals such as Fe, Cr, Ni, etc. The quantity of material deposited on the substrate surface is controlled by the ionic emission current, which is

measured by an electrode-collector at the end of the evaporator, in combination with a quartz microbalance.

3.3.3 LT-STM for Spin-Polarized STM

The LT-STM system was built for spin-polarized STM studies. These highly demanding measurements require conditions like UHV in the low-pressure regime of 10^{-10} mbar, temperatures (liquid-helium temperatures) below the Curie/Néel temperature of the sample and an extreme noise isolation (mechanic, electromagnetic). Additionally, the system should have the option to prepare magnetic samples as well as magnetic tips in UHV.

In particular, the part of the thesis related to the investigation on iron nanostructures included showing that SP-STM for this system for the very first time can be employed (see chapter 6).

4 Substrates and tips: preparation

4.1 Substrates

4.1.1 Highly oriented pyrolytic graphite (HOPG)

Pyrolytic graphite can be experimentally obtained by graphitization, based on the heat treatment of pyrolytic carbon or by chemical vapor deposition. However, when it comes to the highly oriented pyrolytic graphite (HOPG), the annealing of pyrolytic graphite under compressive stress at approximately 3300 K is required. The commercial HOPG samples are based on a polycrystalline material with large grain sized and good orientation with respect to the surface plane [71,72].

HOPG is a layered material where each layer contains carbon atoms arranged in a honeycomb lattice. The atomic separation within the layer is 0.142 nm, while the separation between layers is 0.335 nm (see figure 4.1). Considering sp^2 orbital hybridization, every carbon atom in the honeycomb lattice creates three covalent bonds (σ bonds) with its nearest neighbors. The overlap of the $2p_z$ orbitals perpendicular to the layers produces delocalized π electrons that are free to migrate within the layer, resulting in the electrical conductivity of graphite. Furthermore, the graphene layers are bounded through weak van der Waals bonds, which allows layers to be easily separated [73]. The latter renders HOPG samples easily cleavable, which means that by just peeling off the top layers while using adhesive tape, large clean atomically flat surfaces are obtained. The HOPG fresh surface presents the advantage of being relatively inert to oxidation. The above mentioned characteristics make HOPG suitable for STM investigations, as its well-known structure and its high symmetry are useful for scanner calibration at the nanoscale mainly in the x and y coordinates. The z coordinate is not recommended for calibration due to the variability present in the interlayer spacing promoted by tip interaction and also by considering the weak bonding between graphene layers [74,75].

STM image interpretation: In order to understand the images of HOPG obtained through STM, it is necessary to review both the structural and the electronic characteristics of the graphite. In this sense HOPG is built in a so-called ABAB stacking structure, which means that the neighboring layers are shifted relative to each other, as highlighted in figure 4.1.

Two types of carbon atoms could be identified in every layer: From one side, those which have a direct neighbor in the layer below (site 1) and from the other side those which do not (site 2). Considering that STM bases its measurement in the electronic density of states resulting in the top layer of HOPG, it is necessary to determine the different density of states that carbon atoms would present in sites 1 and 2. Thus, band theory calculations suggest that the amplitude of the Bloch wave functions at site 1 is smaller than at site 2. In fact, at site 1 the density of states is reduced around the Fermi level because of the bonding and antibonding interaction between π orbitals from the top-last layer and the underlayer [76]. Therefore, an STM image of HOPG would differ from the real topography due to the above-mentioned considerations.

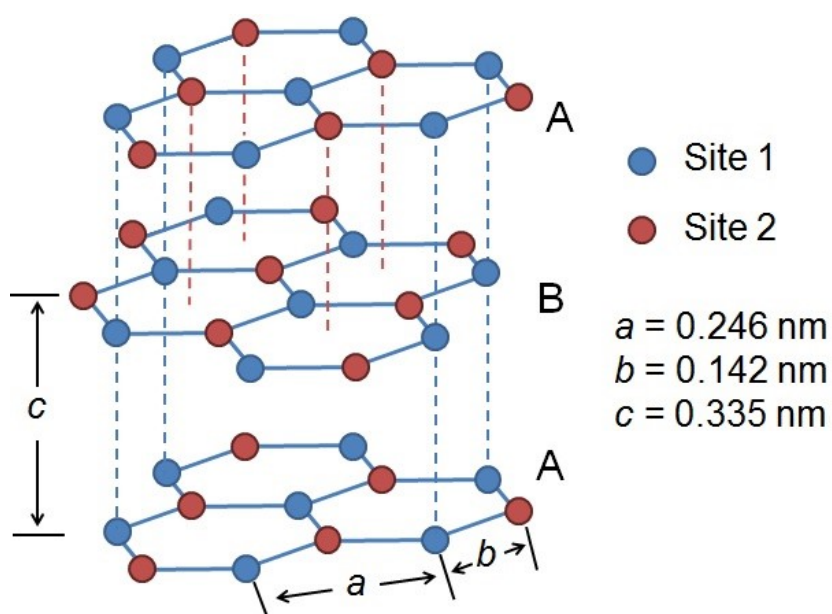


Figure 4.1: Highly oriented pyrolytic graphite (HOPG). Laminal structure ABAB and type of carbon atoms (site 1, site 2).

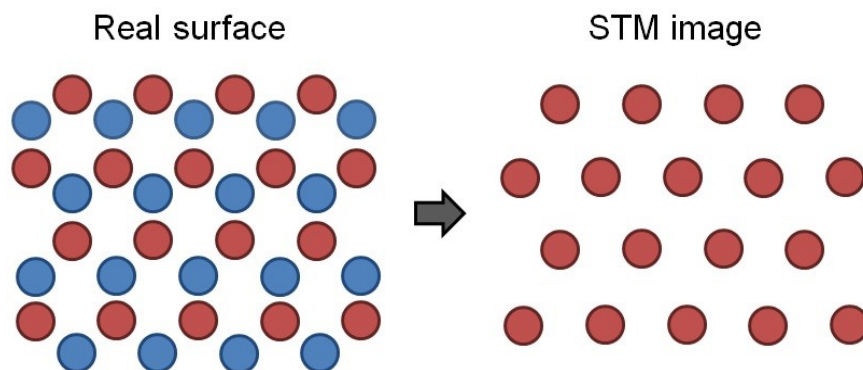


Figure 4.2: Schematic of the real HOPG surface and the HOPG surface obtained by STM.

Figure 4.2 depicts the top view of an HOPG sample; on the one hand representing the real hexagonal lattice (real HOPG surface) and on the other hand showing the triangular lattice that STM reveals. It is worth mentioning that sometimes STM also shows the real surface when, by chance, the top layer is decoupled from the bulk. Figure 4.3 (a) shows a typical STM image revealing the HOPG surface, hereby presented in order to obtain a scanner calibration in the x and y coordinates. Additionally, in figure 4.3 (b) the atomic corrugation along the arrow in (a) is also shown.

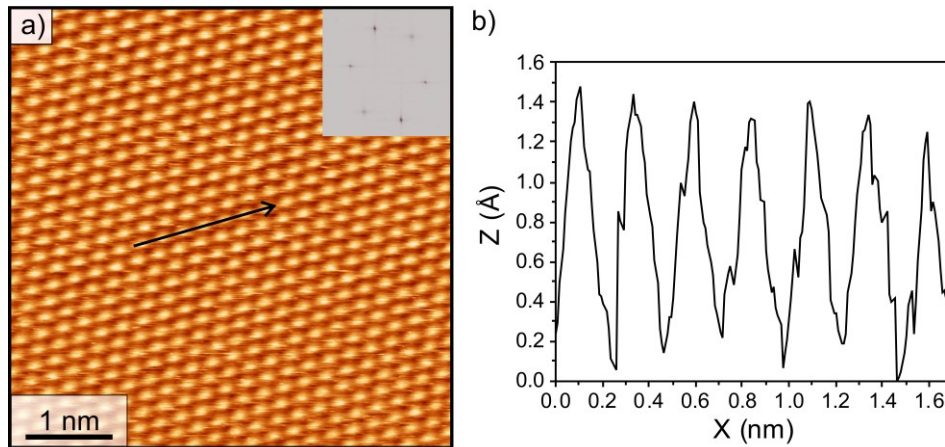


Figure 4.3: (a) HOPG surface revealed by STM (inset: Fast Fourier Transform FFT), (b) line profile indicated from the arrow depicted in (a).

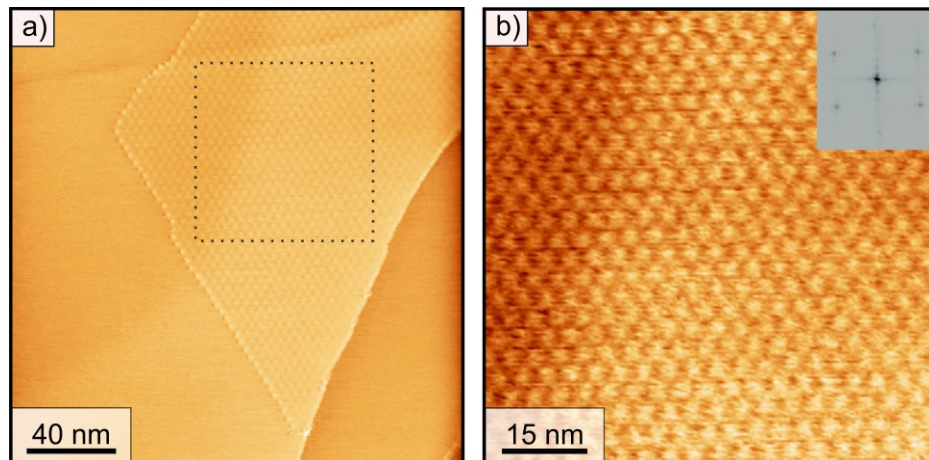


Figure 4.4: (a) HOPG-super structure revealed by STM, (b) Digital zoom-in from the region of interest depicted in (a) (inset: FFT).

HOPG super-structure: STM images sometimes also show ordered patterns with dimensions larger than the expected for HOPG. These kind of images are directly related to the graphene layers organization, which are angularly rotated among them creating

interference patterns (Moiré patterns). These patterns generally depend on the rotation angle [77,78]. Figure 4.4 (a) shows a HOPG surface where one graphene layer creates a Moiré pattern with a lattice parameter of approximately 4.7 nm (see figure 4.4 (b)).

4.1.2 Au(111)

Gold is the soft metal with the highest malleability and ductility among all elements, being a noble metal non-reactive to air, water and mostly all acids. For investigative purposes, single gold crystals can be grown like a film on a substrate (e.g. mica, glass) or like a bulk onto a sample. Among the different techniques employed for gold sample production, there are: physical vapor deposition in the case of thin films, and the Bridgman-, Czochralski- and zone melting techniques in the case of bulk samples [79,80]. After the single crystal production, surface cleaning is required for further investigations by using scanning probe techniques. One of the cleaning procedures is the flame annealing, which is a thermal treatment at approximately 650 °C under nitrogen atmosphere [81,82]. Furthermore, under vacuum conditions, cycles of sputtering with argon ions and subsequent annealing can be employed [80,83]. For this thesis, Au(111) single crystals were firstly sputtered with argon ions at 2kV using a filament current of 10 mA for 8 hours. After the sputtering process the crystals were annealed at 550°C at a chamber pressure of 5×10^{-9} mbar for 12 hours (see the typically observed surface reconstruction in figure 4.6).

Gold single crystals can be produced in different directions, for instance the most common are: Au(111), Au(100), and Au(110). However the Au(111) is the most densely occupied surface and exhibits a particular reconstruction which will be further described, particularly considering the importance of the experiments held with dinickel complexes in the present thesis.

A clean Au(111) crystal exhibits a surface reconstruction ‘herringbone’ or $22 \times \sqrt{3}$ in terms of its surface unit cell (see figure 4.5). The origin of this spatial reconstruction lies in the smaller number of nearest neighbors in the surface (nine instead of twelve in the bulk for an FCC lattice), thus the interatomic distances between the atoms in the top most layer are uniaxially reduced. In the most energetically favorable scenario, 23 surface atoms are packed in 22 bulk lattice sites. Due to this mismatch, some atoms are forced to move from FCC sites to HCP sites and to incommensurate bridge sites. Atoms located at the bridge sites between FCC and HCP stacking regions are slightly displaced in the z direction, causing striped contrast in STM images [84]. Figure 4.6 shows the typical surface exhibited by the Au(111) crystal, used in this thesis for the anchoring of dinickel complexes. Herringbone patterns in these images are a clear signal of the optimal surface cleanness. It is important to mention that the herringbone reconstruction shows two types of periodicities, one of about 30 nm (figure 4.6 (b)) and a shorter of about 7 nm (figure 4.6 (c)) [85].

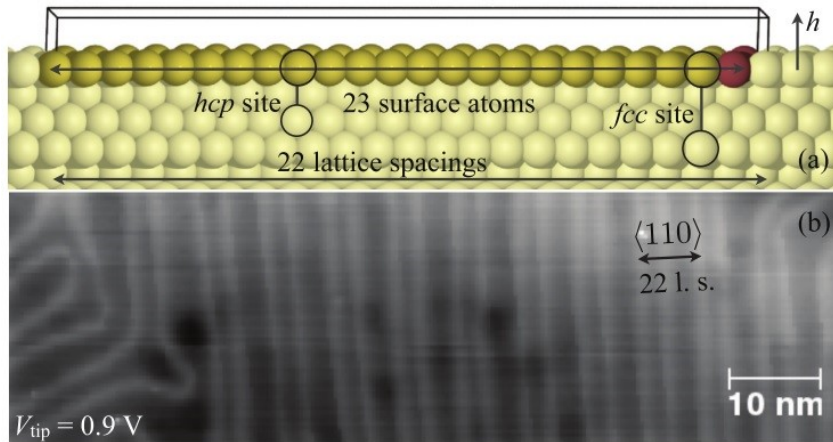


Figure 4.5: (a) Schematic representation of the $\text{Au}(111)/22 \times \sqrt{3}$ reconstruction, showing 23 surface atoms fit into 22 lattice sites, (b) STM image of the $\text{Au}(111)$ herringbone reconstruction. Taken from [86].

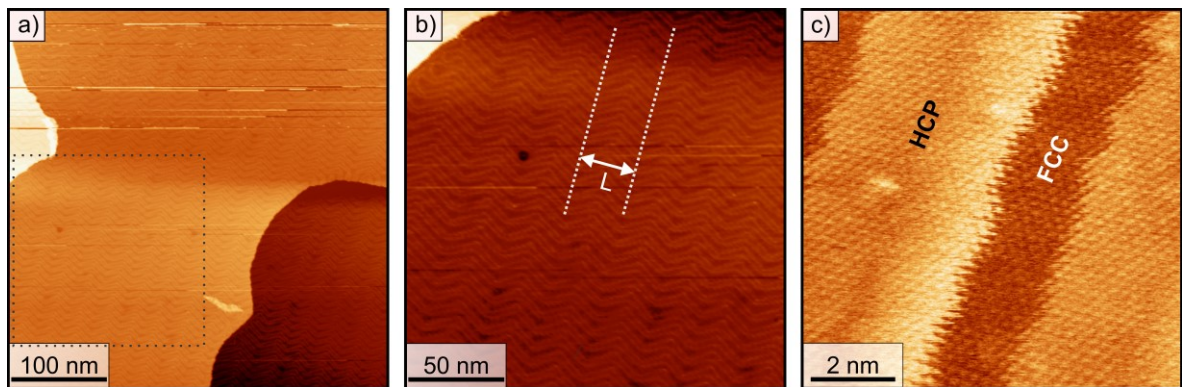


Figure 4.6: (a) $\text{Au}(111)$ surface reconstruction, (b) Digital zoom-in from the region of interest indicated by the dashed square in image (a) with $L \sim 30 \text{ nm}$ (images (a), b) measured by Sebastian Schimmel), and (c) atomic corrugation on $\text{Au}(111)$ in zones HCP and FCC.

4.1.3 W(110)

Tungsten metal is not found in its pure form in nature, being generally extracted from the ore Wolframite ($(\text{FeMn})\text{WO}_4$) that is converted to the trioxide and then reduced to the metal by reduction in hydrogen. Tungsten is relatively inert in the presence of oxygen, acids and alkalis. Such metal presents the highest melting point among all metals and, when pure, can be relatively easy to manipulate, although the presence of impurities renders tungsten extremely brittle and therefore, difficult to machine [72]. The samples of tungsten for investigative purposes are produced by employing the Bridgman-

, Czochralski- and zone melting techniques. The standard orientations commercially available are (001), (110) and (111). The standard accuracy of the orientation from the cut crystals is within less than 2° and by polishing an accuracy of less than 0.1° is achieved [79].

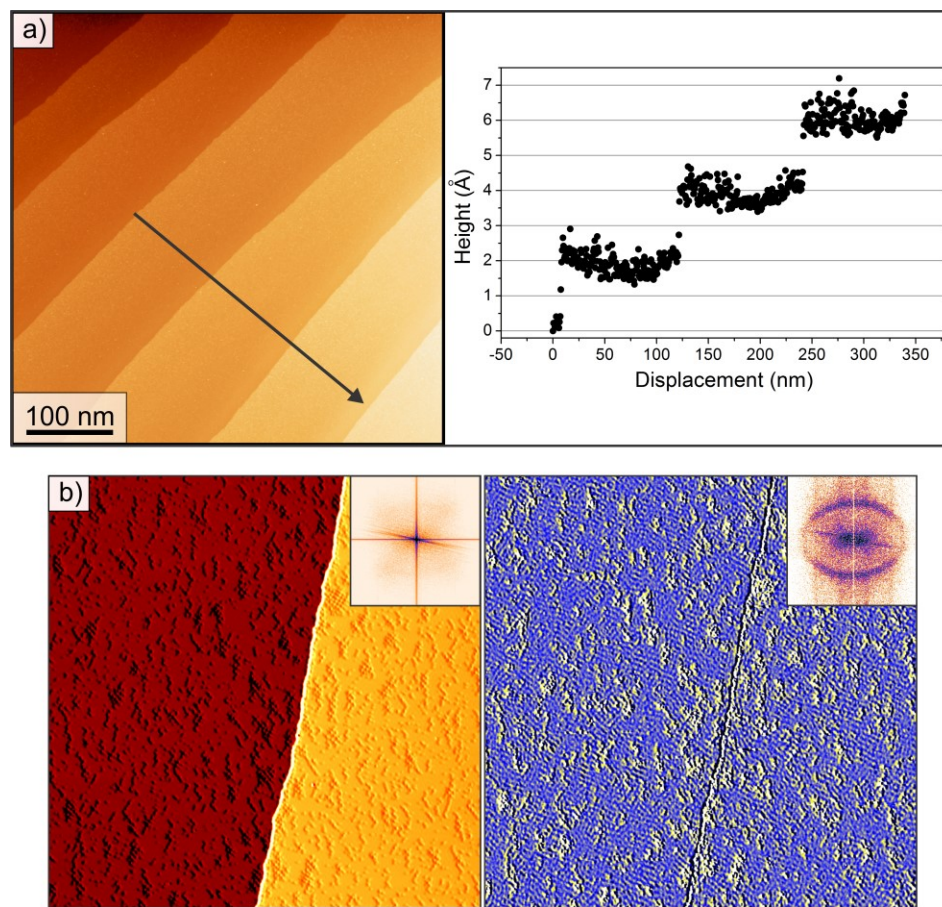


Figure 4.7: (a) Monoatomic steps of W(110) revealed by STM at room temperature, (b) zoom-in topography and differential conductance map in W(110) (image (b) measured by Torben Hänke, taken from [51]).

Different refractory metals are used as substrates for thin film experiments, mainly due to the low intermixing between the film and the substrate. W(110) is one of the most popular substrates for its densely packed surface. However, prior to STM experiments, an in-depth cleaning process is highly recommended due to the presence of carbon impurities on the crystal surface. One of the most successful procedures implies cycles of prolonged annealing ($T \approx 1500$ K for about 30 min) under oxygen atmosphere, followed by short high-temperature treatments, so-called flashes ($T \approx 2300$ K for about 15 s). During the annealing process in the presence of oxygen, the formation of the oxides CO and CO₂ from carbon (C) takes place. Such side products are gaseous substances and can be pumped after thermal desorption. Additionally, tungsten oxides are formed on the

surface and can only be removed by thermal desorption at temperatures above 2300 K [87,88].

Figure 4.7 (a) shows the typical surface from the single crystal W(110) used in this thesis to calibrate the z coordinate as well as substrate of the iron nanostructures studied in chapter 6. Monoatomic steps of about 0.2 nm height are observed in good agreement with literature [88]. Figure 4.7 (b) depicts, on the left side, a zoom of the usual W(110) topography and on the right side a differential conductance map, which reveals the Friedel electronic oscillation only observed in case of working with clean surfaces. In the insets of each image of figure 4.7 (b), the Fast Fourier Transforms (FFT) are shown. In the case of the topographic image (left), the FFT does not show periodical structures (the strongest signal is due to the atomic step). On the other hand, the FFT in the differential conductance map depicts features of the Friedel oscillations.

4.2 Tips

Tip preparation is one of the most crucial aspects to be considered in STM experiments. Tips determine the obtained data quality from the sample under study. Two aspects are relevant in the tip performance: its shape and its chemical composition [89]. In regards to the shape, the tip performance depends on the structure of the last atomic cluster of the tip involved in the tunneling process. In the ideal case, the tunneling current should flow through the last atom of the cluster. However, it is common to have the presence of more than one tunneling point in the tip, causing distortion or aberrations in the images. In regards to the second aspect, the chemical composition of the tip is affected by the original material that it is made of, as well as the possible contaminations present on the surface of the tip. The types of materials determine the density of states of the tip and thus the scope of the experiment. It is worth mentioning however, that contaminants on the tip surface, especially insulating oxide layers, can drastically modify the desired tip density of states leading to severe distortion of both STM and STS data. In the next section different tips employed in this thesis are described in terms of preparation and properties.

4.2.1 Tungsten (W) tips

Tungsten tips present a high mechanical stability due to the strength of the source material (W). Additionally, they are built reproducibly by electrochemical etching and possess a high and comparatively smooth density of states around the Fermi energy, which is optimal for the present STM studies [90]. W-tips are more suitable for experiments in vacuum conditions due to the formation of tungsten oxides in ambient conditions on the tip surface. Such oxides may later interfere with the STM measurements. The last but not least, W-tips, can be obtained from low cost polycrystalline wires.

Electrochemical etching is a widely used technique for the preparation of W-tips [91–93]. It consists of immersing a polycrystalline tungsten wire (normally of 0.3 to 0.5 mm in diameter), which acts as an electrode, into an electrolyte solution (e.g. 1M NaOH in distilled water) where a counter electrode is also present (see figure 4.8).

By applying an AC or DC voltage (4 – 8 V) between the two electrodes, the following chemical reaction takes place:

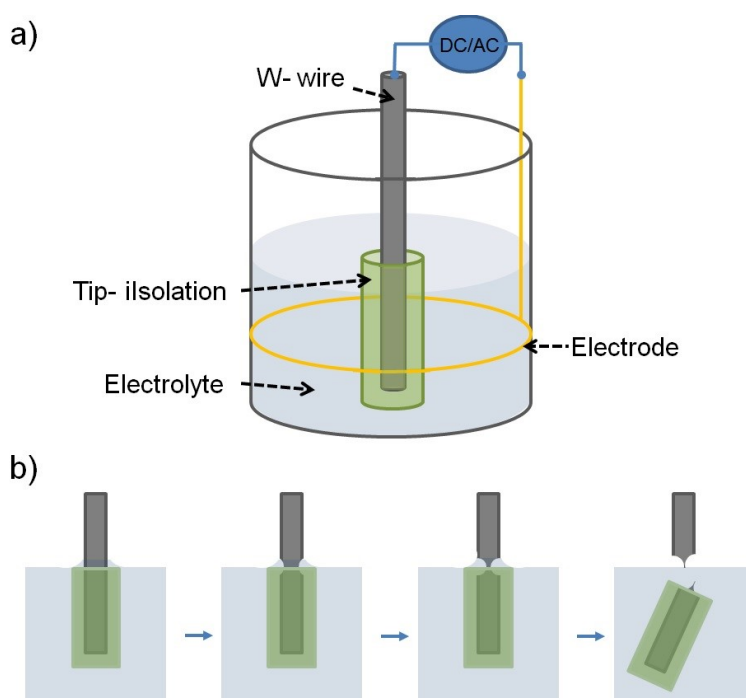
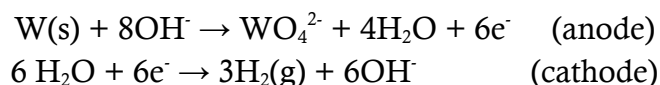


Figure 4.8: (a) Set-up for W-tips etching, (b) W-wire neck formation and tips production.

Under the electrochemical conditions afore mentioned, solid tungsten is oxidized, producing WO_4^{2-} ions which are soluble in water. In the cathode, water molecules are reduced to OH^- ions and hydrogen gas. The latter process causes the dissolution of tungsten and the formation of a neck on the wire, as shown in figure 4.8 (b). As the

diameter of the tungsten wire is extremely thin, the part of the wire immersed in the electrolyte solution gets separated from the outside wire by its own weight, presenting at the very end a very sharp tip of around 20 to 50 nm in diameter [94]. The tip is subsequently picked up and rinsed with distilled water in order to remove possible remainders or side products such as sodium hydroxide crystals, which may hinder the STM measurements. Additionally, the exposure of tungsten tips to air could potentially lead to the formation of tungsten oxides. To avoid such a problem, the tip is introduced into a UHV environment and exposed to a thermal treatment. Such a treatment consists of short time (5 -10 s) heating pulses of the tip by electron beam bombardment, reaching temperatures above 2300 K. After thermal treatment the W-tip desorbs its oxides on the surface, although the tip also becomes blunt, presenting curvatures typically of 1 μ m. However, it has been widely demonstrated that W-tips prepared as described above, permit the user to obtain atomic resolution and very stable spectroscopic measurements (see figure 4.9) [29,61].

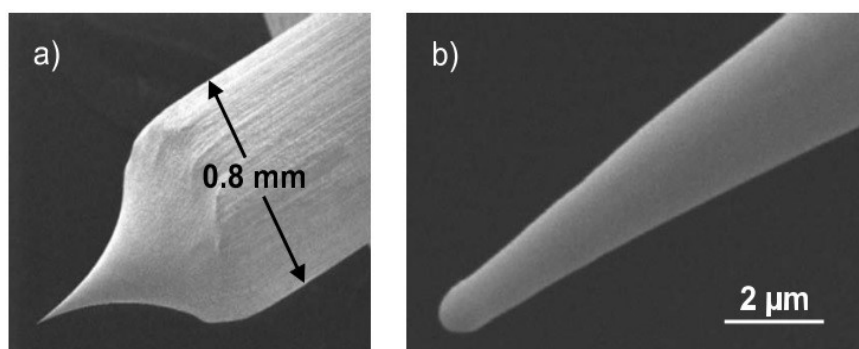


Figure 4.9: (a) SEM image of a W-tip once exposed to a high-temperature flash at $T > 2200$ K and b) higher magnification revealing a tip diameter of about 1 μ m. Taken from [29].

4.2.2 Platinum-iridium (Pt/Ir) tips

Pt/Ir-tips (80% Pt and 20% Ir) suit our requirements to work in ambient conditions due to their chemical inertia thanks to the presence of platinum (Pt). However, the iridium (Ir) contributes to the tip stiffness, making it harder. Although the Pt/Ir-tips have been prepared by using electrochemical techniques [95], the most successful method to obtain such tips is by simple mechanical cutting [96,97]. In which case, the first step in preparing Pt/Ir-tips is to clean the Pt/Ir wire, the pliers and the sharp edges of the wire cutter with ethanol. Afterwards, the Pt/Ir wire is firmly held with the pliers and the wire cutter presses (without cutting) at the desired tip length, forming a small angle with the wire (see figure 4.10 (a)). The cutter pulls the wire in the direction shown in figure 4.10 (a) until the tip is torn off, rather than cleanly cut (see figure 4.10 (b)). As well as the W-

tips, Pt/Ir-tips have widely demonstrated their applicability in high resolution STM data acquisition [98].

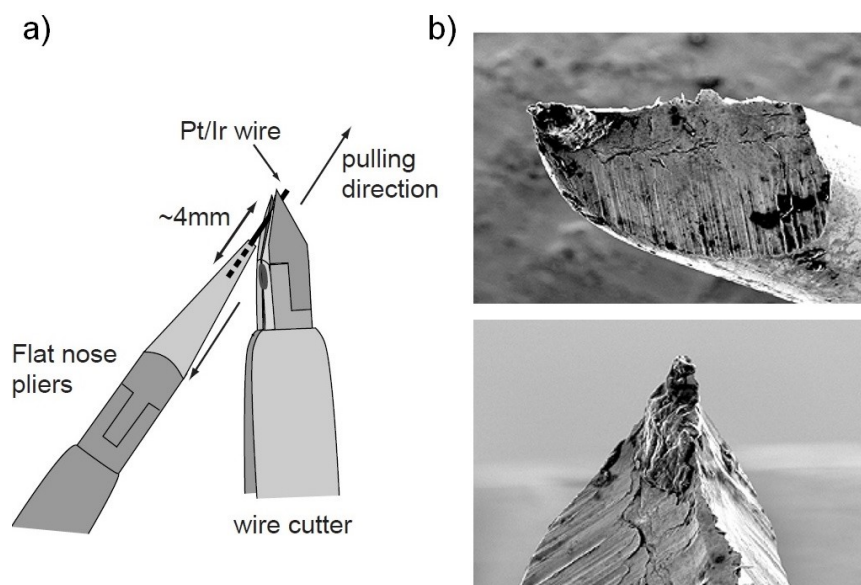


Figure 4.10: (a) Schematic of Pt/Ir-tip preparation by mechanical cutting (b) micrographs of the tip after preparation. Taken from [97].

4.2.3 Iron coated tungsten (Fe/W) tips

Iron coated tungsten tips are one of the most sophisticated tips for STM. They belong to a family of nonmagnetic tips covered with an ultrathin film of magnetic material. The most common nonmagnetic tip is the well-known W-tip, where magnetic films mostly based on iron or chromium are further deposited. This configuration permits the construction of an STM-tip that is sensitive to the spin of the electrons involved in the tunneling process. A great advantage with respect to e.g. bulk magnetic Fe-tips is the low stray fields emanated from the sharp tip end. Furthermore, the preparation of this tip configuration allows for the tuning of the tip magnetic properties (e.g. easy axis of magnetization) by changing the magnetic material and the film thickness on the W-tip [29].

The preparation of iron coated tungsten tips is non-trivial and requires costly equipment which operates at UHV conditions. The first step is the preparation of the W-tip, which has already been described in section 4.2.1. Once a free oxide W-tip is prepared, its tip surface will be ready to host an ultrathin film of iron (see figure 4.11). After the evaporation of some monolayers, a homogeneous film is obtained. However, a later annealing process helps in avoiding the presence of clusters that could interfere with the SP-STM measurements.

The quantity of evaporated iron, in principle, determines the polarization direction of the magnetic tip. The competence between the tip shape anisotropy and the anisotropy of the iron film determine the direction of the final magnetization. It has been indicated in previous works that iron coated tungsten tips exhibit in-plane polarization most of the time, if the number of evaporated monolayers is between 3 and 10. However, it is well-known that the structure of the last cluster could be diverse and therefore responsible for several other polarization directions (e.g. out-of-plane, or in between out-of-plane and in-plane) [61].

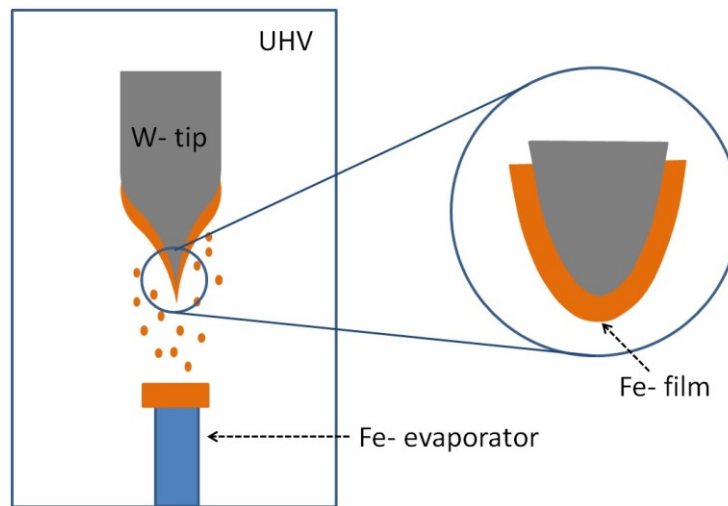


Figure 4.11: Schematic of a W-tip being covered by an iron thin film in UHV conditions.

4.2.4 Chromium (Cr) tips

Chromium bulk tips are good candidates for SP-STM measurements due to the fact that no UHV conditions are required for their preparation. Furthermore, they present negligible magnetic stray fields. Cr-tips can achieve atomic resolution with relative ease [99]. In terms of tip preparation, Cr-tips can be made from polycrystalline rods by electrochemical etching [72]. The etching process can be performed by using electrolytes such as NaOH or KOH (1.5 – 2M) in distilled water by working with voltages between 3 to 5V (see references for more details). During the etching process, different chemical remnants of Na/K and Cr stick onto the rod-surface, but they are soluble in water and can be completely removed by using a water ultrasonic bath. Once a Cr-tip is chemically prepared, additional cleaning procedures such as argon-ion sputtering (in UHV) and tip treating with voltage pulses (up to 10V) on a metal substrate may be required. Previous works have shown Cr-bulk-tips having in-plane magnetic anisotropy in the absence of an external magnetic field. However, this magnetization direction could be changed to out-

of-plane with the help of an external magnetic field of 2 T. In other cases, a canted magnetization direction has been shown to allow them to be sensitive to both in-plane and out-of-plane magnetic components, see figure 4.12 [100,101].

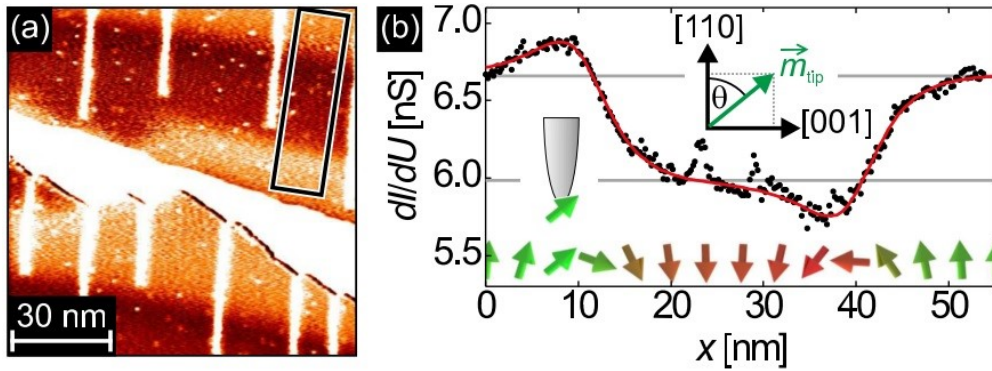


Figure 4.12: (a) Magnetic map over 2ML-Fe nanostructures, (b) line section (black data points) across two double layer walls, averaged over the regions of interest indicated in (a). Taken from [100].

5 Dinickel molecular complexes on Au(111)

5.1 Motivation

Organic magnetic materials are nowadays intensively investigated due to their potential in the development of a new generation of devices based on electron spin currents. This is grounded on two aspects: i) organic molecules can have the capability to build up circuits from a bottom-up approach, reaching smaller sizes than the actual electronic circuits; and ii) organic molecules could preserve spin-coherence over longer times and distances in contrast to conventional metals or semiconductors [102,103]. In this sense, the development of chemical systems which contain magnetically bistable transition metal complexes arranged on planar surfaces could contribute to the architecture of materials with controllable magnetic or spintronic properties [104–107], leading to potential applications on information storage at the molecular level [108,109], in molecular electronics [103], and molecular spintronics [16,102,110,111].

Research lines have been mainly focused on the physisorption or chemisorption of planar organometallic complexes such as phthalocyanines [112–114], porphyrines [115–118], and spin-crossover compounds. Recently, single molecule magnets (SMMs) bearing several coupled transition metal ions have received increasing attention [119,120], and several strategies have been developed to obtain these materials as rows [121], thin films [111,122–124], or multilayers [125–131]. Unfortunately, polynuclear transition metal complexes suffer from limited thermal and kinetic stability, which does not allow their thermal evaporation on surfaces [132]. Therefore, alternative methods have been considered for surface functionalization. Among them all, chemisorption of open-shell transition metal complexes *via* Au-S bonds in the form of self-assembled monolayers (SAM) has turned out to be an attractive and suitable method [133,134].

For the deposition of polynuclear complexes with single molecular magnet (SMM) behaviour two major strategies have been established. The first approach consists of the growth of a SAM of a bifunctional thiol HS-X-L, where X represents a spacer and L usually a carboxylate function, and afterwards the adsorption of a SMM. The second method, which we address here, utilizes an exchange-coupled mixed-ligand complex

with an exposed thiol function¹ that is directly deposited onto the gold surface [120,135–137]. Monolayers produced by adsorption from solution are not restricted to gold and can be applied to other substrates like silicon, silicon oxides, or metal oxides [138,139].

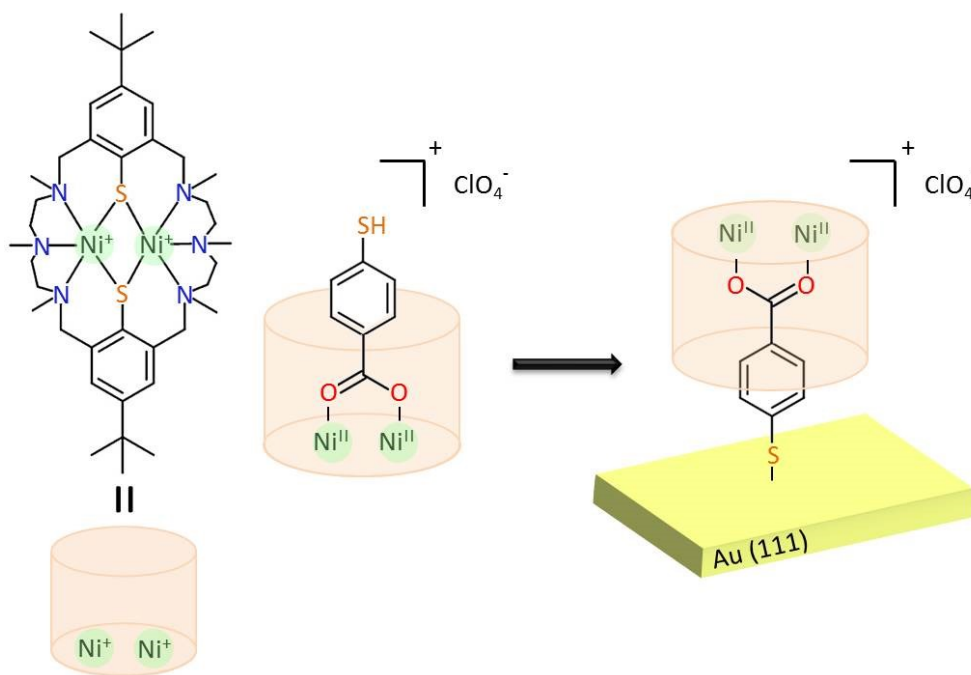


Figure 5.1: Chemisorption of dinickel macrocyclic complexes $[\text{Ni}_2\text{L}(\text{Hmba})]\text{ClO}_4$ (2ClO_4) on Au(111).

The synthesis of the perchlorate salt $[\text{Ni}_2\text{L}(\text{Hmba})]\text{ClO}_4$ (2ClO_4) has been previously reported over [140]. This compound is composed of a paramagnetic dinickel macrocyclic complex ($[\text{Ni}_2\text{L}(\text{Hmba})]^{2+}$) with an $S = 2$ ground state and negative axial anisotropy and a perchlorate ion (ClO_4^-). In the cation, L represents a 24-membered macrocyclic hexaazadithiophenolate ligand and Hmba an ambidentate 4-mercaptopbenzoate ligand ($\text{HO}_2\text{CC}_6\text{H}_4\text{SH}$, H_2mba). The ambidentate ligand has a hard carboxylate function which serves to bind to the Ni^{II} ions in $[\text{Ni}_2\text{L}]^{2+}$ and a soft thiol group for the chemisorption to the gold surface (see Figure 5.1). Here, the evaluation of the molecular anchoring and electrical conductance of these complexes on a Au(111)-surface *via* ambidentate mercaptopbenzoate ligands by using STM and XPS is reported.

¹ The SMM behavior of carboxylate-bridged complexes of the type $[\text{Ni}_2\text{L}(\text{O}_2\text{CR})]^+$ (CR, carbon-radicals) were previously substantiated by HF-EPR measurements. However, the magnetic anisotropy barrier is too small to get sufficient magnetization at finite temperature [177].

We found anchored monolayers *via* Au-S bonds with a height of about 1.5 nm apparently showing a granular structure, with the dinickel complexes appearing as roundish structures and the ClO_4^- counterions as the surrounding environment. No type of long or short range order was observed. Tip-interaction reveals higher degradation rate after eight hours of measurement. Spectroscopy measurements suggest a HOMO-LUMO gap of about 2.5 eV in the dinickel complexes and smaller gap in the surrounding environment.

5.2 Synthesis of molecular complexes

The dinickel molecular complexes used in this thesis were synthesized by Prof. Kersting's group at the University of Leipzig. As reported by J. Lach *et. al.* [140], the synthesis of the molecular complex $[\text{Ni}_2\text{L}(\text{Hmba})]^+$ is achieved through the complexation of the ambidentate ligand ($\text{HO}_2\text{CC}_6\text{H}_4\text{SH}$, H_2mba) by the macrocyclic complex $[\text{Ni}_2\text{L}(\mu\text{-Cl})]\text{ClO}_4$ ($\mathbf{1ClO}_4$). The mono-deprotonated Hmba^- ligand reacts with the Ni_2 complex in a selective manner by substituting the bridging chloride ligand to produce the $\mu_{1,3}$ -carboxylato bridged complex $[\text{Ni}_2\text{L}(\text{Hmba})]^+$. Experimentally, such a reaction was described as the treatment of $[\text{Ni}_2\text{L}(\mu\text{-Cl})]\text{ClO}_4$ ($\mathbf{1ClO}_4$) with 4-mercaptobenzoic acid (H_2mba) in the presence of triethylamine (NEt_3) and lithium perchlorate (LiClO_4), finally obtaining a green solution containing the targeted product $[\text{Ni}_2\text{L}(\text{Hmba})]^+$ in the form of a microcrystalline perchlorate salt $[\text{Ni}_2\text{L}(\text{Hmba})]\text{ClO}_4$ ($\mathbf{2ClO}_4$). The goal-product was obtained with yields of 88 % (see figure 5.2).

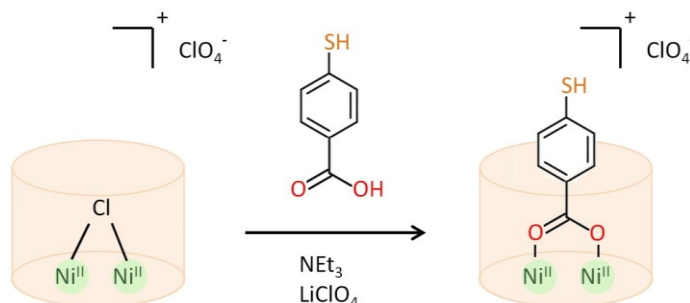


Figure 5.2: Synthesis of the perchlorate salt $[\text{Ni}_2\text{L}(\text{Hmba})]\text{ClO}_4$ ($\mathbf{2ClO}_4$).

The new mercaptobenzoate complex reacts through the free thiophenolate ligand. Therefore, in the presence of air, $\mathbf{2ClO}_4$ dimerizes via a disulfide bond to generate the tetranuclear complex $[\{\text{Ni}_2\text{L}\}_2(\text{O}_2\text{CC}_6\text{H}_4\text{S})_2]^{2+}$ (see figure 5.3 (a)). Moreover, the auration of $\mathbf{2ClO}_4$ with $[\text{AuCl}(\text{PPh}_3)]$, where PPh_3 stands for triphenylphosphine, produces the monoaurated complex $[\text{Ni}_2^{\text{II}}\text{L}(\text{mba})\text{Au}^{\text{I}}\text{PPh}_3]$ ($\mathbf{4ClO}_4$). The latter was an important hint in order to prove the capability of the $\mathbf{2ClO}_4$ complexes to be anchored to gold surfaces (see figure 5.3 (b)).

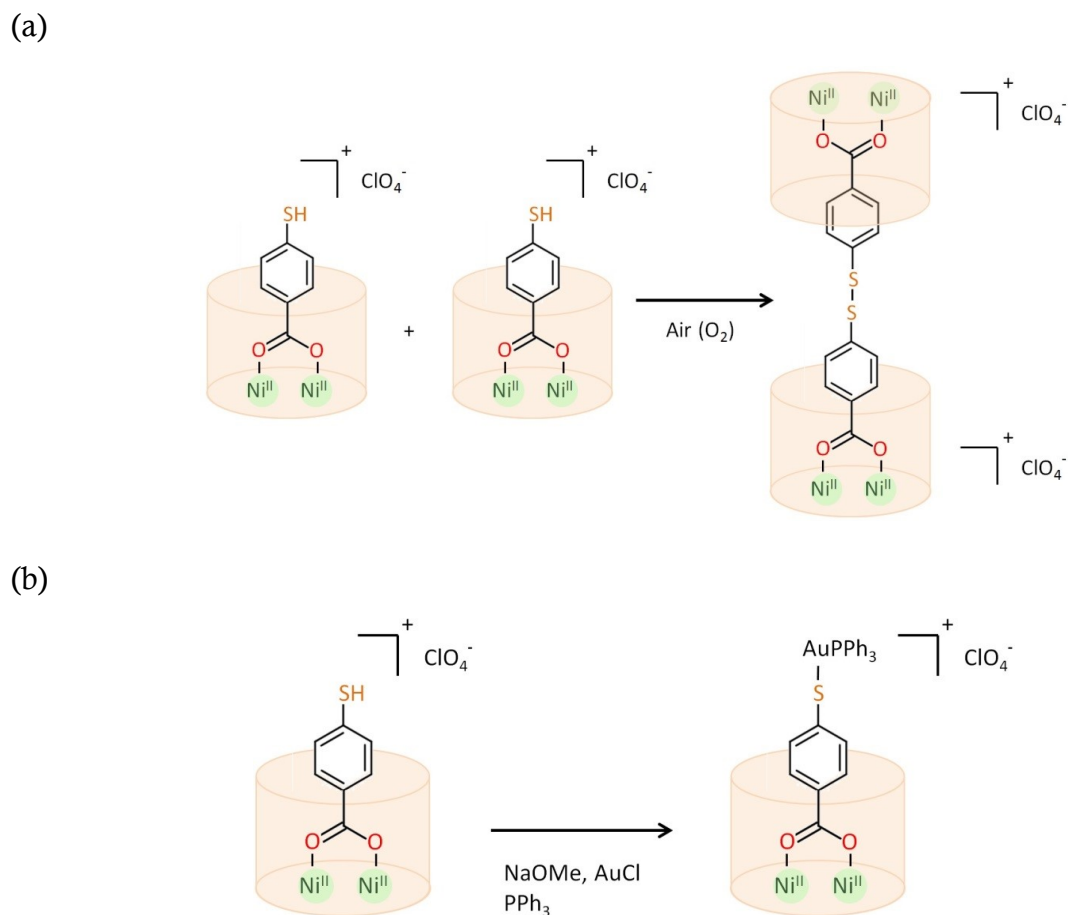


Figure 5.3: Reactions of the perchlorate salt $[\text{Ni}_2\text{L}(\text{Hmba})]\text{ClO}_4$ (2ClO_4): (a) dimerization, (b) auration (4ClO_4).

5.3 Characterization

5.3.1 Electrochemistry

Cyclic voltammograms (CV) are of great value to determine the redox properties of ionic compounds. J. Lach *et.al.* [140] reported CV curves of the compound 2ClO_4 in comparison to similar compounds, such as 4ClO_4 and $[\text{Ni}_2\text{L}(\text{OAc})]\text{ClO}_4$ (see figure 5.4). The CV of 2ClO_4 exhibits two main peaks at 0.66 V and 1.45 V, which suggests two redox processes assigned as metal-centered ($\text{Ni}^{\text{II}}\text{Ni}^{\text{II}} \rightarrow \text{Ni}^{\text{III}}\text{Ni}^{\text{II}}$) and ligand based [$\text{RS}(\text{thiolate}) \rightarrow \text{RS}(\text{thiyl radical})$] oxidation within the $[\text{Ni}^{\text{II}}_2\text{L}]^{2+}$ (figure 5.4 up). Similar peaks have been observed for the related compounds 4ClO_4 and $[\text{Ni}_2\text{L}(\text{OAc})]\text{ClO}_4$, as shown in figure 5.4 middle and bottom, respectively [141]. The CV of 2ClO_4 shows additional features which are not so well defined in the cathodic potential regime, with peaks approximately at -1.6 V and -1.0 V. These features can be possibly attributed to the redox process of the 4-mercaptobenzoate ligand. However, it was suggested that these

values should be taken as indicative rather than definitive, considering that the determination of the RS⁻/RSSR couple could have been hampered due to the chemisorption of thiolate ligands to the electrode materials.

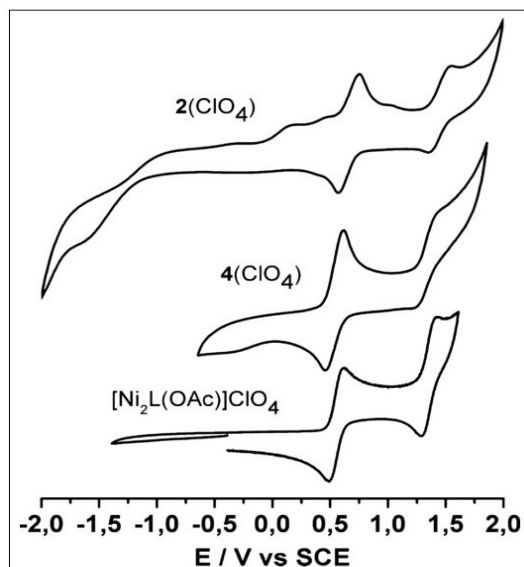


Figure 5.4: Cyclic voltammogram of the perchlorate salt $[\text{Ni}_2\text{L}(\text{Hmba})]\text{ClO}_4$ (2ClO_4) and its comparison with the compounds $4(\text{ClO}_4)$ and $[\text{Ni}_2\text{L}(\text{OAc})]\text{ClO}_4$. Graphic taken from reference [140].

5.3.2 Magnetic properties

Previous studies of magnetic properties carried out by J. Lach *et.al.* [140], showed the magnetic susceptibility versus temperature (figure 5.5 (a)) and magnetization versus external magnetic field (figure 5.4 (b)) of the dinickel molecular complexes under investigation. Additionally, they are compared with the related aureate molecular complexes 4ClO_4 . The results plotted in figure 5.5 (a) show the data corresponding to powdered solid samples in the temperature range of between 2 and 330 K in the presence of an external magnetic field of 0.5 T. For 2ClO_4 , the value of magnetic susceptibility increases from $2.79 \text{ cm}^3 \text{ K mol}^{-1}$ ($4.73 \mu_B$) at 330 K to a maximum of $3.55 \text{ cm}^3 \text{ K mol}^{-1}$ ($5.33 \mu_B$) at 20 K and then it decreases to $2.95 \text{ cm}^3 \text{ K mol}^{-1}$ ($4.86 \mu_B$) at 2 K. Looking at figure 5.5 (a), one can recognize similar behaviour from the compound 4ClO_4 (data almost overlap each other). The decrease in magnetic susceptibility below 20 K was attributed to zero-field splitting of Ni^{II} . The magnetic susceptibility behaviour revealed in both cases an intramolecular ferromagnetic exchange interaction between two Ni^{II} ions, leading to an $S = 2$ ground state. The data also showed that auration does not significantly influence the electronic structure of the $[\text{Ni}_2\text{L}(\text{mba})]^{2+}$ complex fragment.

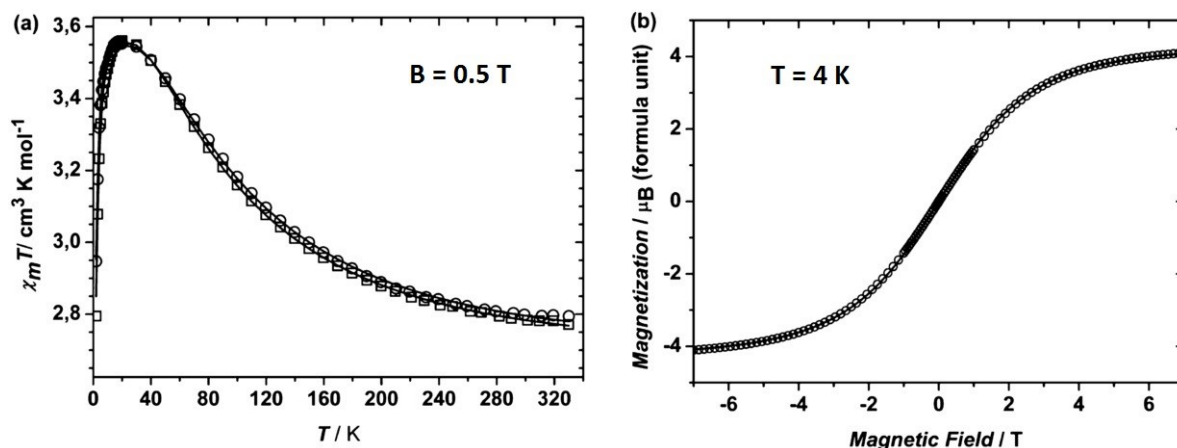


Figure 5.5: (a) Magnetic susceptibility multiplied by temperature (T) (per dinuclear complex) versus temperature (T) for 2ClO_4 (open circles) and 4ClO_4 (open squares) (data of 2ClO_4 and 4ClO_4 almost overlap each other). The full lines represent the best theoretical fit to equation (5.1). (b) Magnetization versus magnetic field measured at $T = 4$ K for 2ClO_4 (open circles). The full line represents the best theoretical fit to equation (5.2). Graphics taken from reference [140].

The fitted data of 2ClO_4 and 4ClO_4 using the Hamiltonian in equation (5.1) provided values for J = coupling constant, g = g value, D = zero-field splitting parameter, and TIP = temperature independent paramagnetism, which are all listed below in table 5.1.

$$H = -2J\hat{S}_1\hat{S}_2 + \sum_{i=1}^2 \left\{ D_i \left[\hat{S}_{zi}^2 - \frac{1}{3}\hat{S}_i(\hat{S}_i + 1) \right] + g_i\mu_B S_{i\tau} B_\tau \right\} \quad (\tau = x, y, z) \quad (5.1)$$

Compound	g	$J(\text{cm}^{-1})$	$D(\text{cm}^{-1})$	TIP ($\text{cm}^3 \text{mol}^{-1}$)
2ClO_4	2.18	22.29	5.23	3.59×10^{-4}
4ClO_4	2.18	20.83	6.73	3.33×10^{-4}

Table 5.1: Parameters g , J , D , and TIP from the fit of the equation 4.1. Values taken from reference [140].

Magnetization versus magnetic field was measured in 2ClO_4 at 4 K between -7 and +7 T (figure 5.5 (b)). In figure 5.5 (b) are shown the experimental data (open circles) and the theoretical fit (full line) in complete agreement (practically overlapped). The theoretical fit was carried out by employing the Brillouin function (equation 5.2) confirming an $S = 2$ ground state for the 2ClO_4 .

$$M(H) = N_A g \mu_B \left[\frac{2S+1}{2S} \coth \left(\frac{g\mu_B H}{kT} \frac{2S+1}{2S} \right) - \frac{1}{2S} \coth \left(\frac{g\mu_B H}{kT} \frac{1}{2S} \right) \right] \quad (5.2)$$

5.4 Chemisorption on gold surfaces: first hints

5.4.1 Contact angle measurements

As was described by Thomas Young [142], the contact angle of a liquid drop on an ideal solid surface (see figure 5.6) is defined by the mechanical equilibrium of the drop under the action of the solid-gas, solid-liquid and liquid-gas interfacial tensions (γ_{SG} , γ_{SL} , γ_{LG}):

$$\gamma_{SG} - \gamma_{SL} - \gamma_{LG} \cos \theta_c = 0, \quad (5.3)$$

where θ_c represents the contact angle. The angle, which reflects the surface wettability, is conventionally measured through the liquid.

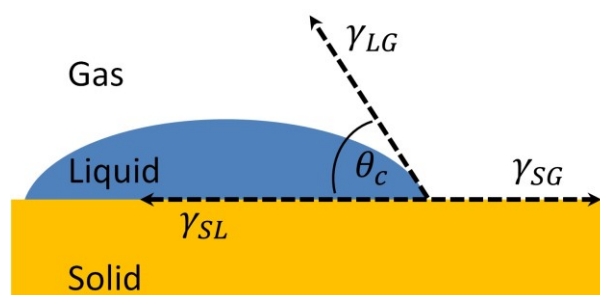


Figure 5.6: Contact angle measurements. The equilibrium contact angle reflects the relative strength of the liquid, solid, and vapor molecular interaction.

A comparative experiment of the wettability of gold functionalized surfaces (with 2ClO_4 and H_2mba) by J. Lach *et.al.* [140], provided the first hint to consider, in the surface anchoring of 2ClO_4 complexes. The surface wettability was evaluated through static water-contact-angle measurements, as shown in table 5.2.

Compound	Contact angle (°)	Standard deviation
Bare gold (EtOH)	75.8	1.5
H_2mba	55.6	1.7
2ClO_4	71.4	2.1

Table 5.2: Water (static)-contact-angle measurements. The values represent the average of 10 measurements by using 4 μL drops of deionized water. Values taken from reference [140].

The highest contact angle value of 75.8° was exhibited for the non-polar gold surface (in good agreement with literature [143]), being less hydrophilic than the monolayers of 2ClO_4 and H_2mba (having contact angles of 71.4° and 55.6° , respectively). The most

hydrophilic surface was the monolayer of H₂mbs due to the presence of polar surface carboxylate functions [144]. The monolayer formed with 2ClO₄ showed a lower contact angle in comparison to the bare gold surface. This indicated the transition to a more polar surface after the chemisorption of 2ClO₄. However, it is worth to notice that 2ClO₄ is not as polar as the H₂mbs-monolayer, indicating a good shielding of the charge by the non-polar groups from the macrocyclic ligands.

5.4.2 XPS studies

X-ray photoelectron spectroscopy (XPS) is a surface-sensitive spectroscopic technique that is useful to investigate the chemical and electronic properties of surfaces and interfaces (see the basics in figure 5.7). A XPS spectrum is obtained by irradiating a material with X-rays, while simultaneously, the kinetic energy and number of electrons that escape from the surface sample are measured (see photoelectric effect in [42]).

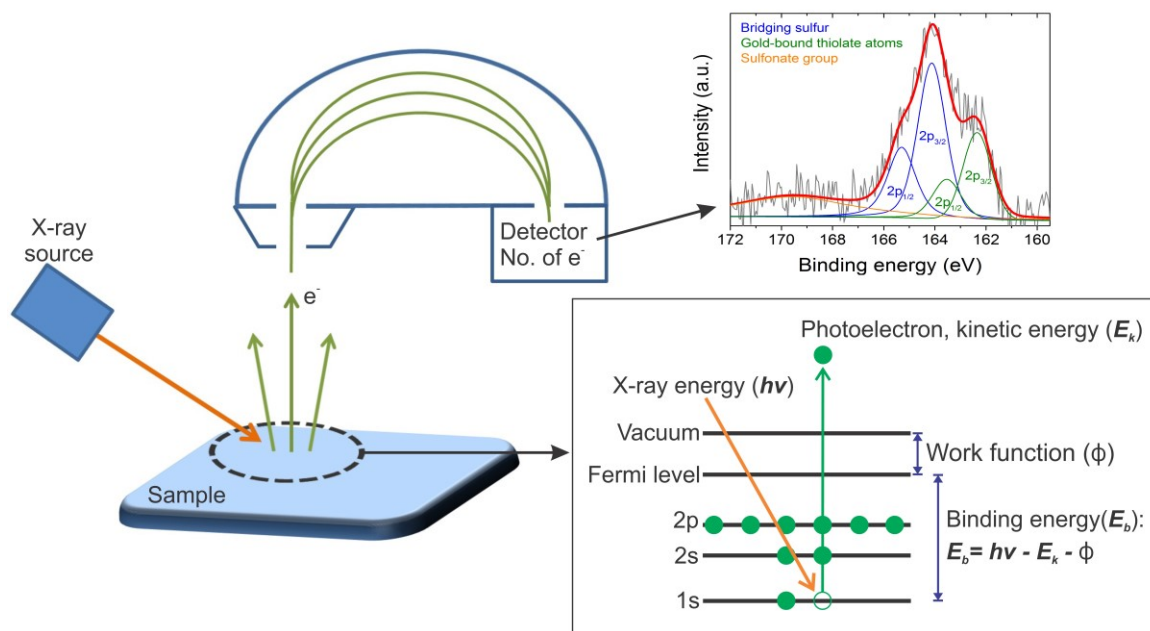


Figure 5.7: X-ray photoelectron spectroscopy technique (XPS).

The XPS spectrum is a plot of the number of detected electrons (Intensity (a.u.)) versus the binding energy (E_b (eV)), which is obtained as is indicated in equation 5.4. $h\nu$ is the X-ray photon energy, E_k is the photoelectron kinetic energy and ϕ is the work function of the sample.

$$E_b = h\nu - E_k - \phi \quad (5.4)$$

The elements on the sample surface can be identified and chemically analyzed by producing a characteristic set of XPS peaks at characteristic binding energies. These

characteristic spectral peaks correspond to the electronic configuration within the sample atoms, e.g. 1s, 2s, 2p, 3s, etc. The number of detected electrons in each of the characteristic peaks is directly related to the amount of an element with a specific electronic configuration within the XPS sampling volume.

Element	2ClO ₄	2ClO ₄ on Au(111)	Assignment
S(2p _{3/2})	169.2	168.7	RSO ₃ ⁻
	163.0	163.6	Nickel-bound sulfur atoms
	164.3		Free thiol
		161.9	Gold-bound 4-mercaptobenzoate
S(2p _{1/2})	170.2	169.7	RSO ₃ ⁻
	164.1	164.6	Nickel-bound sulfur atoms
	165.3		Free thiol
		162.8	Gold-bound 4-mercaptobenzoate
Ni(2p _{3/2})	856.3	855.0	Ni ²⁺
	863.0	862.5	“shake up satellite”
C(1s)	286.1	285.2	Aliphatic and aromatic carbon atoms
	287.5	286.6	Sulfur-bound carbon atoms
	289.5	288.6	RCO ₂ ⁻
Cl(2p _{3/2})	208.8	209.0	ClO ₄ ⁻
Cl(2p _{1/2})	210.4	210.6	
Cl(2p _{3/2})	199.5	199.0	Cl ⁻
Cl(2p _{1/2})	201.1	200.6	

Table 5.3: XPS binding energies (eV) for 2ClO₄ and SAM of 2ClO₄ on gold. The binding energies are referenced to Au(4f_{7/2}) (84.0 eV). Values taken from reference [140].

A special characteristic in XPS spectra of paramagnetic states are the “shake up” peaks. They appear when an outgoing photoelectron leaves the ion in a specific excited energy state a few eV above the ground state. Thus, the kinetic energy of the emitted

photoelectron is therefore reduced and this will result in a satellite peak at higher binding energy than the main line [145].

The chemisorption of 2ClO_4 was previously investigated by J. Lach *et al.* [140], by X-ray photoelectron spectroscopy [140]. The main results (peak positions and their assignments) are listed in table 5.3. In particular, the XPS peaks for the powder and for the deposited 2ClO_4 in the S(2p) region clearly reveal covalent bonding of the $[\text{Ni}_2\text{L}(\text{Hmba})]^+$ complexes to the gold surface *via* Au-S single bonds.

The analysis in the Ni($2p_{3/2}$) regions showed the signal corresponding to the Ni and also the well-known shake up satellites at 863 and 862 eV characteristic for divalent, six-coordinate nickel complexes. These results indicated that complex 2ClO_4 undergoes no redox changes upon surface fixation.

5.5 Results: Monolayers of the complex $[\text{Ni}_2\text{L}(\text{Hmba})]\text{ClO}_4$ on Au(111)

5.5.1 Sample preparation

Preparation of the substrate: In order to study the anchoring of $[\text{Ni}_2\text{L}(\text{Hmba})]\text{ClO}_4$ on gold surfaces in detail, Au(111) single crystals were prepared as indicated in chapter 4. A posterior STM topographic constant-current measurement revealed for the crystal used in the STM experiments at room temperature a typical Au(111) surface reconstruction with atomic steps shown in Figure 5.10 (a). The crystal used in the STM experiments at low temperature additionally showed the well-known herringbone surface reconstruction shown in chapter 4.

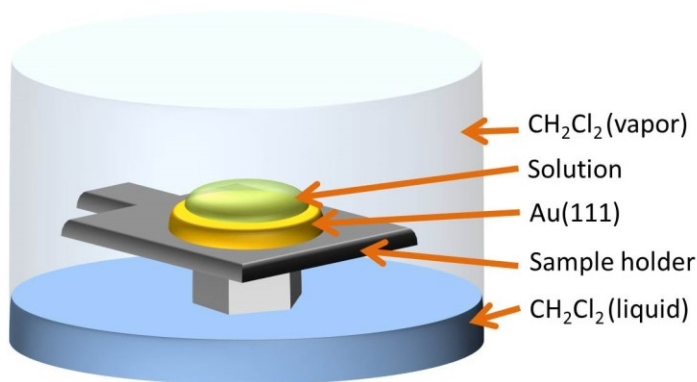


Figure 5.8: Schematic of the experimental set-up for the deposition of dinickel molecular complexes from a solution of $[\text{Ni}_2\text{L}(\text{Hmba})]\text{ClO}_4$ in dichloromethane (CH_2Cl_2).

Preparation of monolayers: A few drops of a 1.4 mM solution of 2ClO_4 [140] in dichloromethane were deposited on the gold single crystal until the surface was fully covered. The sample was then stored at room temperature within a dichloromethane atmosphere for 15 hours (see schematic of the set-up in figure 5.8). This set-up assured

the selective contact of the 2ClO_4 solution with only the gold crystal, avoiding possible contaminations from the sample holder made of tungsten. The liquid dichloromethane in the set-up contributed to form a saturated atmosphere of evaporated dichloromethane preventing a quick evaporation of the 2ClO_4 solution as well as contamination through contact with air. Finally, the substrate was washed with dichloromethane and ethanol, dried under vacuum, and transferred to the STM or XPS. Prior to the measurements, the sample was subjected to an annealing process at 70°C for 3 hours in order to exclude the presence of organic solvents on the sample.

5.5.2 Monolayer characterization *via* core level spectroscopy (XPS)

Experimental details: X-ray (XPS) photoemission spectroscopy experiments were carried out using a two-chamber ultra-high vacuum system. The measurement chamber with a base pressure of about 2×10^{-10} mbar is equipped with an electron-energy analyzer PHOIBOS-150 purchased from SPECS and an x-ray tube providing monochromatic Al K α radiation with a photon energy of 1486.6 eV. The total energy resolution of the spectrometer was 0.35 eV. More detailed information concerning photoemission spectroscopy can be found in reference [146].

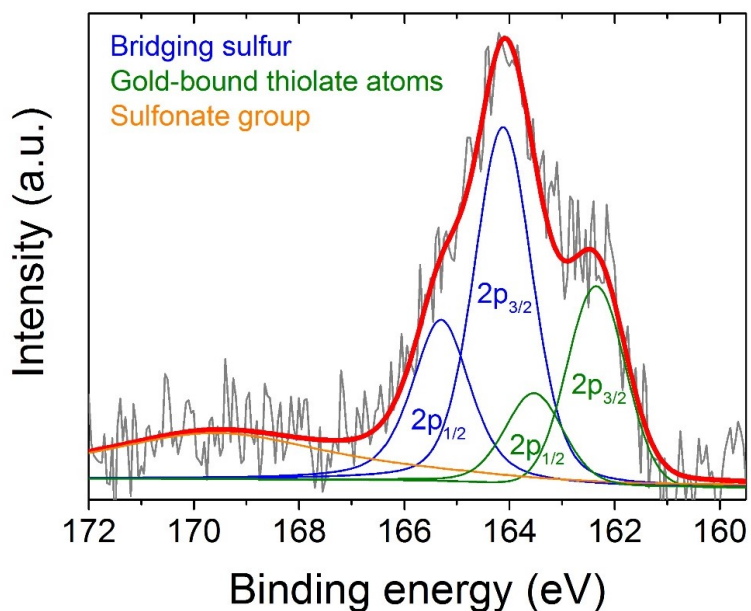


Figure 5.9: XPS S 2p core level data for a monolayer of $[\text{Ni}_2\text{L}(\text{Hmba})]\text{ClO}_4$ chemisorbed on Au(111). The experimental spectrum (grey) could be fitted (red) by the use of the contributions of sulfonate groups (orange), gold-bound thiolate (green) and bridging sulfur functions (blue). Spectrum measured and analyzed by Florian Ruckerl.

Chemisorption of the monolayer: Figure 5.9 depicts the obtained spectrum for the sulfur (S) 2p core level. The main photoemission feature is located in the region between 161 eV

and 167 eV photon energy. A second broad feature can be found around 170 eV. The data could be fitted very well by using three different contributions. The broad feature at higher energies can be assigned to a sulfonate group (RSO_3^-) which stems from an X-ray-induced decomposition of the ClO_4^- [140,147]. Note, that there is only minor decomposition due to a preferably short measurement time, which resulted in a lower sulfonate percentage compared to former studies [140].

The main feature can be divided into two spin-orbit split contributions [148]. One at 165.3 eV and 164.1 eV and the other at 163.4 eV and 162.6 eV binding energy. The ratio between both contributions was found to be 2:1. On the spectroscopic point of view, the feature at lower binding energy distinguishes itself by a higher electron density and a resulting different screening in comparison to the feature at higher energies. The ratio of 2:1 gives an additional hint on the bonding situation of the sulfur atoms in $[\text{Ni}_2\text{L}(\text{Hmba})]\text{ClO}_4$. According to the literature, the first contribution at higher binding energies can be addressed to the bridging sulfur functions while the other at lower energies to the gold-bound thiolate group [140,149–151], whereby two out of three sulfur atoms of the compound are bridged while the remaining one is bonded to the gold substrate. We note that the shape of the Ni $2p_{3/2}$ core level (not shown) with its well-known shake up satellites is characteristic of divalent, six-coordinate nickel complexes and hence implies that there are no redox state changes upon surface fixation [140]. Thus, the XPS data confirm the bonding of the molecules to the gold surface.

5.5.3 Monolayer characterization *via* scanning tunneling microscopy (STM)

Experimental details: The measurements at room temperature were carried out in the LT-STM, whereas the measurements at low temperature (70 K) were conducted in the Omicron variable temperature STM (both STMs are described in chapter 3). Regarding tip preparation, Pt/Ir wires were mechanically prepared in a standard manner as described in chapter 4. Topographic images were acquired in the constant current mode and the single point $I(U)$ curves were measured with an open feedback loop at the given stabilization parameters (see chapter 2). The spectroscopy curves were averaged out of thirty measurements.

Monolayer characterization at room temperature: Figure 5.10 (a) shows a representative topographic constant-current image of the Au(111) surface of the substrate single crystal prior to the molecular deposition. Figures 5.10 (b) and (c) show typical topographic results obtained after *ex-situ* deposition of 2ClO_4 . The two panels represent the bias-selective backward and forward images of the same surface area, simultaneously obtained. The topographic data shown in figure 5.10 (b) was obtained with $U_{\text{bias}} = 1$ V during the backward-moving direction of the tip and figure 5.10 (c) with $U_{\text{bias}} = 2.5$ V during the forward-moving direction of the tip. The former seems to be less sensitive to

the molecular electronic states than the latter, as in figure 5.10 (b) the contrast which apparently predominantly arises from the steps of the underlying Au(111) surface (apart from a relatively low number of much brighter and much darker objects), whereas in figure 5.10 (c) the contrast mainly arises from a compact arrangement of roundish structures where the Au(111) surface steps appear less clear.

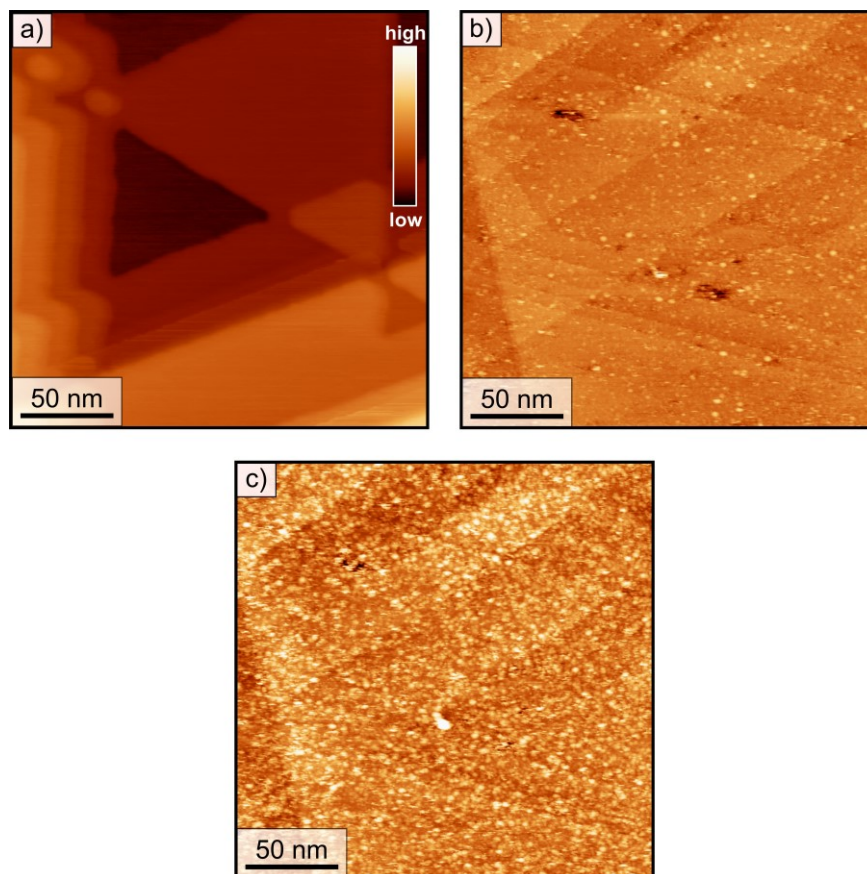


Figure 5.10: (a) Topographic image of a clean Au(111) surface of the substrate single crystal prior to the molecular deposition ($I = 15$ pA, $U_{bias} = -25$ mV $T = RT$). (b) Backward topographic image after the 2ClO_4 deposition acquired with $U_{bias} = 1$ V, $I = 10$ pA, and $T = RT$. (c) Forward topographic image after the 2ClO_4 deposition acquired with $U_{bias} = 2.5$ V, $I = 10$ pA, and $T = RT$.

This result makes evidence the presence of a monolayer on the surface of a gold crystal which is, however, detected only at relatively high bias voltages. This suggests discrete electronic states in the molecular structures and located relatively far away from the Fermi energy in contrast to the continuous electronic states presented in bulk materials. Therefore, the bias voltage of 1 V achieves the electronic tunneling current by mainly involving occupied states of the tip and unoccupied states of the gold.

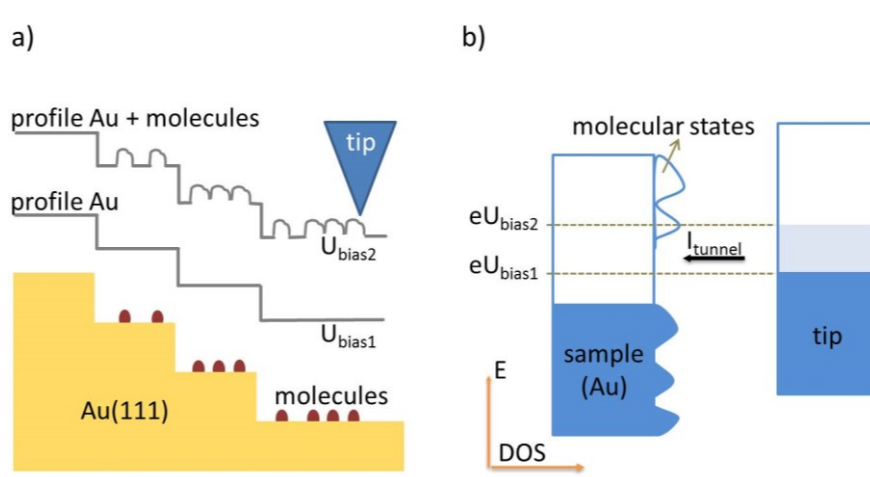


Figure 5.11: (a) Schematic of the topographic line profiles taken at different bias voltages. (b) Interpretation of the tunneling process involving the electronic density of states of the monolayers and/or the metallic substrate.

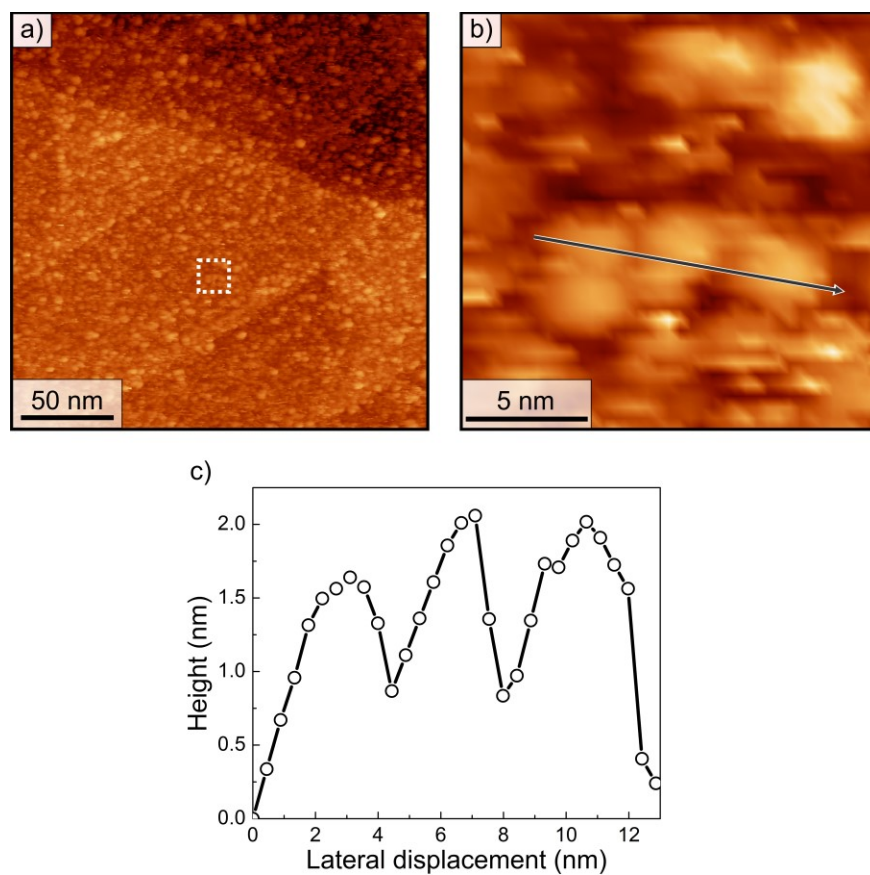


Figure 5.12: (a) Constant-current topographic image after 2ClO_4 deposition ($I = 10$ pA, $U_{bias} = 2.5$ V, $T = \text{RT}$). (b) digital zoom-in of square area (dashed white line) in (a). (c) line profile along arrow in (b).

However, in the case of 2.5 V the tunneling current is established between the occupied states of the tip and unoccupied states of the monolayer (see figure 5.11).

Looking at different areas of the sample, one can determine that the monolayer covers a large surface of the gold crystal (figure 5.12 (a) is another example of the surface topography). Figure 5.12 (b) shows a digital zoom-in of the marked area (dashed white line) in Figure 5.12 (a), and Figure 5.12 (c) depicts a line profile along the arrow in Figure 5.12 (b). As can be seen in these data, the characteristic minimum distance between two neighboring roundish bright structures is between 3 - 4 nm with a typical height of about 1.5 - 2.0 nm. Evidence of long range and short range order of these structures as checked by investigating both the Fourier transformed and autocorrelated data. However, no such evidence was observed.

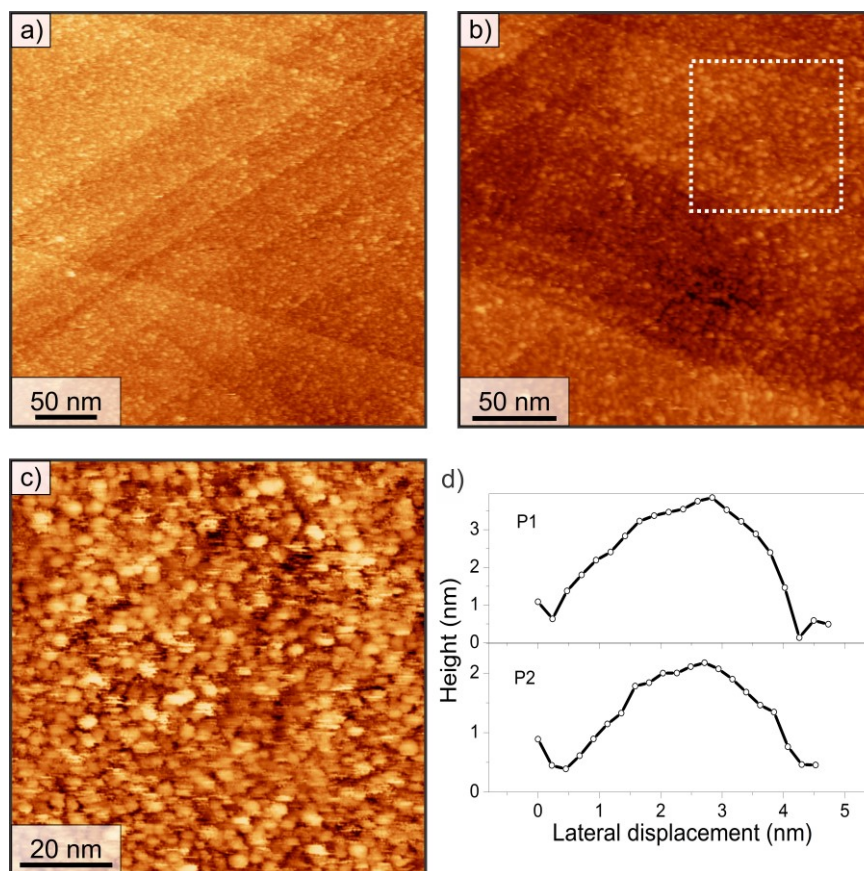


Figure 5.13: (a), (b) Topographic images in different areas after 2ClO_4 deposition ($I = 10$ pA, $U_{bias} = 2.5$ V, $T = \text{RT}$). (c) zoom-in of square area (dashed white line) in (b). (d) line profiles along arrows in (c) (P1 and P2).

Although large areas of the monolayers were relatively easy to observe (see more examples in figures 5.13 (a) and (b)), the zoom-in process in order to achieve sub-molecular resolution of the molecular complexes did not work so well. The closest view

of the monolayer is depicted in figures 5.13 (c) and (d). The main reason seems to be the low stability of the system (dinickel complexes), referring to the molecular movement (rotation, vibration) induced by the STM-tip interaction through the bias voltage or tunneling current.

One of the discernable facts of long term measurements is the degradation of the monolayer, promoted by the STM-tip interaction. Figures 5.14 (a), (b), and (c) are topographic images taken approximately at the same spot but at different times. Whereas figure 5.14 (a) shows an almost completed layer, in figure 5.14 (b), some holes in the monolayer start to be evident (see line profile in figure 5.14 (d) taken in (b)), and after around 8 measurement hours the monolayer has suffered considerable degradation as is visible in figure 5.12 (c).

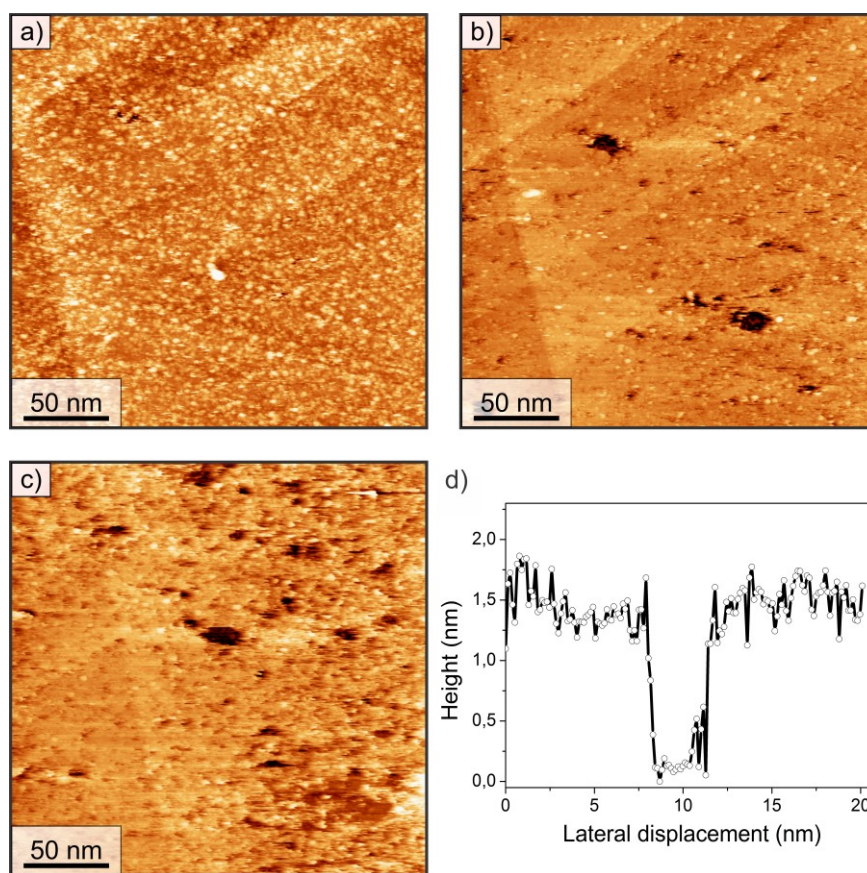


Figure 5.14: (a) Constant-current topographic image after 2ClO_4 deposition ($I = 10$ pA, $U_{\text{bias}} = 2.5$ V, $T = \text{RT}$). (b) topographic image after approximately 3 hours ($I = 10$ pA, $U_{\text{bias}} = 1$ V, $T = \text{RT}$). (c) topographic image after more than 8 hours ($I = 10$ pA, $U_{\text{bias}} = 1$ V, $T = \text{RT}$) (d) line profile along white arrow in (b).

Monolayer characterization at low temperature: Figure 5.15 (a) shows a topographic image of a sample with a roughness of 1.958 ± 0.002 nm. $I(U)$ curves taken at different positions of the surface in figure 5.15 (a) result in an average curve shown in figure 5.15 (b). Such an averaged-curve indicates an insulating sample with a gap that is larger than 3 eV. Interestingly, after six measurement hours we could observe in figure 5.16 (a) that the surface in 5.15 (a) modified its appearance, reducing its roughness to 1.933 ± 0.002 nm. Furthermore, some fissures on the surface began to appear. After 18 measurement hours, in figure 5.16 (b), it was possible to clearly see dark tracks corresponding to the gold surface and other bright tracks corresponding to the remaining monolayer.

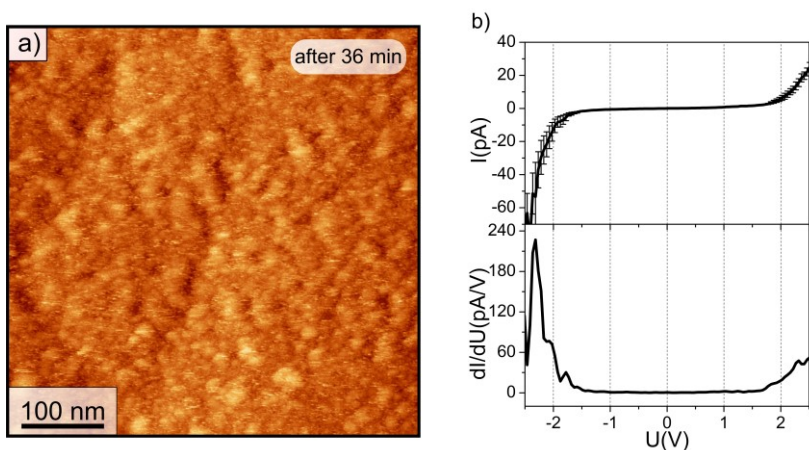


Figure 5.15: (a) Topographic constant-current image of complex 2ClO_4 on Au(111) after 36 min ($I = 30$ pA, $U_{\text{bias}} = 2$ V, $T = 70$ K), (b) characteristic $I(U)$ and dI/dU spectra in (a) (stabilization conditions: $I = 30$ pA, $U_{\text{bias}} = 2.5$ V, $T = 70$ K).

A line profile taken along the dark-arrow in figure 5.16 (b) probes a height of approximately 1.5 nm shown in figure 5.16 (c). Figure 5.17 (a) is a broad topographic image ($1.2 \mu\text{m} \times 1.2 \mu\text{m}$) taken at a different spot of the monolayer following similar measurements that were described in figures 5.15 and 5.16. In figure 5.17 (b) the color scale was changed in order to see different zones clearly, before and after tip-interaction. Zone 1 corresponds to the area where the tip was approached. In zone 1 the tip scanned for approximately one hour. After that, the scan area was changed to zone 2 (dashed black line, $500 \text{ nm} \times 500 \text{ nm}$), where similar measurements were conducted as described for figures 5.15 and 5.16, for approximately the same time (18 hours). The dark blue lines within zone 2 correspond to the gold surface and the red features at its rim correspond to removed parts during scanning from the monolayer. Zones 3 and 4 are areas where no previous measurements were carried out, where zone 4 represents the monolayer in a higher step of the gold crystal.

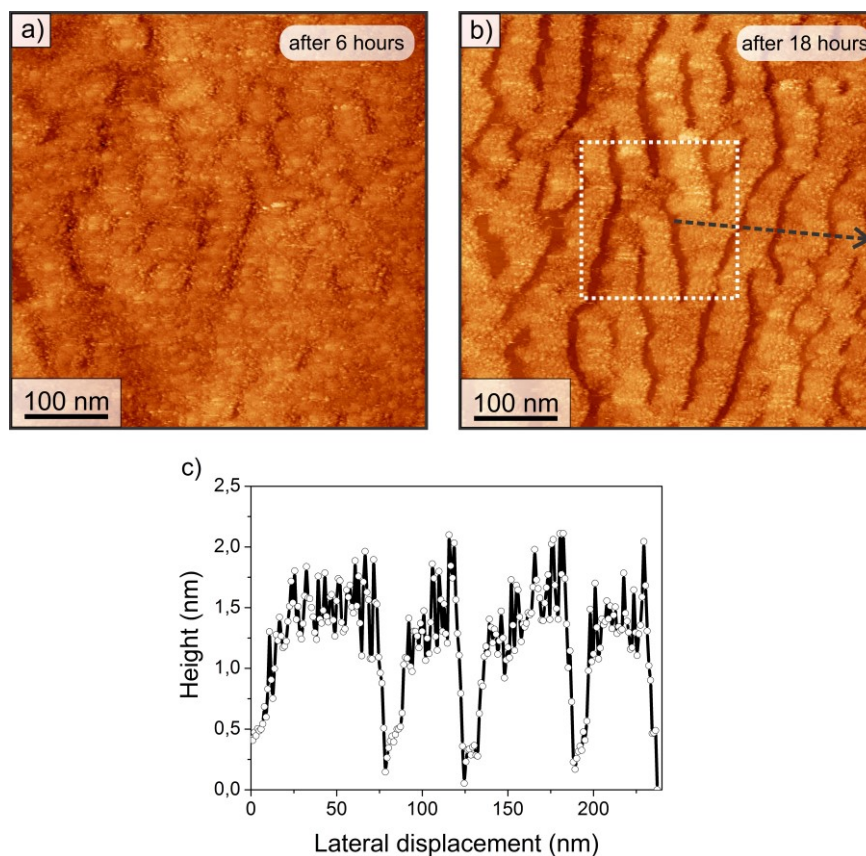


Figure 5.16: (a) Topographic constant-current image of complex 2ClO_4 on Au(111) after 6 hours, (b) topography after 18 hours (c) line profile indicated by the black arrow in (b) ($I = 30 \text{ pA}$, $U_{\text{bias}} = 2 \text{ V}$, $T = 70 \text{ K}$).

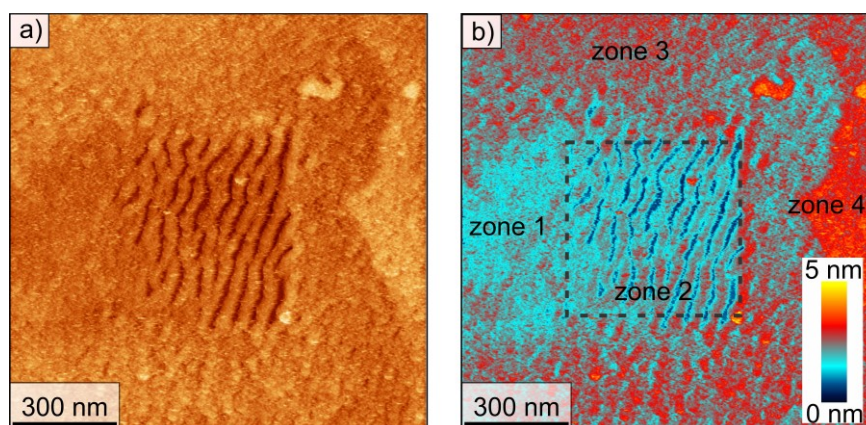


Figure 5.17: (a) Zones of the monolayer before and after tip-interaction, (b) color scale showing the apparent height of the surface.

In order to determine how much the tip-interaction modifies the sample, the area corresponding to the monolayer was measured in a series of topographic images of 500 nm x 500 nm taken systematically during 18 hours (some images correspond to figures 5.15 and 5.16). The calculation of the area was carried out identifying first the area of gold surface by selecting the points on the topography with values of a height lower than 0.75 nm (figure 5.18 bottom-left, black areas-hole) and afterwards, by subtracting from the total area, the area of the monolayer (figure 5.18 bottom-left, green areas-ML). The degradation tendency is shown in the curve of figure 5.18. The monolayer is slightly modified in the first 8 hours, covering the surface of more than 96 %. A linear fit for the data in the first 8 hours (not shown) gives a degradation rate of approximately 0.3 % per hour. After 8 hours of continuous measurement, the film was faster removed with a rate of approximately 1.7 % per hour as is evident in the slope of the curve.

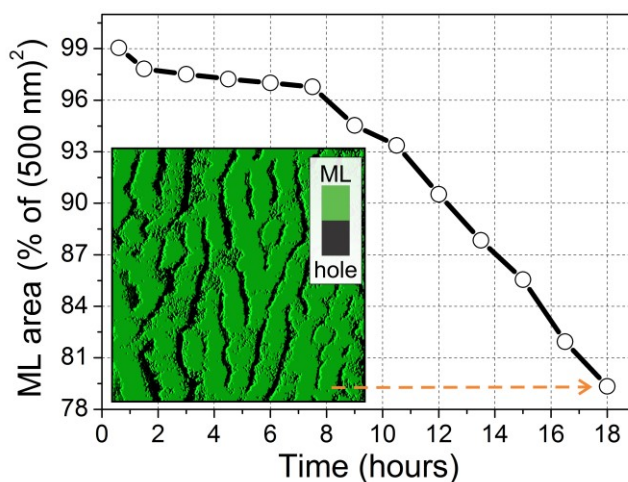


Figure 5.18: Monolayer (ML) area *versus* time.

A further zoom-in, marked with a dashed white line rectangle in figure 5.16 (b), is shown in figure 5.19 (a). It reveals some protrusions on the surface, which are qualitatively comparable with the bright structures plotted in figure 5.12 (b and c). These topographic features corroborate our earlier notion that the surface-bonded dinickel complexes can be directly observed in STM topography measurements. The observed inhomogeneity in size and aspect is reasonable, considering the likely random orientation of the molecules on the surface (see further below). Furthermore, the formation of agglomerates of several molecules is likely to play a crucial role here, particularly in view of the molecules' propensity to stack via $\pi \cdots \pi$ or $\text{CH} \cdots \pi$ interactions [152]. It is worth mentioning in this regard, that the behavior of benzene rings to aggregate *via* $\text{CH} \cdots \pi$ bonds is well known [153] and such interactions are often observed in dinuclear complexes [154].

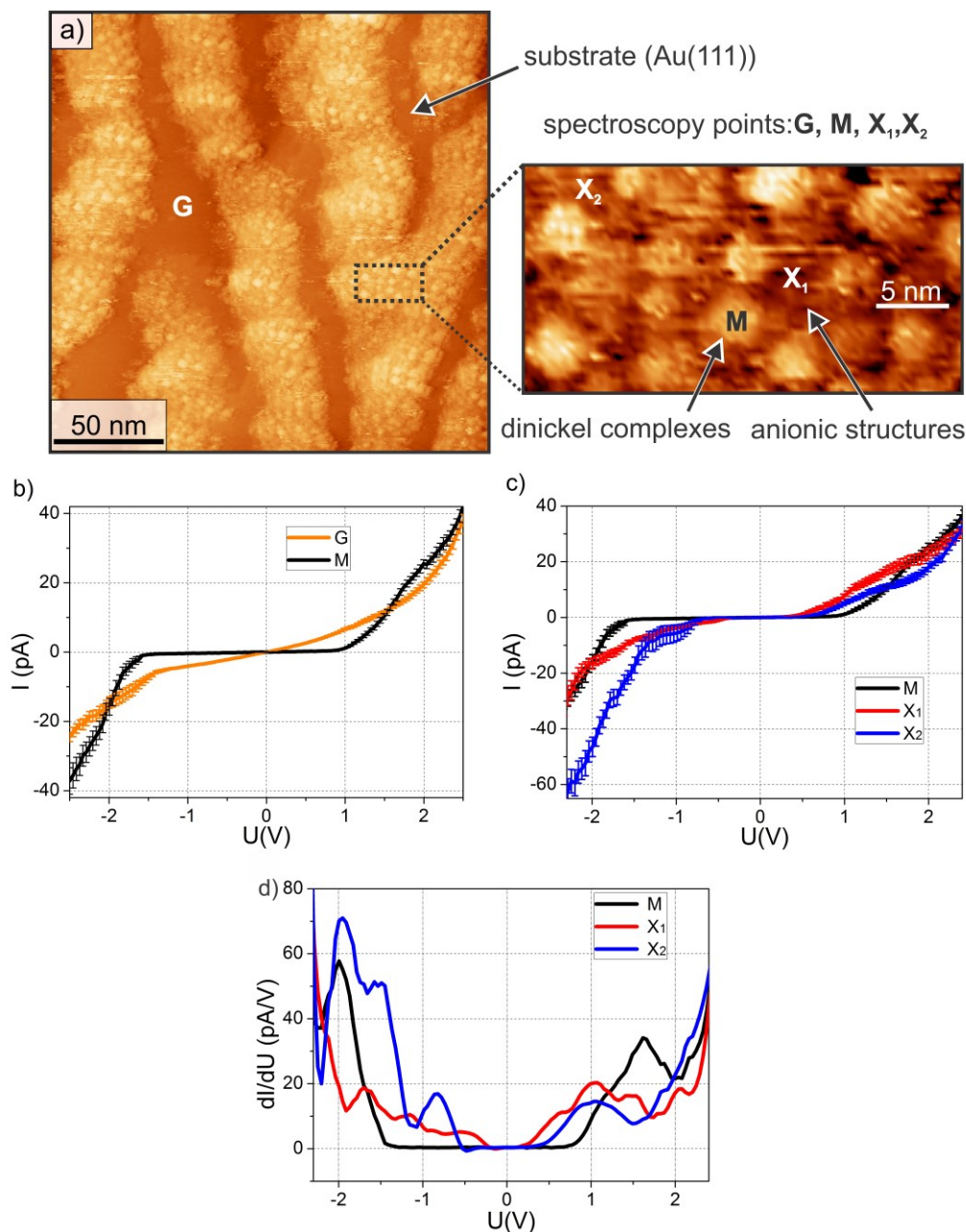


Figure 5.19: (a) Zoom-in image marked with dashed white line rectangle in figure 5.15 (b) and digital zoom-in (30 nm x 15 nm) marked with dashed black line rectangle. (b) Tunneling current *versus* bias voltage taken in the point **G** (orange line) and in **M** (black line). (c) Comparison of the $I(U)$ curves taken in **M**, **X₁**, and **X₂**. (d) First derivative of $I(U)$ curves in (c) (stabilization conditions: $I = 30$ pA, $U_{bias} = 2.5$ V, $T = 70$ K).

In order to analyze the conductance of the sample, spectroscopic curves were taken at different points indicated as: **G**, **M**, **X₁**, and **X₂**. The results are shown in figures 5.19 (b,c,d). In figure 5.19 (b) $I(U)$ curves taken in **G** and **M** are plotted. The $I(U)$ curve taken

at **G** (orange curve in figure 5.17 (b)) shows no gap and linear behaviour around zero bias in good agreement with the band structure of metals and therefore, in this case, corresponds to the gold surface. On the other hand, the curve taken at **M** (black curve) indicates a gap of approximately 2.5 V which is not strictly symmetric with zero bias.

Figure 5.19 (c) shows $I(U)$ curves recorded at different points within the monolayer (**M**, **X₁**, **X₂**). The differential conductance (dI/dU) (figure 5.19 (d)) was calculated out of the curves in figure 5.19 (c) by numerical differentiation. A clear reduction of the gap in the surrounding environment (**X₁**, **X₂**) of the roundish structures marked with **M** is observed.

Discussion: The relatively large initial surface roughness of the low-temperature experiment (figure 5.15 (a)) is likely due to the *ex-situ* conditions of the deposition process.

As is seen in figures 5.16 and 5.17, the tip-interaction modifies the surface of the film basically reducing the surface roughness and after long scanning time removing parts of the film, leaving evidence of the gold surface. The removed parts could be found on the remaining monolayer and also aside from the scan area as is visible in figure 5.17 (b). However, it is also possible that some of them are desorbed to the vacuum. Field-induced and current-induced mechanisms are likely to be responsible for the film modification. Moreover, strong electric fields provided by high bias voltages (higher than 2 V in this case) may yield field-induced molecular desorption. Alternatively, a chemical degradation mechanism, promoted by high electric fields, is likely to be related with electronic reduction processes in the layers: Although the macrocyclic complexes are resistant towards reduction in solution, in a solid phase some reduction processes and thus the destruction of the $[\text{Ni}_2\text{L}(\text{Hmba})]^+$ molecules due to the negatively charged tunneling tip appear possible. Furthermore, it could be possible that reduction of the counterions (ClO_4^-) occurs. The latter has already been seen in XPS experiments [140]. Relatively high tunneling currents also contribute to molecular desorption [133,155,156]. In this work, the sample analyzed using a current of 30 pA and a bias voltage of 2 V (images taken at LT) suffered higher modification in contrast to the sample analyzed using 10 pA and a bias voltage of 2.5 V (images taken at RT). For both mechanisms described above, it is clear that long-term measurements enhance the removing process. Finally, a non-proper adjustment of the bias voltage, in order to tunnel within molecular electronic states, leads to a possible mechanical interaction between the tip and the sample, which could also remove the monolayer. Taking into account that several factors could play a role in the film modification, it is difficult to clearly establish which one has a stronger influence in our experiments. In view of all this, the reason for the apparent two-stage degradation remains unknown. A possible explanation for this is a critical damage that is reached after ~ 8 hours of measurement,

where uncompensated electrostatic forces, due to previously created defects in the monolayer, facilitate the degradation

The length scale over which the film is damaged, in a wavy track manner, may be related to the herringbone surface reconstruction of Au(111), which is known to exhibit different surface reactivity associated to different surface coordination [86]. One may thus speculate, that the bond strength between the sulphur atoms and the Au(111) varies spatially, tracking the herringbone structure. It is interesting to note in this context, that the longer periodicity of the herringbone structure in Au(111) [85] is of the order of ~ 30 nm, which is comparable with the observed width of the molecular stripes in figure 5.16 (b). Furthermore, one cannot exclude the possibility that inhomogeneous electrostatic forces, likely originated from defects in the molecular arrangement, may also contribute to the above mentioned wavy degradation pattern.

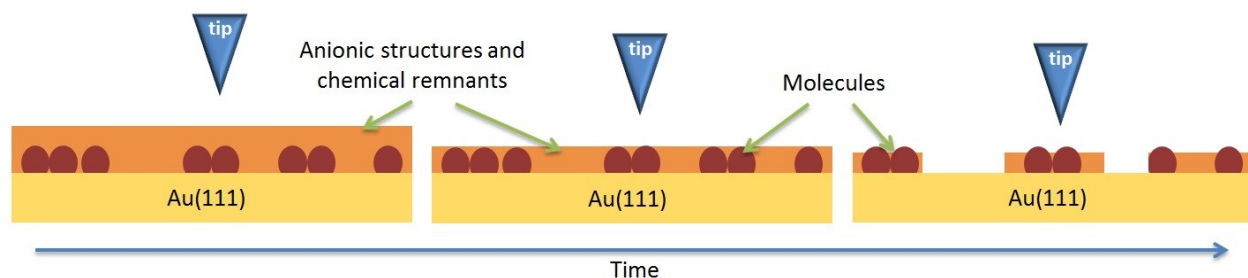


Figure 5.20: Schematic of the tip-interaction with the monolayer.

The monolayers shown in this work exhibit roundish structures surrounded by an environment that in this particular case (bias voltage of 2.5V and 2V) have a darker contrast (e.g. figures 5.12 (b) and 5.19 (a)). Considering that the chemical precursor is a salt, these structures surrounding the molecular complexes should correspond to the counterions ClO_4^- . It let us propose a growth granular model where two structures are involved in figure 5.20. One structure depicted as brown-round entities, representing the cationic dinickel molecular complexes and a second one composed by anions of ClO_4^- , depicted in orange. In this model, the dinickel complexes do not have the chance of establishing any kind of order as they are surrounded by the anionic structures, which does not let them interact properly through any of the ordering forces.

The spectroscopic data taken at the roundish structures marked with **M**, suggest a gap of 2.5 eV, which is in good agreement with the electronic structure of organic layers, with a gap in the order of eV as it has been theoretically shown in related structures [157]. On the other hand, the spectroscopic curves taken in the surrounding structures (**X₁** and **X₂**) show a reduction of the gap. The origin of this relatively small gap is unclear, but may be attributed, in part, to a potential barrier between tip and sample becoming similar to that of the tip-gold configuration.

Surface binding model: Figure 5.21 (a) shows a likely orientation of a single 2ClO_4 on the gold surface. Such a single molecule can be seen as the elementary building block for the observed structures on the surface; either the single molecules or agglomerates of several molecules. The height of the $[\text{Ni}_2\text{L}(\text{Hmba})]^+$ complex on the surface in this case is given by the distance between two opposing N-Me substituents, being approximately 12.5 Å. In an alternate orientation (not shown in Figure 5.21 (a)), the $[\text{Ni}_2\text{L}]^{2+}$ fragment is rotated by 90° around the $\text{O}_2\text{CC}_6\text{H}_4\text{-S}$ bond. In this case, the height is given by two opposing *tert*-butyl CH_3 groups, being 15.5 Å (H32a--H37b); the latter value is calculated by adding the van der Waals radii of two H atoms (2.4 Å) to the atom resulting in a distance of 13.123 Å. This value is in reasonable agreement with the thickness determined by STM measurements (see figures 5.14 (d) and 5.16 (c)). Regardless of the actual orientation of the $[\text{Ni}_2\text{L}]^{2+}$ fragment, the surface complex is presumably also stabilized by van der Waals interactions between the Au surface and the methylene or methyl groups of the supporting macrocycle. However, the thiolate sulphur atoms are out of range of bonding interactions with the Au surface. A further stabilization is likely to occur and compatible with the lateral size of the observed structures through molecule-molecule stacking that could arise from $\text{CH}\cdots\pi$ interactions and lead to molecule pairs (see schematic in figure 5.21 (b)).

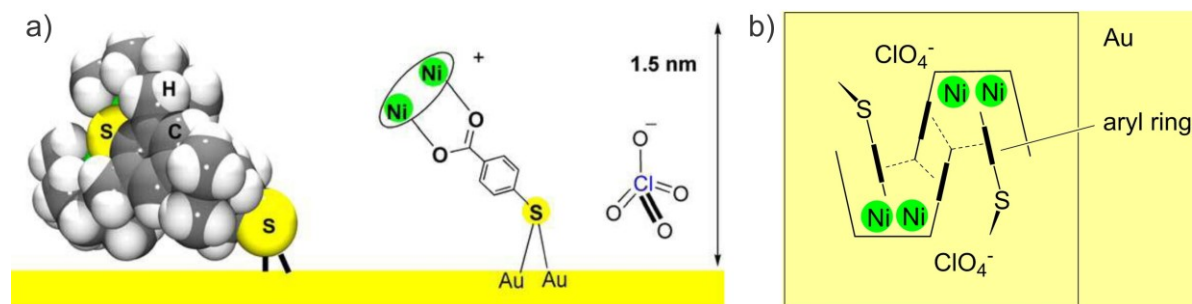


Figure 5.21: (a) Proposed binding model of a single 2ClO_4 to gold. (b) Aggregation model for molecular pairs on gold (top view). Dashed lines indicate the $\text{CH}\cdots\pi$ interactions that potentially lead to molecular binding. Images provided by Prof. Kersting's group.

5.6 Conclusions

This work successfully demonstrated the possibility of anchoring magnetic molecular complexes to gold surfaces *via* ambidentate ligands. The molecular complexes form monolayers with a height of about 1.5 nm. The monolayers contain two apparently granular structures, one cationic structure corresponding to the dinickel molecular complexes and other anionic corresponding to the counterions. No evidence of long or

short range order of these structures was found. Further characterization reveals the tip-interaction with the monolayer due to field and current-induced desorption until the point of damage in some regions. Single point spectroscopy indicates a gap in the molecular complexes of about 2.5 eV and a gap reduction in the anionic environment becoming close to the tip-gold configuration. The height of the monolayers suggests that the molecular complexes are not perpendicular anchored to the gold surface, but they are canted.

6 Iron nanostructures on W(110)

6.1 Motivation

Although the first SP-STM experiment was performed more than 20 years ago (see chapter 2), just a few research groups in the world have successfully implemented the technique. The difficulty in its implementation relies on its special experimental requirements. Firstly, it is necessary to work in extremely clean environments, which is only possible under UHV conditions. These conditions prevent potential sample contamination (e.g. oxidation) as well as guarantee the high reproducibility of the sample and tip preparation. Secondly, low temperature environments are necessary to improve the stability of the system. Experiments conducted at low temperatures, among several other advantages, increase the resolution of the measurements by suppressing: i) the thermal broadening (see chapter 2), ii) the tube scanner drift (see chapter 3), and iii) the atomic diffusion on the sample/tip surface. Furthermore, low-temperature experiments allow the magnetic sample and tip be below the Curie or Néel temperature. This chapter presents the successful implementation of the SP-STM technique at the IFW-Dresden by using the well-known magnetic system Fe/W(110). At the beginning, the physical properties of the system Fe/W(110) are described. Then, the experimental results concerning the growth of iron nanostructures and their magnetic imaging are discussed.

6.2 Iron nanostructures: physical properties

In the past, different groups prepared nanometric iron systems by employing physical vapor deposition techniques with the aim of investigating their magnetic structure by using space average techniques and local techniques like SP-STM. Some relevant examples of such iron systems are islands of one atomic layer, thin films of few layers and three-dimensional islands of hundreds of layers. All of them are achieved by tuning different growth parameters such as coverage, evaporation rates, and temperature, among others. Considering the large number of papers on iron nanostructures, this work will focus on the physical properties of the system Fe/W(110) which has shown excellent multi-faceted structural, electronic and magnetic properties.

6.2.1 Iron nanowires

Magnetic nanowires with a thickness of two monolayers (2 ML) can be achieved by thermal evaporation of between 1 ML to 2 ML of iron on a tungsten single crystal (W(110)). The crystal substrate should be held at approximately 520 K. Figure 6.1 shows on the left, a typical topographic STM image of an alternating array of double-layer and monolayer stripes obtained by step-flow growth, while the right depicts a three dimensional sketch of the mentioned array.

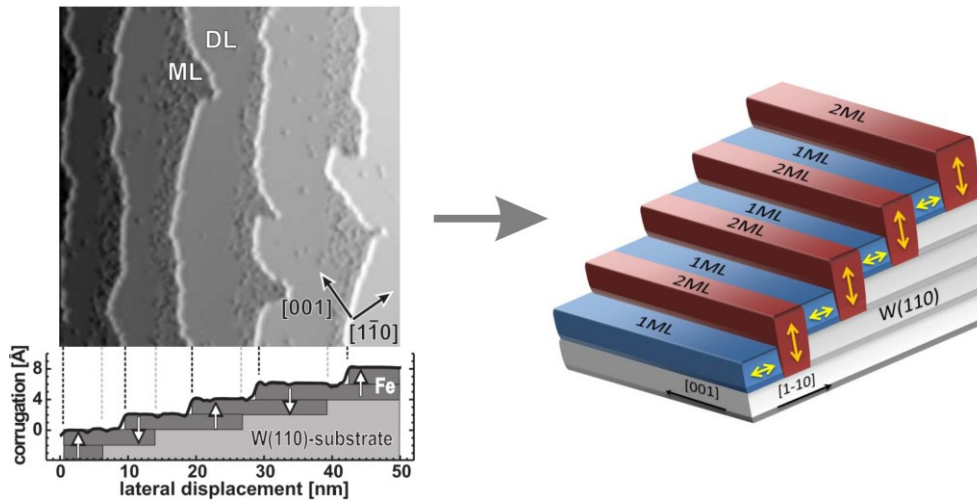


Figure 6.1: On the left, STM image of alternating double-layer and monolayer stripes, taken from reference [158]. On the right, schematic in 3D of the left-hand STM image; yellow arrows indicate the magnetic easy axes.

Structural and magnetic properties of the double-layer iron nanowires are strongly determined by the large lattice mismatch between iron and tungsten ($a_{\text{Fe}} = 2.8665 \text{ \AA}$ and $a_{\text{W}} = 3.165 \text{ \AA}$) [159]. In the growth of the first layer of iron, high strain is present. This strain is responsible of diverse surface reconstructions which are visible in STM (see figure 6.2) [48]. One of the consequences of such a large mismatch in the second monolayer is the formation of sporadic dislocations lines along the [001] direction of the surface. In the third layer a regular pattern is also created, with characteristic lines pointing to the [001] direction; while from the fourth till the twelfth layer a two-dimensional network is observed. This network has a lattice constant of 40.5 \AA along [1-10] and 28.6 \AA along the [001] direction. When more layers are added, the iron systematically relaxes and reaches the bulk lattice constant [48,160].

The system iron on W(110) has been investigated through techniques like the magneto-optical Kerr effect and SP-STM, revealing in the first atomic layer of iron a magnetic easy axis along the [1-10] direction, i.e. in-plane easy axis, with a Curie temperature of 230 K [161]. In contrast, two atomic layers of iron exhibit out-of-plane magnetic easy

axis (orthogonal with in-plane) and systems with more than two atomic layers of iron possess again in-plane magnetic easy axis. However, it is also known that at 22 atomic layers the easy axis stays in-plane but changes its direction from $[1-10]$ to $[001]$ [162].

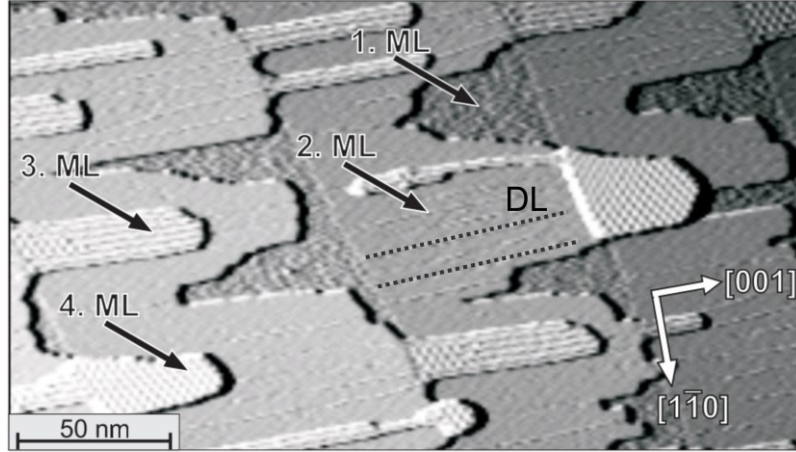


Figure 6.2: Sample of 2.5 ML of Fe on W(110) grown at $T = 500$ K, local coverage is indicated in monolayers (ML). Some dislocation lines (DL) in the 2. ML are highlighted with dashed lines, taken from reference [48].

In the first years of investigation on pseudomorphic iron films grown on stepped W(110) surfaces by using Kerr magnetometry (MOKE), it was not clear what caused the onset of perpendicular magnetization in nanostripe arrays of alternating double-layer and monolayer stripes (see figure 6.1). However, a micromagnetic model proposed by Elmers *et al.*, considering the strain anisotropy induced by epitaxial strain [163,164], successfully explained the experimental results. This model takes into account that the structural difference of approximately 10 % in the lattice parameters of iron and tungsten induces a huge strain anisotropy preferring an out-of-plane easy axis in the double-layer patches instead of in-plane, which might be promoted by dipolar and surface anisotropies (see figure 6.3) [165]. In this manner, the model treats a periodic array of stripes with alternating orthogonal uniaxial anisotropies (see figure 6.3 top). Despite the discontinuous change of anisotropy from an out-of-plane easy axis in the double-layer stripe to an in-plane easy axis in the monolayer stripe, the magnetization direction changes continuously on a lateral scale given by the exchange length. The magnetization direction is specified by the angle $\vartheta(x)$ with respect to the film normal as a function of the x coordinate, along the $[1-10]$ direction (across the stripe array) (see figure 6.3). a_{DL} and a_{ML} are the widths of the double-layer stripe and the monolayer stripe, respectively, and $x = 0$ denotes the boundary between the double-layer region for $x < 0$ and the monolayer region for $x > 0$. Thus, $\vartheta(x)$ was calculated by the minimization of the free energy γ per period $L = a_{DL} + a_{ML} = 9$ nm:

$$\gamma = 2 \int_{-a_{DL}/2}^{+a_{ML}/2} \left\{ A_i t_i \left(\frac{d\vartheta}{dx} \right)^2 + K_i t_i (\sin \vartheta)^2 \right\} dx. \quad (6.1)$$

The exchange stiffness A_i , the anisotropy constant K_i and the film thickness t_i are constants except for a discontinuous change at $x = 0$ ($i = ML$ for $x < 0$ and $i = DL$ for $x > 0$). One of the main results, after the analytical solution of the variational problem enounced in equation (6.1) [165], was the calculation of a critical value for the width of a double-layer stripe (equation 6.2), when the $\vartheta(x)$ switches from in-plane state ($\vartheta(x) = \pi/2$) to out-of-plane ($\vartheta(x) = 0$):

$$a_{DL,c} = 2L_{DL} \arctan\{\alpha \tanh(a_{ML}/2L_{ML})\}, \quad (6.2)$$

where $L_i = \sqrt{A_i/|K_i|}$ is the exchange lengths and $\alpha = \sqrt{(A_{ML}|K_{ML}|t_{ML}^2)/(A_{DL}|K_{DL}|t_{DL}^2)}$.

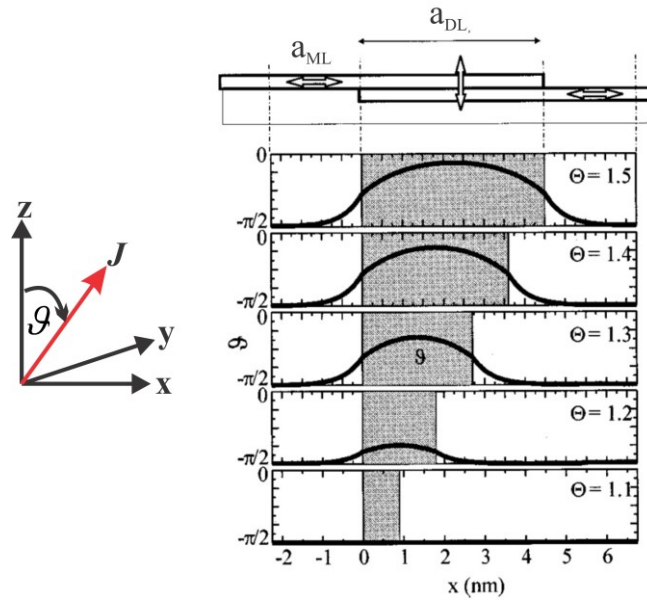


Figure 6.3: Numerical results from micromagnetic theory for the angle of magnetization (ϑ) with respect to the z -axis as a function of the double layer width. The periodic stripe array (see schematic illustration on top) has a width $L = a_{ML} + a_{DL} = 9$ nm. Θ is the sample coverage in monolayers (ML) and J the magnetization vector. Parameters used for the calculation: anisotropy constants $K_{ML} = -5 \times 10^6 \text{ Jm}^{-3}$ and $K_{DL} = +1 \times 10^6 \text{ Jm}^{-3}$, exchange constant $A = 10^{-12} \text{ J/m}$ by H.J. Elmers *et al.* [165,166].

For a quantitative discussion Elmers *et al.* took effective values for the anisotropy constants K_i , determined from torsion oscillation magnetometry: $K_{ML} = -5 \times 10^6 \text{ Jm}^{-3}$ for the monolayers and $K_{DL} = +1 \times 10^6 \text{ Jm}^{-3}$ for double-layer islands [167]. The authors assumed for simplicity $A_{ML} = A_{DL} = A$. Numerical calculations for the magnetization

direction $\vartheta(x)$ as a function of the double-layer width, which is directly related to sample coverage Θ , are shown in figure 6.3. They illustrate the onset of a perpendicular remanent magnetization near a coverage of 1.1 ML as was observed through Kerr effect experiments (see more details in [166]).

The magnetic structure of iron nanowires formed by two atomic layers is strongly defined by their width. Consequently, the width of the wires depends on the width of the tungsten steps and the iron coverage in the sample. Additionally, the width of the steps in a single crystal can be defined by its miscut, which refers to the cutting angle of the tungsten crystal oriented in the [1-10] direction. Thus, a miscut of 1.35° ends with a step-width of about 9 nm, whereas a miscut of 0.64° provides step-widths of about 20 nm, as shown in figure 6.4 [158].

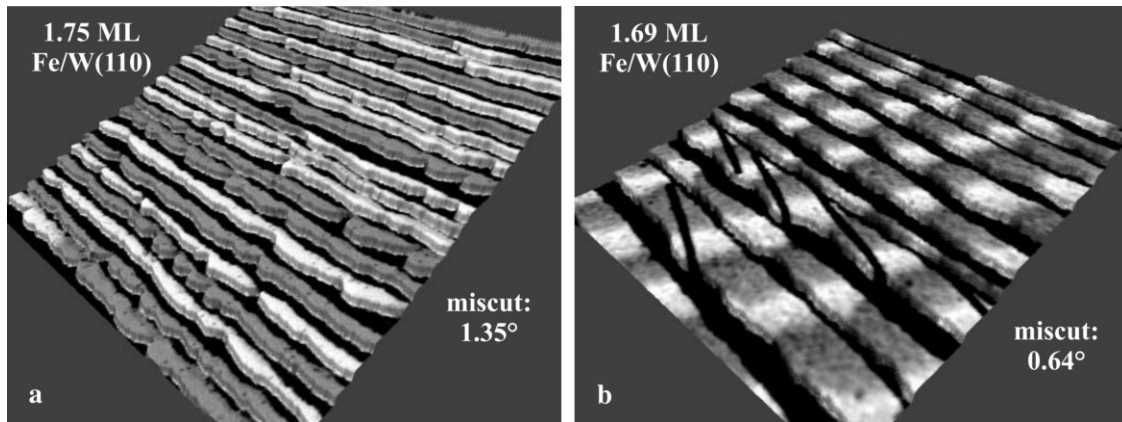


Figure 6.4: Perspective topographic images (200 nm x 200 nm) of Fe nanostripes prepared on different W(110) substrates combined with grey scale representations of the magnetic dl/dU signal: (a) 1.75 ML Fe deposited on a substrate that is miscut by 1.35° with respect to the (110) plane; and (b) 1.69 ML Fe deposited on a substrate which exhibits a smaller miscut of about 0.64° . Both images taken from reference [158].

Figure 6.4 (a) shows iron nanowires with a width of about 6 – 7 nm. The gray scale, representing the spin-resolved spectroscopic dl/dU signal, reveals an alternating out-of-plane (up and down) magnetization direction between adjacent double-layer wires. This image shows us that the iron nanowires are antiferromagnetically coupled due to magnetostatic interactions (see schematic in figure 6.5 (a)). On the other hand, figure 6.4 (b) shows iron nanowires with a width of approximately 20 nm. In this case, each nanowire presents a periodical change of the out-of-plane magnetization (up and down) by introducing several domain walls in the [1-10] direction (see schematic in figure 6.5 (b)). The latter indicates that the adjacent wires are ferromagnetically coupled [29,158]. But each nanowire has a helical magnetic structure where the domain walls are of Bloch-

character, which means that the changing of the magnetization is done by rotation of the magnetization vector around the $[001]$ direction (see schematic in figure 6.5 (c)) [48].

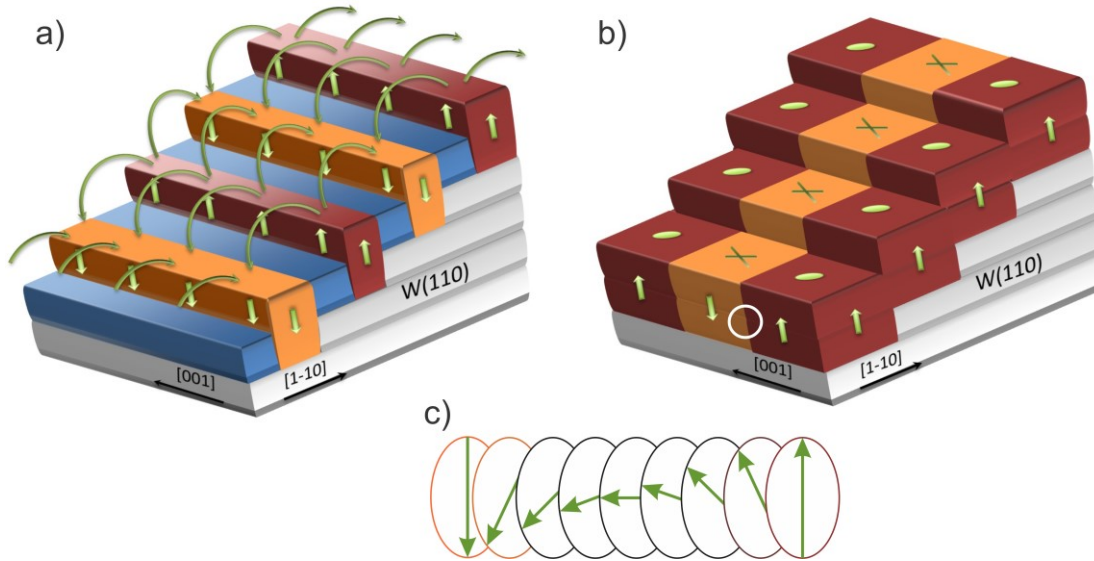


Figure 6.5: (a) Schematic illustration of antiferromagnetically coupled iron double-layer nanowires, (b) schematic of double-layer iron nanowires ferromagnetically coupled, (c) Bloch domain wall indicated in (b) with a white circumference.

One interesting characteristic of ferromagnetically coupled iron nanowires on W(110) is that the domain walls have different electronic density of states in comparison to the domain cores. This fact makes conventional STM/STS also capable of detecting the magnetic structure of iron nanowires by revealing the domain walls. DFT calculations attributed this fact to a spin-orbit coupling effect [59,168].

6.2.2 Iron islands

In the system Fe on W(110), one can find islands with diverse sizes and thickness, which determine their magnetic structure. One of the simplest cases are islands in the sub-monolayer regime, e.g. islands of one atomic layer. These islands have special magnetic characteristics depending on their size: whereas small islands present superparamagnetic behaviour, large islands could become ferromagnetic with an easy axis lying in the sample plane [61,161].

Another case are islands of two atomic layers. These islands are ferromagnetic, but depending on their size, present different easy axes of magnetization. Small islands keep the in-plane magnetization inherited by the first complete monolayer, whereas bigger islands switch the easy axis of magnetization perpendicularly with respect to the sample surface (out-of-plane), as was previously discussed for double-layer iron nanowires [61,169].

Figure 6.6 left is an example of a topographic STM image of double-layer iron islands surrounded by the first layer of iron on W(110); while Figure 6.6 right corresponds to its dI/dU -map acquired by using an out-of-plane magnetized tip. The latter shows that some of the islands are dark and others are bright. This difference in the dI/dU contrast is related to the two possible out-of-plane alignments of the magnetization direction of the islands with respect to the tip: parallel (bright contrast) in some cases, and antiparallel (dark contrast) in others.

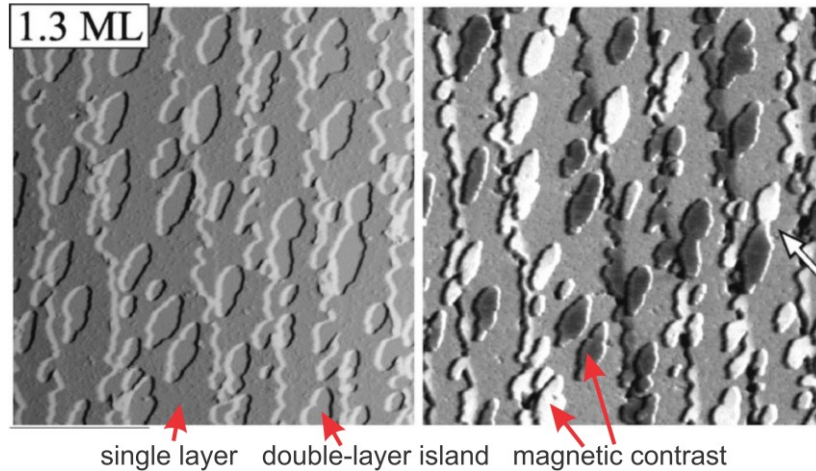


Figure 6.6: On the left, STM image of double-layer iron islands, total coverage 1.3 ML. On the right, dI/dU signal revealing the magnetic structure on double-layer iron islands, taken from reference [169].

Figure 6.7 shows further analysis of dI/dU -maps taken with an out-of-plane magnetized tip on double-layer islands. This analysis confirms that islands with a geometrical width (i.e. along the [1-10] direction) larger than 3.2 nm are out-of-plane magnetized (region I in figure 6.7 (a)). Some of these islands are parallel magnetized with respect to the tip magnetization, exhibiting the highest dI/dU signal; whereas the others are antiparallel magnetized, exhibiting the lowest dI/dU signal. Islands in Region II are in a crossover region, which means that these islands (width: 1.8 - 3.2 nm) do not have a clear out-of-plane magnetization. Islands in region III do not show out-of-plane magnetization but as was mentioned before, they have in-plane magnetization (see figures 6.7 (b) and (c)).

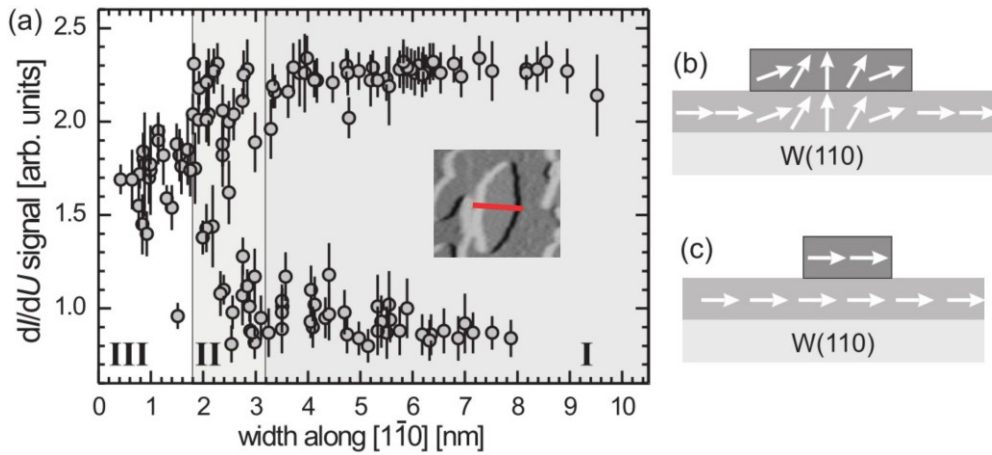


Figure 6.7: On the left, plot of dI/dU signal strength measured by an out-of-plane magnetized tip on 140 individual double-layer Fe islands *versus* their geometrical width along the $[1-10]$ direction, i.e. the short island axis (depicted in red in the inset). On the right, (b) schematic of magnetization rotation in large double-layer islands due to strain anisotropy with out-of-plane easy axis, (c) schematic of in-plane magnetization of small double-layer islands due to dominance of surface anisotropy (in-plane easy axis), taken from reference [61].

Iron islands of more than two atomic layers on W(110) are characterized by in-plane anisotropy. However, these islands show a variety of surface magnetic configurations depending mostly on their thickness.

Figure 6.8 shows examples of iron islands with varying thicknesses, ranging from approximately 3.5 nm to 8.5 nm. Additionally in this figure, SP-STM images (dI/dU -maps) and schematic illustrations of the surface magnetic structures are shown. Figure 6.8 (a) shows islands of approximately 3.5 nm height in a mono-domain magnetic configuration. The SP-STM image shows islands aligned parallel to the tip magnetization in bright contrast and others aligned antiparallel in dark contrast. Figure 6.8 (b) shows the example of a higher island of approximately 5.5 nm, where there are two opposite magnetic domains. Figure 6.8 (c) presents an island of about 8 nm height exhibiting a vortex magnetic configuration and figure 6.8 (d) shows the example of an island of about 8.5 nm height, where there are two magnetic vortices (diamond configuration) [170].

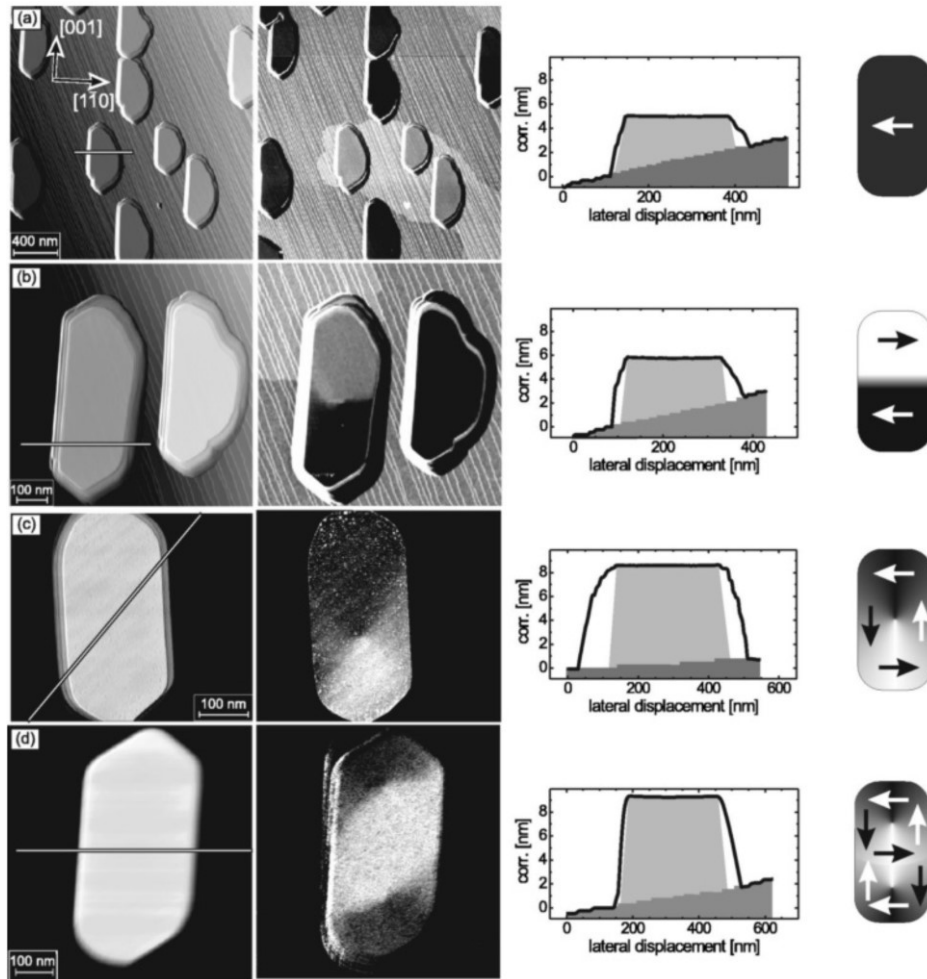


Figure 6.8: 3D iron islands on W(110), images taken with an in-plane magnetized tip; topography, SP-STM image, height and magnetic structure. (a) mono-domain structure ($\sim 3,5$ nm height), (b) two-domains structure ($\sim 5,5$ nm height), (c) vortex state (~ 8 nm height), (d) diamond state ($\sim 8,5$ nm height). Taken from reference [170].

6.3 Results I: Growth of iron nanostructures on W(110)

In order to grow iron nanostructures, a single crystal of tungsten oriented in the [110] direction has been used as a substrate. The cleaning procedure of the dense-packed W(110) surface was based on several cycles of prolonged annealing under oxygen atmosphere followed by the subsequent short high-temperature treatments (see more details in chapter 4) [171]. A topographic image of the substrate W(110) (see figure 6.9 (a)) shows the characteristic surface with mono-atomic steps of about 0.2 nm in height.

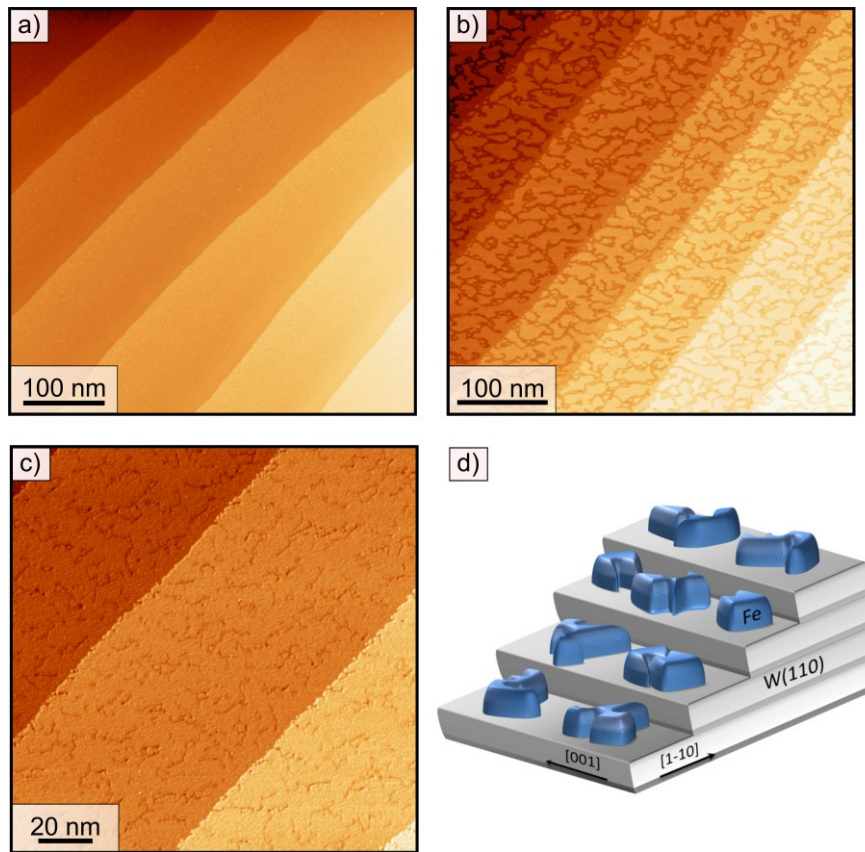


Figure 6.9: Sub-monolayer coverage of Fe on W(110). (a) STM image of a single crystal W(110) ($I = 100$ pA, $U = -20$ mV, $T = \text{RT}$), (b) 0.75 ML Fe on W(110) ($I = 10$ pA, $U = -20$ mV, $T = \text{RT}$), (c) 0.97 ML Fe on W(110) ($I = 15$ pA, $U = -300$ mV, $T = 38$ K), (d) corresponding Schematic illustration of the Fe growth in sub-monolayer regimens. Note: the scale in the plane is much different to the out-of-plane in (d).

Once the substrate was prepared, iron was evaporated at a constant rate of 0.1 ML/minute². Several samples of iron deposited on W(110) were prepared with varying parameters, in particular the substrate temperature and the coverage. As a result, different systems of iron deposited on W(110) were obtained. Figures 6.9 (b) and (c) show iron layers in sub-monolayer coverage (see schematic illustration in figure 6.9 (d)). In order to calculate the coverage of each sample, the visible area of the substrate W(110) was measured by identifying the points on the image with a height below 0.1 nm, with respect to the tungsten substrate. The resulting coverages were 0.75 ML in figure 6.9 (b) and 0.97 ML in figure 6.9 (c).

² The evaporation rate was calibrated by measuring the evaporation time and the obtained coverage of several samples through STM.

As we can observe in figures 6.9 (b) and (c), before the first iron monolayer is completely formed, the growth of structures of two atomic layers is not present. This points out that the interaction between the iron atoms and the tungsten substrate is stronger than the interaction between only iron atoms.

After the formation of the first iron layer, so-called wetting layer, the new evaporated atoms find a different substrate. It means that the interactions between these new iron atoms and the substrate (1ML Fe on W(110)) will be different, and as a result, new structures will appear in the coverage regime between 1ML and 2ML.

Figure 6.10 (a) shows a sample with a coverage of about 1.4 ML evaporated on a substrate held at 230 °C. The main observation is the formation of elongated islands of two atomic layers sparse over the surface (see schematic illustration in figure 6.10 (d)) and additional tiny structures of three atomic layers on top of the 2 ML-islands. On the other hand, figure 6.10 (b) shows a sample with a coverage of 1.6 ML evaporated on a substrate, in this case, held at 300 °C with 5 minutes of annealing. We obtained islands of two atomic layers again, but this time due to the effect of the substrate-temperature, the islands are bigger and grow preferably away from the crystal step edges. These islands do not have small 3 ML-islands on top, which proves the enhancement of the adatoms mobility due to the thermal energy provided during film growth.

The image shown in figure 6.10 (c) corresponds to a sample achieved by evaporating 1.4 ML of iron on a W(110) substrate held at 300 °C and with annealing of about 30 minutes after iron evaporation. In this particular case, the 2 ML-islands coalesce, forming 2ML-wires at the crystal step edges (see figure 6.1 right).

Iron films with higher coverage than 1 ML suffer strain due to the misfit ($\sim 10\%$) between the lattices of the substrate and the film. This film-strain is proportional to the film-thickness. It is well-known [172] in these systems that beyond a critical thickness, the strain energy becomes large enough to initiate one of many possible strain-relieving mechanisms. In 2ML-wires, the strain-relieving mechanism is the introduction of misfit dislocations at the film-substrate interface. In the topographic image shown in figure 6.10 (c), dislocation lines are not visible. However, in the dI/dU -map shown further below in figure 6.15 (b), dislocation lines are clearly visible. Another different strain-relieving mechanism is the formation of 3D-islands which occurs at high (> 600 °C) substrate temperature (see figure 6.11 (c) and (d)).

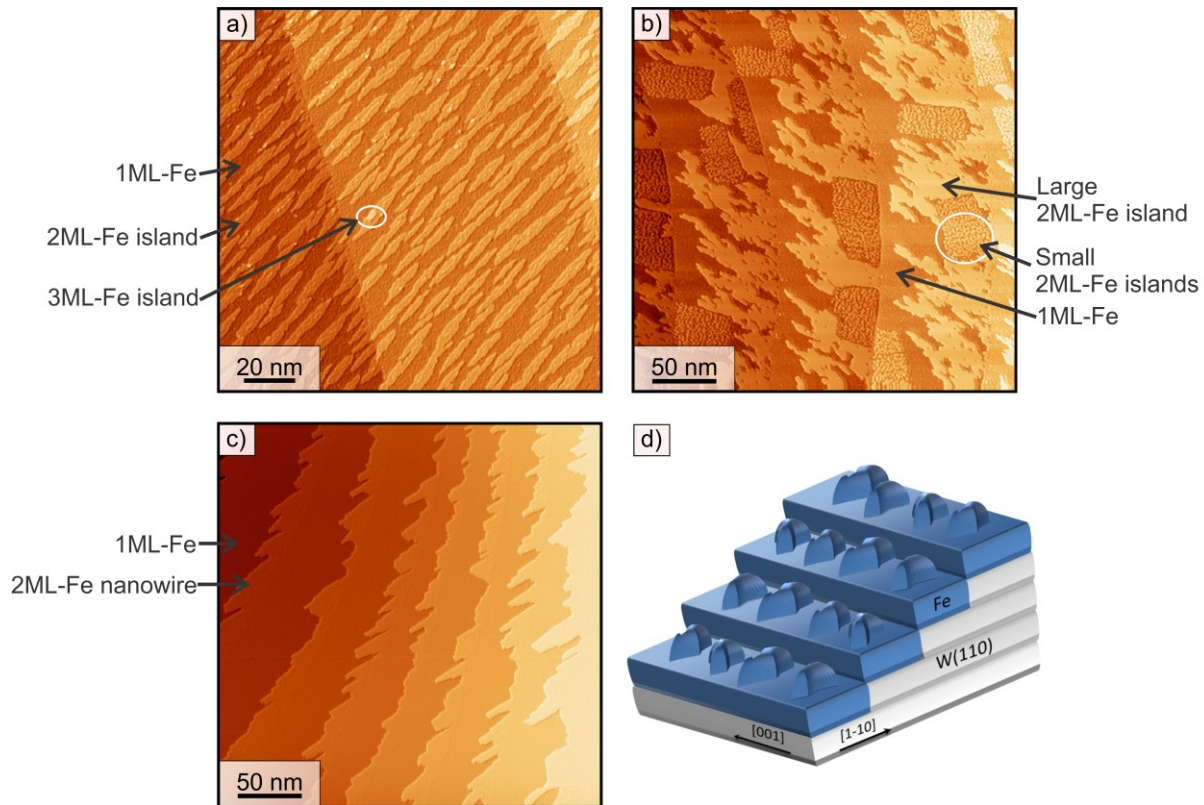


Figure 6.10: Coverage between 1 ML and 2 ML of Fe on W(110). (a) STM topographic images of 1.4 ML Fe on W(110) grown at 230 °C ($I = 100$ pA, $U = -300$ mV, $T = 38$ K), (b) 1.6 ML Fe on W(110) grown at 300 °C ($I = 300$ pA, $U = -300$ mV, $T = 38$ K), (c) 1.4 ML Fe on W(110) grown at 300 °C ($I = 300$ pA, $U = 50$ mV, $T = 38$ K), (d) corresponding schematic illustration of the Fe growth. Note: the scale in the plane is much different than out-of-plane in (d).

Figure 6.11 shows samples with higher coverage than 2 ML. In particular, the sample in figure 6.11 (a) was prepared with approximately 15 ML on a W(110) substrate held at 270 °C with subsequent 10 minutes of annealing. In this sample the iron film shows a square surface reconstruction depicted in figure 6.11 (b) with a lattice parameter of about 2.5 nm. For the system Fe/W(110), it is known [48] that structures with local coverage of 4 ML up to 12 ML show a two-dimensional reconstruction network with a lattice constant of 4.05 nm in [1-10] and 2.86 nm in the [001] direction. Furthermore, at higher coverage, iron is completely relaxed and reaches the bulk iron lattice constant. This implies that the number of iron layers shown in figure 6.11 (a) is larger than 12, because the lattice parameter (2.5 nm) of the surface reconstruction is smaller than any of the lattice parameters in a system between 4 ML and 12ML. Furthermore, it shows that the lattice is relaxing towards a total lattice relaxation of iron, which would have the bulk lattice parameter of 2.856 Å [88].

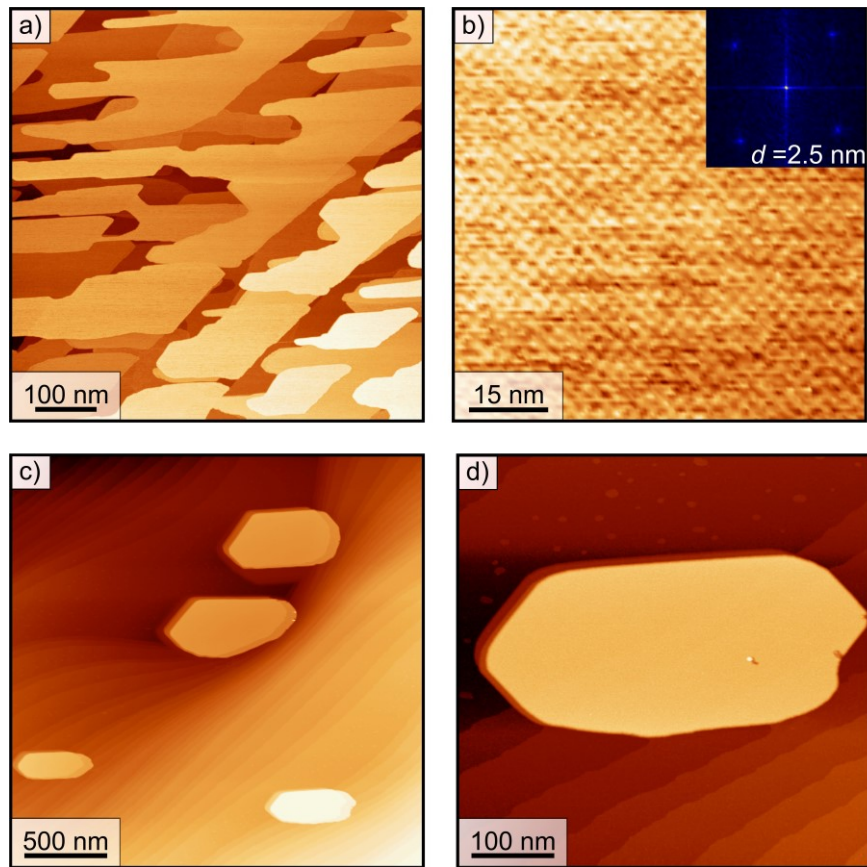


Figure 6.11: High coverage Fe/ W(110)-systems. (a) STM topographic images of ~ 15 ML Fe grown on W(110) at 280°C ($I = 10$ pA, $U = -200$ mV, $T = \text{RT}$), (b) digital zoom-in from the region highlighted with a dashed square in image (a) (inset, Fast Fourier Transform (FFT) on topography); (c) 3D-islands of Fe on W(110) grown at 660°C with 10 min annealing ($I = 10$ pA, $U = -200$ mV, $T = \text{RT}$), (d) zoom-in from the region highlighted with a dashed square in image (c).

Figures 6.11 (c) and (d) can be interpreted as 3D-islands surrounded by the iron wetting layer. The 3D-islands were obtained by evaporating approximately 15 ML on a W(110) substrate held at 660°C with subsequent 10 minutes of annealing. The latter samples clearly show the so-called Stranski-Krastanov growth, where in the initial stage of the film growth, the wetting layer formation is privileged and afterwards the 3D-islands formation takes place [173].

In figure 6.12 (a) we can see a broad sample-overview containing different types of 3D-islands. As an example, figure 6.12 (b) shows a line profile taken along the longest geometrical direction of an island in (a). Here we can observe the variation of the height due to the slope of the substrate. Additionally, it is possible to see atomic steps of the W(110) wetted with the first iron layer. The histograms in figures 6.12 (c) and (d) show us the island average heights and the area, respectively. One can notice that the islands

size is quite diverse, finding heights from 3 nm to 11 nm, and areas between 1589 nm² and 135641 nm².

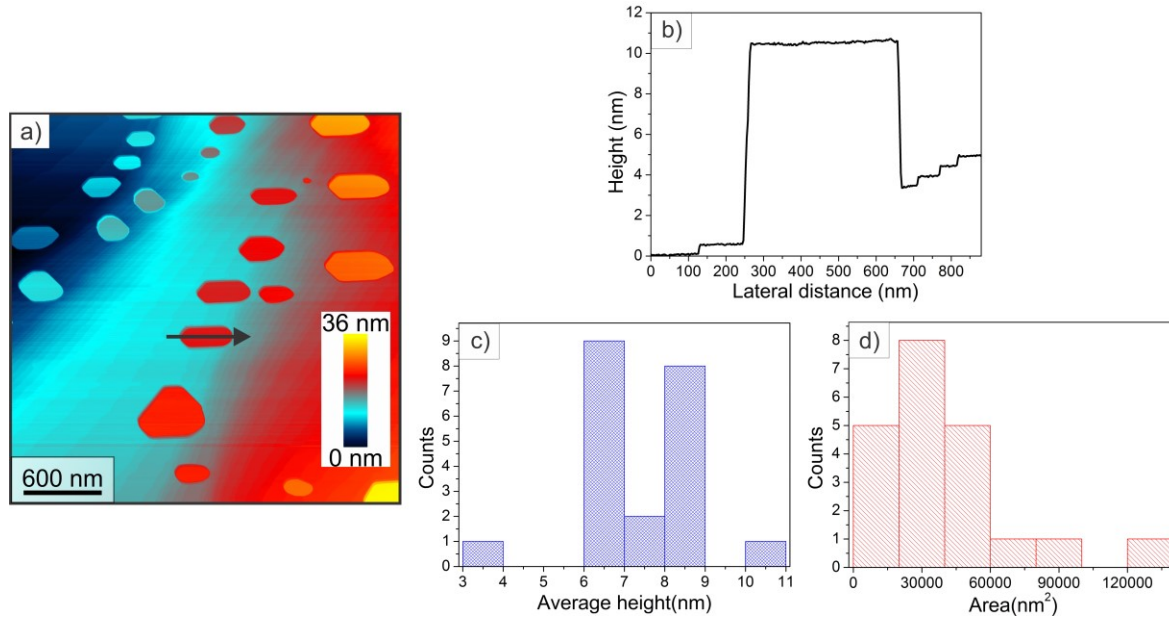


Figure 6.12: 3D-iron islands on W(110). (a) Topographic STM image of different 3D-islands ($I = 20$ pA, $U = -200$ mV, $T = RT$), (b) corresponding line profile through the longest geometrical direction of the island shown in figure (a), (c) histogram of islands-average height, (d) histogram of islands-area.

6.4 Results II: Spin-polarized tunneling on iron nanostructures: magnetic imaging

One way to measure the spin contribution to the height (h) in topography and to the differential conductance (dI/dU) in dI/dU -maps is through the asymmetry. The asymmetry is a coefficient which compares two signals of the same nature as defined by equation 6.3.

$$Asymmetry = \frac{A - B}{A + B} \quad (6.3)$$

In the case of equality between two compared signals, the asymmetry will be zero. Otherwise the coefficient will show how much bigger one signal is with respect to the other.

Figure 6.13 shows the first result of spin-polarized tunneling on a sample of 1.6 ML of iron on W(110), measured with an iron-coated tungsten tip. Figure 6.13 (a) is the topographic image of the sample already described in figure 6.10 (b). In this figure, as it

was previously mentioned, one can recognize large 2ML-Fe islands surrounded by the iron wetting layer and small 2ML-islands.

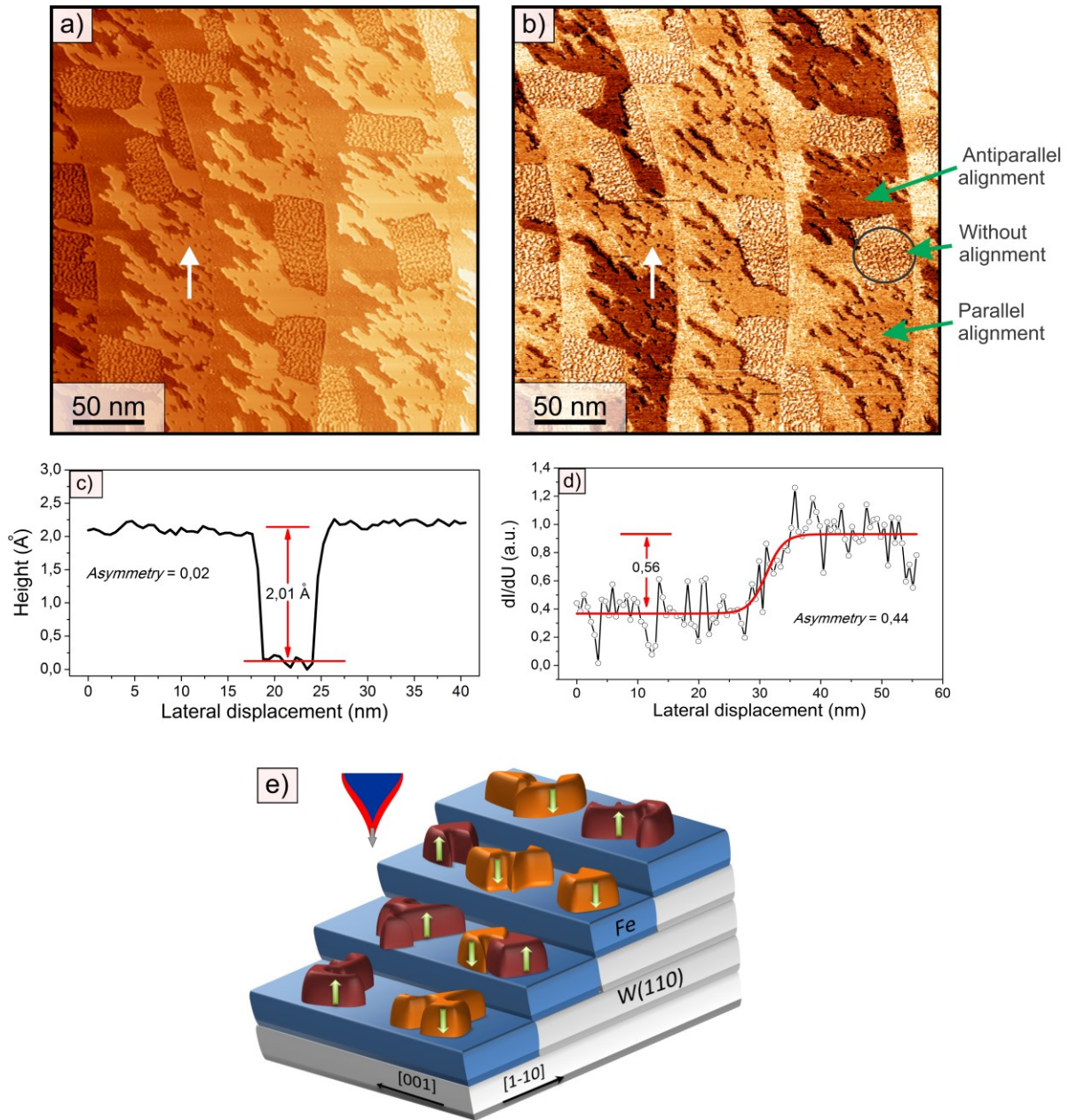


Figure 6.13: 1.6 ML of Fe on W(110) measured with an iron-coated tungsten tip. (a) Topographic image ($I = 300$ pA, $U = -300$ mV, $T = 38$ K), (b) dI/dU -map @ $U = -300$ mV ($U_{mod} = 100$ mV, $f_{mod} = 3$ KHz), (c) line profile along white arrow in (a), (d) line profile along white arrow in (b), (e) corresponding schematic illustration of the magnetic islands. Note: i) the alignment condition indicated in (b) is between the magnetic moments of the tip and sample and ii) the scale in the plane is much different to the out-of-plane in (e).

Figure 6.13 (b) is a dI/dU -map taken at -300 mV bias voltage. Here we can clearly see on the bigger islands that the dI/dU signal substantially differs. In order to analyze these differences, line profiles were taken along the white arrows in figures 13 (a) and (b), respectively. The white arrows are located on top of two separated islands. The line profile presented in figure 13 (c) (taken at (a)) shows an average height in one island of about 1.97 Å, whereas in the other of about 2.07 Å. Both heights are in between the real value of 2.019 Å. Applying the equation 6.3 to the average heights of the two islands, the asymmetry coefficient is 0.02, indicating nearly no difference in the signals. In contrast, the line profile in figure 13 (d) (taken at (b)) shows that the dI/dU signal of the two islands has a significant asymmetry of 0.44.

The observed differences in the two 2ML-islands, in height as well as in the dI/dU signal are due to the spin contribution to the tunneling current. As was discussed in chapter 2, the parallel and the antiparallel alignment of the magnetic moments of tip and sample affect the apparent height and the differential conductance probed on magnetic structures. In this sense, the dark islands mainly align their magnetic moments antiparallel with respect to the tip magnetic moment and vice versa in the case of the bright islands (see schematic in figure 6.13 (e)). In this sample, we observe that the big islands are magnetic domains probably anti-ferromagnetically coupled with the closer ones. The magnetization direction, based on previous knowledge, is out-of-plane [29].

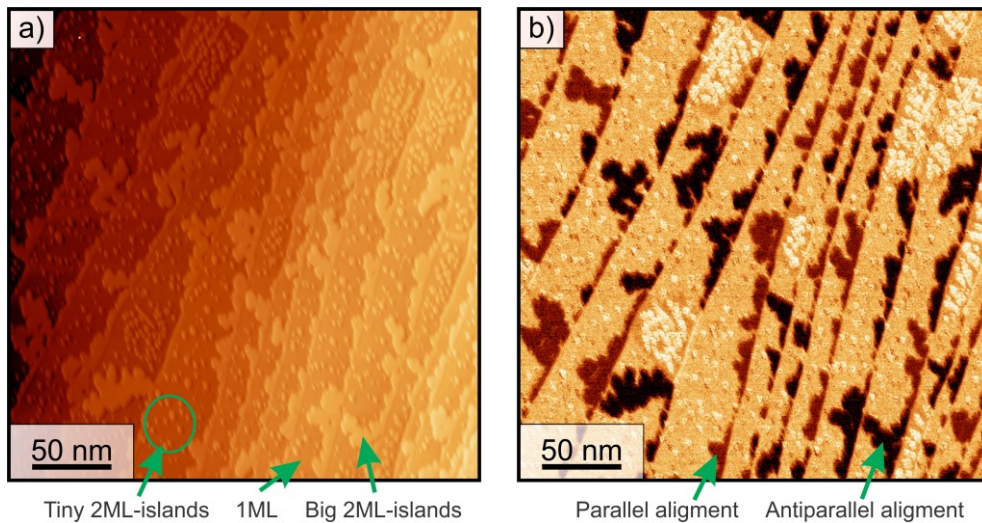


Figure 6.14: 1.4 ML of Fe on W(110) showing tiny and big 2ML-islands measured with an iron-coated tungsten tip. (a) STM topography image ($I = 300$ pA, $U = -150$ mV, $T = 38$ K), (b) dI/dU -map @ $U = -150$ mV revealing magnetic mono-domains in big islands and non-magnetic contrast in tiny islands ($U_{mod} = 100$ mV, $f_{mod} = 3$ KHz).

Although iron coated tungsten tips have mainly exhibited in-plane magnetic polarization, there are examples, such as the one presented here, that have exhibited out-

of-plane polarization [61]. When considering the reasons for the out-of-plane polarization of iron coated tips, one should take into account the fact that the tip material is not a single crystal and the tip treatment previous to the measurement might create clusters, which deviate from a perfectly smooth film on the tungsten tip [174]. The tip polarization therefore, might be slightly canted and could be sensitive to both out-of-plane and in-plane polarizations [100]. Furthermore, it is possible to see in the sample, that the tiny 2ML-islands do not have enough size to keep the same magnetization direction as the big ones. One can finally recognize, that the large asymmetry in the dI/dU signals in comparison with the asymmetry in the heights indicates the usefulness of the dI/dU -maps revealing the magnetic structure.

Figure 6.14 represents another example of iron magnetic 2ML-islands, but in this case, the dI/dU -map shown in figure 6.14 (b) was taken at -150 mV bias voltage. One can recognize the magnetic structure of the sample again, however, the contrast between the big islands differs in comparison with the ones shown in figure 6.13. This suggests a dI/dU signal dependence on the energy (bias voltage), which in principle can arise from the energy dependence of the spin-polarized-DOS (see also further below). It should be noted that in addition to the discussed 2ML-islands, this sample shows small islands with different contrast than the big ones, although they have the same thickness.

In order to study more in detail the dependence on energy of the dI/dU signal, another example of magnetic imaging is shown in figure 6.15. In this case, 1.4 ML of iron on W(110) forms a system of 2ML-nanowires as was previously described in figure 6.10 (c). Figures 6.15 (b), (c), and (d) are dI/dU -maps taken at bias voltages of -50 mV, +50 mV, and -100 mV, respectively. Figure 6.15 (b) shows clear contrast between the double layer nanowires and the wetting layer. Additionally, lines almost perpendicular with the step edges are visible. Figures 6.15 (c) and (d) show contrast mainly within the 2ML-nanowires, however, the contrast within the nanowires is opposite in these images. The contrast shown at -50 mV is purely electronic due to the different DOS between monolayer and double-layer structures. Moreover, the visible lines within the nanowire correspond to dislocation lines as was explained in figure 6.10 (c). But, the clear contrast at +50 mV and -100 mV within the nanowires has a magnetic origin coming from the different DOS in opposite magnetic domains (spin-dependent-DOS). Due to the small width, the nanowires possess a magnetic structure composed of single domains instead of the spin spiral configuration. Several dislocation lines are highlighted in the nanowires, especially in the dI/dU -map of figure 6.15 (b), providing certain growth tendency along their direction; however, it is not certain that this influences the magnetic structure of the nanowires.

The energy dependence (bias voltage) on magnetic imaging has been clearly demonstrated, but with the purpose to have a complete understating of its origin, single

point spectra were taken on magnetic domains with opposite magnetization, as is indicated with the blue points in figure 6.15 (c). The single point spectra are shown in figure 6.15 (e). For identification of each curve, the opposite magnetic domains are called “up” and “down” respectively. The first aspect to mention is that both curves share the same characteristics, in terms of shoulders and valleys, which are consistent with the DOS of the second layer of iron on W(110) [175].

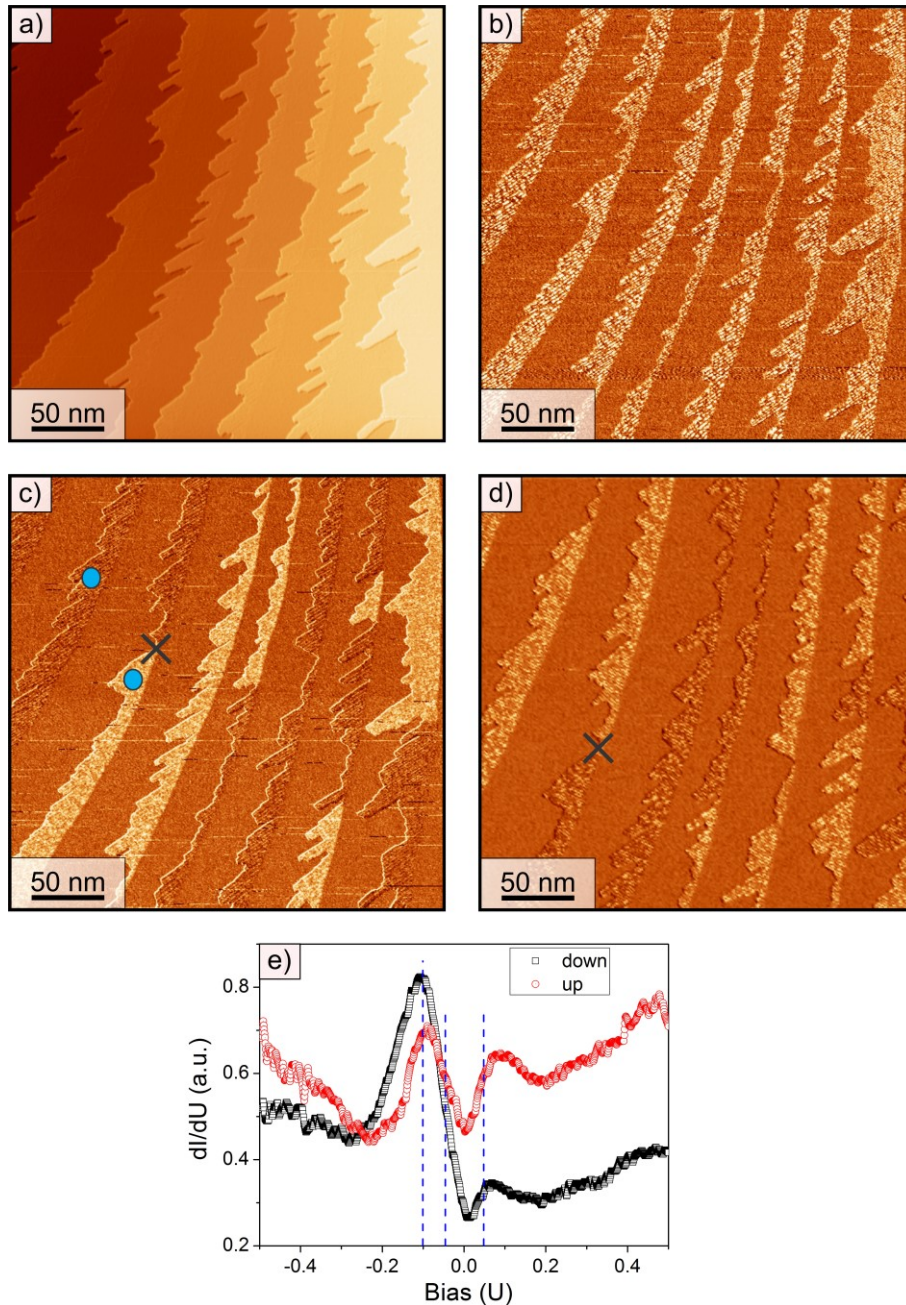


Figure 6.15: 1.4 ML of Fe on W(110) measured with an iron-coated tungsten tip. (a) STM topographic image ($I = 300$ pA, $U = 50$ mV, $T = 38$ K), (b) dI/dU -map @ $U = -50$

mV ($U_{mod} = 20$ mV, $f_{mod} = 3$ KHz), (c) dI/dU -map @ $U = +50$ mV ($U_{mod} = 20$ mV, $f_{mod} = 3$ KHz), (d) dI/dU -map @ $U = -100$ mV ($U_{mod} = 20$ mV, $f_{mod} = 3$ KHz), (e) spin-dependent single point spectra taken at the blue points in figure (c) and averaged over 50 measurements (stabilization conditions: $I = 300$ pA, $U = 500$ mV, $T = 38$ K). Dashed blue lines in (e) indicate the bias voltages of +50 mV, -50 mV and -100 mV respectively. Note that (d) shows an area that is shifted with respect to (c) because (d) corresponds to a different measurement where the field of view is different due to thermal drift. The black crosses indicate two equivalent points in (c) and (d).

However, the crucial aspect comparing both curves is the difference in the intensity for specific energy values, attributed to the spin-polarized-DOS. Now with this information, it is possible to clearly identify the energies where magnetic domains of the iron nanowires are visible (figures 6.15 (c) and (d)), as well as energies where non-magnetic contrast will appear (figure 6.15 (b)).

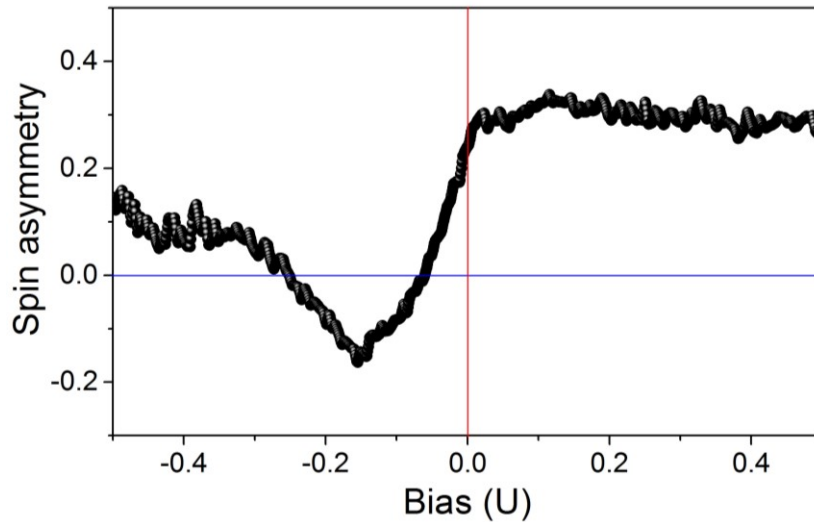


Figure 6.16: Spin asymmetry calculated from the spectroscopic data shown in figure 6.15 (e).

Furthermore, single point spectra on these two opposite magnetic domains provides the unique possibility to calculate the spin asymmetry as a function of energy (see figure 6.16), which otherwise, would be extremely difficult by using the contrast of the dI/dU -maps (revealing magnetic structures). One can recognize in figure 6.16 that the spin asymmetry variates from negative to positive values in a range between -0.5 V and +0.5 V. This implies that dI/dU -maps taken at positive values of spin asymmetry will reveal, with different intensities, the magnetic structures such as shown in figure 6.15 (c); however, dI/dU -maps taken at negative values of spin asymmetry, will reveal the

magnetic structures shown in figure 6.15 (d). Moreover, from the spin asymmetry calculation, one can measure that the highest magnetic contrast ($\sim 35\%$ of spin asymmetry) for this sample is found at $+120$ mV, in reasonable agreement with former studies [29] and close to the result in figure 6.15 (c). This shows us how SP-STM reveals the magnetic structure of a sample depicting different polarization directions as a function of energy due to the energy dependence of the spin-polarized-DOS. It additionally suggests that the spectroscopy data on magnetic structures is crucial information, which will provide clear hints of magnetic contrast. Thus, it is very important to consider the spin asymmetry of the magnetic system from the very beginning, in order to rationally approach unknown magnetic structures by using SP-STM.

Chromium bulk tips for magnetic imaging: One problem of ferromagnetic tips in order to investigate novel materials such as strongly correlated systems is their high stray field, which might interact considerably with the sample. Therefore, the development of functional antiferromagnetic tips is highly desired. The first attempt to implement chromium bulk tips in the SP-STM experiments at the IFW-Dresden is presented in figure 6.17. The preparation of bulk chromium tips was carried out as was explained in chapter 4. By using a sample of 1.2 ML of iron on W(110) (see the topography in figure 6.17 (a)), it is possible to discern a contrast in the iron wetting layer in the dI/dU -maps (see figures 6.17 (b, c, d)). As one can see in figure 6.17 (b), the contrast is not high, and in the case of figures (c,d), the contrast is even lower due to sample/tip degradation after 12 hours of measurements. Therefore, in order to evaluate the asymmetry in this sample, the dI/dU signal was statistically analyzed along the white arrow in figure 6.17 (b), which touches both the bright and the dark characteristic regions. 420 dI/dU data were used to calculate an average value of the dI/dU signal on the dark region as well as on the bright one. The average values were 0.51 ($\varepsilon = 0.007$) and 0.75 ($\varepsilon = 0.01$) on the dark and bright region respectively (see figure 6.17 (e)). This results in an asymmetry of 0.19. This is consistent with a reasonably low contrast considering that chromium is an antiferromagnetic material which does not possess a high spin polarization, in comparison to iron. In any case, this asymmetry agrees with reported spin polarization of tunneling electrons from Cr-tips of about 20-22% [29]. Therefore, the contrast is likely of magnetic origin. In this case, the magnetic contrast would correspond to an in-plane sample/tip magnetic polarization, considering the assumption that the magnetic anisotropy lies in the sample surface for the first iron layer [176].

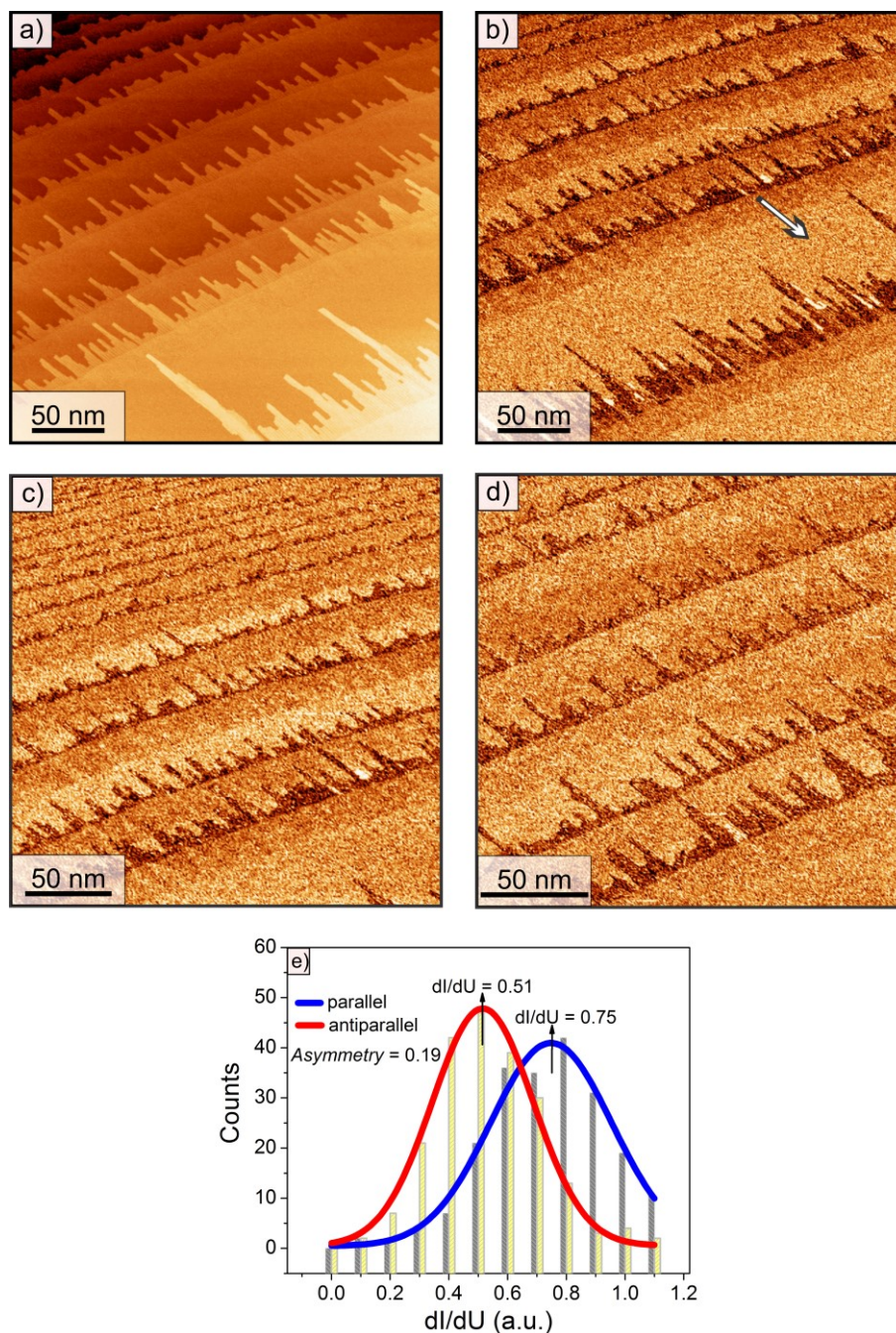


Figure 6.17: 1.2 ML of Fe on W(110) measured with a Cr-bulk tip. (a) STM topographic image ($I = 300$ pA, $U = -50$ mV, $T = 38$ K), (b, c, d) dI/dU -maps @ $U = -50$ mV ($U_{mod} = 20$ mV, $f_{mod} = 3$ KHz). (e) Spin asymmetry calculated by using 410 dI/dU -data along the black arrow in (b) and further statistical analysis with Gaussian fits, red curve represents data of antiparallel magnetic alignment of tip-sample and blue curve represents data of parallel alignment.

6.5 Conclusions

This chapter demonstrated the implementation of the spin-polarized STM technique at the IFW-Dresden. In order to do this, the well-known system Fe/W(110) and magnetic tips based on iron-coated tungsten tips as well as chromium bulk tips were chosen as a sample/probe system.

A systematic study of the iron growth on W(110) was presented, showing a wide range of structural configurations, whose topography was evaluated. From this, it was determined that the topography is influenced by the film coverage and sample preparation temperature. Among these configurations, nanoislands from one to three atomic layers, as well as nanowires of two atomic layers and 3D-islands were shown.

Magnetic imaging was performed on nanostructures of two atomic layers of iron. Magnetic domains with diverse shapes were revealed with iron-coated tungsten tips. These domains are expected to carry out-of-plane magnetization. Although iron coated tungsten tips are known in literature for showing most of the time in-plane magnetization, in our case such tips also showed out-of-plane magnetization. This was probably due to a canted magnetic moment. Furthermore, the energy dependence of magnetic images was corroborated considering the direct relation to the energy dependence of the spin-polarized-DOS.

With the purpose of evaluating the contrast in magnetic imaging, the coefficient of asymmetry in topography as well as in the dI/dU signal was calculated, providing a clear idea about the advantage of using dI/dU -maps in order to study magnetic structures. Preliminary results employing chromium bulk tips have been shown, which revealed a clear contrast in the dI/dU -signal, apparently of magnetic origin.

The present data show that the SP-STM technique has been successfully implemented at the IFW-Dresden, paving the way for further experiments in order to investigate novel quantum materials such as molecular magnets and strongly correlated electron systems.

7 Summary and outlook

Apart from an introduction to the scanning tunneling microscopy and spectroscopy (STM/STS) technique, and the used equipment (including efforts to repair an existing variable temperature scanning tunneling microscope), the thesis at hand contains two parts of successful experimental results using STM/STS:

- i) Investigations of macrocyclic paramagnetic complexes $[\text{Ni}_2\text{L}(\text{Hmba})]^+$ on gold.
- ii) First time implementation of spin-polarized scanning tunneling microscopy (SP-STM) at the IFW-Dresden, including studies on thin magnetic films.

The research interest in paramagnetic complexes arises from their potential use in spintronic devices, as one of the smallest thinkable building blocks for magnetic structures. Naturally, the understanding of the interface between such molecules and metallic electrodes is of crucial importance, before a functional unit based magnetic archetype can be designed. Therefore, as part of this thesis, exchange-coupled paramagnetic macrocyclic complexes $[\text{Ni}_2\text{L}(\text{Hmba})]^+$ deposited *via* 4-mercaptobenzoate ligands on Au(111) single crystals were analyzed, in terms of their structural and electronic properties. STM complemented with XPS data showed the successful gold surface-grafted paramagnetic macrocyclic complexes forming large monolayers with a height of about 1.5 nm. In light of the experimental data, the monolayers of $[\text{Ni}_2\text{L}(\text{Hmba})]\text{ClO}_4$ contain two apparently granular structures, one cationic structure corresponding to $[\text{Ni}_2\text{L}(\text{Hmba})]^+$ ions and another anionic one corresponding to the counterions ClO_4^- . No evidence of long or short range order of these structures was found. Further characterization reveals the tip-interaction with the monolayer due to field and current-induced desorption until the point of damage in some regions. Inhomogenous electrostatic forces, likely originated from defects in the molecular arrangement, probably contribute to the monolayer degradation. Single point spectroscopy indicates a gap in the molecular complexes of about 2.5 eV and a gap reduction in the anionic environment, becoming close to the tip-gold configuration. The height of the monolayers suggests that the molecular complexes are not perpendicularly anchored to the gold surface, but they are canted. Furthermore, the data suggest the formation of molecular agglomerates, likely by the high trend on such complexes to stack *via* $\text{CH}\cdots\pi$ and $\pi\cdots\pi$ interactions.

In addition to the morphologic and electronic investigations of such molecules, the exploration of their magnetic properties is of at most interest. The extension of STM by spin sensitivity (so-called spin-polarized STM, SP-STM) provides a promising approach

towards such studies. The experimentally challenging implementation of SP-STM at the IFW-Dresden included: i) a systematic study of the iron growth on a W(110) crystal, from sub-monolayers to multilayers and ii) the use of iron nanostructures of two atomic layers and iron-coated tungsten tips to probe the spin-polarized electron tunneling. The data showed a wide range of structural configurations depending mainly on the film coverage and sample preparation temperature. The obtained configurations were: nanoislands from one to three atomic layers, nanowires of two atomic layers and 3D-islands. Subsequent to the well-understanding of the iron growth, the experiments were focused on revealing, for the first time at the IFW-Dresden, the magnetic inner structure of iron nanostructures. Magnetic imaging was performed on nanostructures of two atomic layers of iron, revealing magnetic domains with diverse shapes. These domains are expected to carry out-of-plane magnetization. Furthermore, the energy dependence of magnetic images was corroborated, considering the direct relation to the energy dependence of the spin-polarized-DOS. With the purpose of evaluating the contrast in magnetic imaging, the coefficient of asymmetry in topography as well as in the dI/dU signal was calculated, providing a clear understanding about the advantage of using dI/dU -maps in order to study magnetic structures. Preliminary results employing polycrystalline chromium bulk tips have been shown, which revealed a clear contrast in the dI/dU signal, apparently of magnetic origin.

This thesis all together contributes to the foundation of a new class of future experiments at the IFW-Dresden, i.e. i) the systematic investigation of *ex-situ* growth of self-assembled monolayers of magnetic molecules by means of SP-STM, and ii) the application of SP-STM to other interesting magnetic systems such as correlated electron systems.

Bibliography

- [1] J. Wolfe, *The Industrial Revolution (Age of Revolution)* (Britannica-Educational Publishing, 2015).
- [2] J. D. Bernal, *Science and Industry in the Nineteenth Century* (Indiana University Press, 1970).
- [3] R. Feynman, *Caltech Eng. Sci.* **23:5**, 22 (1960).
- [4] P. Moriarty, *Reports Prog. Phys.* **64**, 297 (2001).
- [5] K. D. Sattler, editor, *Handbook of Nanophysics: Nanoparticles and Quantum Dots* (CRC Press, 2011).
- [6] M. A. Reed, J. N. Randall, R. J. Aggarwal, R. J. Matyi, T. M. Moore, and A. E. Wetsel, *Phys. Rev. Lett.* **60**, 535 (1988).
- [7] S. Iijima, *Nature* **354**, 56 (1991).
- [8] C. Vericat, M. E. Vela, G. Benitez, P. Carro, and R. C. Salvarezza, *Chem. Soc. Rev.* **39**, 1805 (2010).
- [9] V. J. Benavides, C. D. Salazar, M. E. Espitia, D. M. Devia, and A. Devia, *Phys. Scr.* **T131**, 014021 (2008).
- [10] D. T. Thompson, *Nano Today* **2**, 40 (2007).
- [11] Y. Q. He, S. P. Liu, L. Kong, and Z. F. Liu, *Spectrochim. Acta Part A Mol. Biomol. Spectrosc.* **61**, 2861 (2005).
- [12] X. Huang and M. A. El-Sayed, *J. Adv. Res.* **1**, 13 (2010).
- [13] F. J. Himpsel, J. E. Ortega, G. J. Mankey, and R. F. Willis, *Adv. Phys.* **47**, 511 (1998).
- [14] C. L. Dennis, R. P. Borges, L. D. Buda, U. Ebels, J. F. Gregg, M. Hehn, E. Jouguelet, K. Ounadjela, I. Petej, I. L. Prejbeanu, and M. J. Thornton, *J. Phys. Condens. Matter* **14**, R1175 (2002).
- [15] A. Caneschi, D. Gatteschi, and F. Totti, *Coord. Chem. Rev.* **289-290**, 357 (2015).
- [16] L. Bogani and W. Wernsdorfer, *Nat. Mater.* **7**, 179 (2008).
- [17] M. N. Leuenberger and D. Loss, *Nature* **410**, 789 (2001).
- [18] S. Hill, R. S. Edwards, N. Aliaga-Alcalde, and G. Christou, *Science* **302**, 1015 (2003).
- [19] D. Gatteschi, L. Bogani, A. Cornia, M. Mannini, L. Sorace, and R. Sessoli, *Solid State Sci.* **10**, 1701 (2008).
- [20] A. Cornia, A. Costantino, A. Fabretti, L. Zobbi, A. Caneschi, D. Gatteschi, M.

- Mannini, and R. Sessoli, *Single-Molecule Magnets and Related Phenomena* (Springer, 2006).
- [21] D. Gatteschi, R. Sessoli, and J. Villain, *Molecular Nanomagnets* (Oxford University Press, 2006).
- [22] R. Sessoli, H. Tsai, A. Schake, S. Wang, J. Vincent, K. Folting, D. Gatteschi, G. Christou, and D. Hendrickson, *J. Am. Chem. Soc.* **115**, 1804 (1993).
- [23] P. Lin, T. J. Burchell, L. Ungur, L. F. Chibotaru, W. Wernsdorfer, and M. Murugesu, *Angew. Chemie - Int. Ed.* **48**, 9489 (2009).
- [24] R. J. Blagg, C. A. Muryn, E. J. L. McInnes, F. Tuna, and R. E. P. Winpenny, *Angew. Chemie - Int. Ed.* **50**, 6530 (2011).
- [25] N. Ishikawa, M. Sugita, T. Ishikawa, S. Koshihara, and Y. Kaizu, *J. Am. Chem. Soc.* **125**, 8694 (2003).
- [26] N. Grumbach, A. Barla, L. Joly, B. Donnio, G. Rogez, E. Terazzi, J. Kappler, and J. Gallani, *Eur. Phys. J. B* **73**, 103 (2010).
- [27] R. Wiesendanger, *Scanning Probe Microscopy and Spectroscopy* (Cambridge University Press, 1998).
- [28] C. J. Chen, *Introduction to Scanning Tunneling Microscopy* (Oxford University Press, New York, 1993).
- [29] R. Wiesendanger, *Rev. Mod. Phys.* **81**, 1495 (2009).
- [30] M. Bode, *Chimia (Aarau)*. **66**, 56 (2012).
- [31] G. Binnig and H. Rohrer, *Surf. Sci.* **126**, 236 (1983).
- [32] G. Binnig, H. Rohrer, C. Gerber, and E. Weibel, *Phys. Rev. Lett.* **49**, 57 (1982).
- [33] G. Binnig and H. Rohrer, *Rev. Mod. Phys.* **59**, 615 (1987).
- [34] D. M. Eigler and E. K. Schweizer, *Nature* **344**, 524 (1990).
- [35] M. F. Crommie, C. P. Lutz, and D. M. Eigler, *Science* **262**, 218 (1993).
- [36] D. T. Pierce, *Phys. Scr.* **38**, 291 (1988).
- [37] A. A. Minakov and I. V. Shvets, *Surf. Sci.* **236**, L377 (1990).
- [38] R. Wiesendanger, H.-J. Güntherodt, G. Güntherodt, R. Gambino, and R. Ruf, *Phys. Rev. Lett.* **65**, 247 (1990).
- [39] M. Enayat, Z. Sun, U. R. Singh, R. Aluru, S. Schmaus, A. Yaresko, Y. Liu, C. Lin, V. Tsurkan, A. Loidl, and P. Wahl, *Science* **345**, 653 (2014).
- [40] J. E. Hoffman, A Search for Alternative Electronic Order in the High Temperature Superconductor $\text{Bi}_2\text{Sr}_2\text{CaCu}_2\text{O}_{8+d}$ by Scanning Tunneling Microscopy, Ph.D. Thesis, University of California, Berkeley, 2001.
- [41] C. Cohen-Tannoudji, B. Diu, and F. Laloe, *Quantum Mechanics, Volume 1* (Wiley, 1977).
- [42] D. J. Griffiths, *Introduction to Quantum Mechanics*, second (Pearson Prentice Hall, 2005).

-
- [43] J. Bardeen, Phys. Rev. Lett. **6**, 57 (1961).
- [44] J. Tersoff and D. Hamann, Phys. Rev. Lett. **50**, 1998 (1983).
- [45] J. Tersoff and D. R. Hamann, Phys. Rev. B **31**, 805 (1985).
- [46] A. Stroscio and W. Kaiser, editors, *Scanning Tunneling Microscopy* (ACADEMIC PRESS, INC, 1993).
- [47] C. J. Chen, Phys. Rev. Lett. **65**, 448 (1990).
- [48] K. von Bergmann, Iron Nanostructures Studied by Spin-Polarised Scanning Tunneling Microscopy, Ph.D. Thesis, Hamburg University, 2004.
- [49] M. Scheffler, L. Smykalla, D. Baumann, R. Schlegel, T. Hänke, M. Toader, B. Büchner, M. Hietschold, and C. Hess, Surf. Sci. **608**, 55 (2013).
- [50] R. Schlegel, T. Hänke, D. Baumann, M. Kaiser, P. K. Nag, R. Voigtländer, D. Lindackers, B. Büchner, and C. Hess, Rev. Sci. Instrum. **85**, 013706 (2014).
- [51] D. Baumann, Aufbau Eines Ultrahochauflösenden Tieftemperatur-Rastertunnelmikroskops, Dissertation, Technische Universität Dresden, 2011.
- [52] C. Iacovita, Spin - Dependent Tunneling into Single Cobalt - Phthalocyanine Molecules, Ph.D. Thesis, Université de Strasbourg, 2009.
- [53] A. M. Russell and D. A. Torchia, Rev. Sci. Instrum. **33**, 442 (1962).
- [54] www.thinksrs.com (2015).
- [55] I. Wang, J. Park, S. Seo, Y. Shin, J. Shin, M. Lee, Y. Jo, and H. Kim, J. Korean Phys. Soc. **45**, 1347 (2004).
- [56] T. Hänke, A New Variable-Temperature Scanning Tunneling Microscope and Temperature-Dependent Spin-Polarized Scanning Tunneling Spectroscopy on the Cr (001) Surface, Ph.D. Thesis, Hamburg University, 2005.
- [57] P. Levy, S. Zhang, and A. Fert, Phys. Rev. Lett. **65**, 1643 (1990).
- [58] J. C. Slonczewski, Phys. Rev. B **39**, 6995 (1989).
- [59] M. Bode, S. Heinze, A. Kubetzka, O. Pietzsch, X. Nie, G. Bihlmayer, S. Blügel, and R. Wiesendanger, Phys. Rev. Lett. **89**, 237205 (2002).
- [60] S. Heinze, M. Bode, A. Kubetzka, O. Pietzsch, X. Nie, S. Blügel, and R. Wiesendanger, Science **288**, 1805 (2000).
- [61] M. Bode, Reports Prog. Phys. **66**, 523 (2003).
- [62] D. Wortmann, S. Heinze, P. Kurz, G. Bihlmayer, and S. Blügel, Phys. Rev. Lett. **86**, 4132 (2001).
- [63] R. Wiesendanger, *Scanning Probe Microscopy and Spectroscopy* (Cambridge University Press, 1994).
- [64] www.eblproducts.com (2015).
- [65] S. Schimmel, Aufbau Eines Tieftemperatur Rastertunnelmikroskops, Bachelorarbeit, Westsächsische Hochschule Zwickau, 2014.

- [66] www.scientaomicron.com (2015).
- [67] D. Bombor, Konstruktion Eines Rastertunnelmikroskops Für Variable Temperaturen Und Oberflächenuntersuchungen an Supraleitenden Eisenpniktiden, Diplomarbeit, Technische Universität Dresden, 2009.
- [68] M. Scheffler, Aufbau Eines Rastertunnelmikroskops Und Untersuchung von Magnetischen Molekülen, Diplomarbeit, Technische Universität Dresden, 2011.
- [69] www.epotek.com (2015).
- [70] www.janis.com (2015).
- [71] P. Delhaes, *Graphite and Precursors* (Gordon and Breach Science Publishers, 2000).
- [72] www.goodfellow.com (2015).
- [73] D. D. L. Chung, *J. Mater. Sci.* **37**, 1475 (2002).
- [74] R. V. Lapshin, *Rev. Sci. Instrum.* **69**, 3268 (1998).
- [75] S. Ernst, Optimisation of the Preparation Process for Tips Used in Scanning Tunneling Microscopy, Master Thesis, Technische Universität Dresden, 2006.
- [76] R. Wiesendanger and H.-J. Güntherodt, *Scanning Tunneling Microscopy III*, 2nd ed. (Springer, 1996).
- [77] M. Kuwabara, D. R. Clarke, and D. a. Smith, *Appl. Phys. Lett.* **56**, 2396 (1990).
- [78] Z. Y. Rong and P. Kuiper, *Phys. Rev. B* **48**, 17427 (1993).
- [79] www.mateck.de (2015).
- [80] M. H. Dishner, M. M. Ivey, S. Gorer, J. C. Hemminger, and F. J. Feher, *J. Vac. Sci. Technol. A* **16**, 3295 (1998).
- [81] C. Nogues and M. Wanunu, *Surf. Sci.* **573**, L383 (2004).
- [82] M. E. Lauer, R. Jungmann, J. H. Kindt, S. Magonov, J. H. Fuhrhop, E. Oroudjev, and H. G. Hansma, *Langmuir* **23**, 5459 (2007).
- [83] Y. L. Cai, J. Song, S. Bao, P. He, F. Hu, and H. Zhang, *Chem. Phys. Lett.* **609**, 142 (2014).
- [84] N. Takeuchi, C. T. Chan, and K. M. Ho, *Phys. Rev. B* **43**, 13889 (1991).
- [85] J. V. Barth, H. Brune, G. Ertl, and R. J. Behm, *Phys. Rev. B* **42**, 9307 (1990).
- [86] F. Hanke and J. Björk, *Phys. Rev. B* **87**, 235422 (2013).
- [87] M. Bode, R. Pascal, and R. Wiesendanger, *Surf. Sci.* **344**, 185 (1995).
- [88] M. Bode, Strukturelle Und Lokale Elektronische Eigenschsften Ultradünner Eisenfilme Auf W(110), Dissertation, Universität Hamburg, 1996.
- [89] D. Bonnell, editor , *Scanning Tunneling Microscopy and Spectroscopy, Theory, Techniques and Applications* (Wiley, 1993).
- [90] H. Ness and F. Gautier, *J. Physics. Condens. Matter* **7**, 6625 (1995).
- [91] C. Bai, *Scanning Tunneling Microscopy and Its Application*, Second (Springer, 2000).

- [92] J. P. Ibe, P. P. Bey Jr, S. L. Brandow, R. A. Brizzolara, N. A. Burnham, D. P. DiLella, K. P. Lee, C. R. K. Marrian, and R. J. Colton, *J. Vac. Sci. Technol. A* **8**, 3570 (1990).
- [93] B. Hacker, A. Hillebrand, T. Hartmann, and R. Guckenberger, *Ultramicroscopy* **42-44**, 1514 (1992).
- [94] I. Ekvall, E. Wahlstr, D. Claesson, H. Olin, and E. Olsson, *Meas. Sci. Technol.* **10**, 11 (1999).
- [95] A. H. Sørensen, U. Hvid, M. W. Mortensen, and K. A. Mørch, *Rev. Sci. Instrum.* **70**, 3059 (1999).
- [96] J. Garnaes, F. Kragh, K. A. Mørch, and A. R. Thölén, *J. Vac. Sci. Technol. A* **8**, 441 (1990).
- [97] Nanosurf, *Operating Instructions: easyScan 2 STM Version 1.6* (Nanosurf, 2007).
- [98] B. Bhushan, editor, *Handbook of Nanotechnology* (Springer, 2010).
- [99] A. Li Bassi, C. S. Casari, D. Cattaneo, F. Donati, S. Foglio, M. Passoni, C. E. Bottani, P. Biagioni, A. Brambilla, M. Finazzi, F. Ciccacci, and L. Duò, *Appl. Phys. Lett.* **91**, 173120 (2007).
- [100] A. Schlenhoff, S. Krause, G. Herzog, and R. Wiesendanger, *Appl. Phys. Lett.* **97**, (2010).
- [101] M. Corbetta, S. Ouazi, J. Borme, Y. Nahas, F. Donati, H. Oka, S. Wedekind, D. Sander, and J. Kirschner, *Jpn. J. Appl. Phys.* **51**, 030208 (2012).
- [102] A. R. Rocha, V. M. García-Suárez, S. W. Bailey, C. J. Lambert, J. Ferrer, and S. Sanvito, *Nat. Mater.* **4**, 335 (2005).
- [103] J. M. Seminario, *Nat. Mater.* **4**, 111 (2005).
- [104] A. Cornia, M. Mannini, P. Sainctavit, and R. Sessoli, *Chem. Soc. Rev.* **40**, 3076 (2011).
- [105] J. Gómez-Segura, J. Veciana, and D. Ruiz-Molina, *Chem. Commun.* 3699 (2007).
- [106] M. Cavallini, M. Facchini, C. Albonetti, and F. Biscarini, *Phys. Chem. Chem. Phys.* **10**, 784 (2008).
- [107] K. Szaciłowski, *Chem. Rev.* **108**, 3481 (2008).
- [108] M. Urdampilleta, S. Klyatskaya, J.-P. Cleuziou, M. Ruben, and W. Wernsdorfer, *Nat. Mater.* **10**, 502 (2011).
- [109] F. Troiani and M. Affronte, *Chem. Soc. Rev.* **40**, 3119 (2011).
- [110] V. Meded, A. Bagrets, K. Fink, R. Chandrasekar, M. Ruben, F. Evers, A. Bernard-Mantel, J. S. Seldenthuis, A. Beukman, and H. S. J. Van Der Zant, *Phys. Rev. B* **83**, 245415 (2011).
- [111] T. Komeda, H. Isshiki, J. Liu, Y.-F. Zhang, N. Lorente, K. Katoh, B. K. Breedlove, and M. Yamashita, *Nat. Commun.* **2:217**, 1 (2011).

- [112] D. E. Barlow, L. Scudiero, and K. W. Hipps, *Langmuir* **20**, 4413 (2004).
- [113] C. Iacovita, M. V. Rastei, B. W. Heinrich, T. Brumme, J. Kortus, L. Limot, and J. P. Bucher, *Phys. Rev. Lett.* **101**, 116602 (2008).
- [114] C. Wäckerlin, D. Chylarecka, A. Kleibert, K. Müller, C. Iacovita, F. Nolting, T. A. Jung, and N. Ballav, *Nat. Commun.* **1:61**, 1 (2010).
- [115] A. Scheybal, T. Ramsvik, R. Bertschinger, M. Putero, F. Nolting, and T. A. Jung, *Chem. Phys. Lett.* **411**, 214 (2005).
- [116] H. Wende, M. Bernien, J. Luo, C. Sorg, N. Ponpandian, J. Kurde, J. Miguel, M. Piantek, X. Xu, P. Eckhold, W. Kuch, K. Baberschke, P. M. Panchmatia, B. Sanyal, P. M. Oppeneer, and O. Eriksson, *Nat. Mater.* **6**, 516 (2007).
- [117] M. Bernien, J. Miguel, C. Weis, M. E. Ali, J. Kurde, B. Krumme, P. M. Panchmatia, B. Sanyal, M. Piantek, P. Srivastava, K. Baberschke, P. M. Oppeneer, O. Eriksson, W. Kuch, and H. Wende, *Phys. Rev. Lett.* **102**, 047202 (2009).
- [118] P. M. Oppeneer, P. M. Panchmatia, B. Sanyal, O. Eriksson, and M. E. Ali, *Prog. Surf. Sci.* **84**, 18 (2009).
- [119] A. Cornia, A. C. Fabretti, M. Pacchioni, L. Zobbi, D. Bonacchi, A. Caneschi, D. Gatteschi, R. Biagi, U. Del Pennino, V. De Renzi, L. Gurevich, and H. S. J. Van der Zant, *Angew. Chemie* **115**, 1683 (2003).
- [120] M. Mannini, F. Pineider, P. Sainctavit, C. Danieli, E. Otero, C. Sciancalepore, A. M. Talarico, M. Arrio, A. Cornia, D. Gatteschi, and R. Sessoli, *Nat. Mater.* **8**, 194 (2009).
- [121] M. S. Alam, M. Stocker, K. Gieb, P. Müller, M. Haryono, K. Student, and A. Grohmann, *Angew. Chemie - Int. Ed.* **49**, 1159 (2010).
- [122] W. Hieringer, K. Flechtner, A. Kretschmann, K. Seufert, W. Auwärter, J. V Barth, A. Görling, H. P. Steinrück, and J. M. Gottfried, *J. Am. Chem. Soc.* **133**, 6206 (2011).
- [123] T. Choi, S. Bedwani, A. Rochefort, C. Y. Chen, A. J. Epstein, and J. A. Gupta, *Nano Lett.* **10**, 4175 (2010).
- [124] T. G. Gopakumar, F. Matino, H. Naggert, A. Bannwarth, F. Tuczek, and R. Berndt, *Angew. Chemie - Int. Ed.* **51**, 6262 (2012).
- [125] H. Soyer, C. Mingotaud, M.-L. Boillot, and P. Delhaes, *Thin Solid Films* **327-329**, 435 (1998).
- [126] A. B. Gaspar, M. Seredyuk, and P. Gütllich, *Coord. Chem. Rev.* **253**, 2399 (2009).
- [127] G. Agustí, S. Cobo, A. B. Gaspar, G. Molnár, N. O. Moussa, P. Á. Szilágyi, V. Pálfi, C. Vieu, C. M. Muñoz, J. A. Real, and A. Bousseksou, *Chem. Mater.* **20**, 6721 (2008).
- [128] I. Boldog, A. B. Gaspar, V. Martínez, P. Pardo-Ibañez, V. Ksenofontov, A. Bhattacharjee, P. Gütllich, and J. A. Real, *Angew. Chemie - Int. Ed.* **47**, 6433 (2008).

- [129] F. Volatron, L. Catala, E. Rivière, A. Gloter, O. Stéphan, and T. Mallah, *Inorg. Chem.* **47**, 6584 (2008).
- [130] C. Rajadurai, F. Schramm, S. Brink, O. Fuhr, M. Ghafari, R. Kruk, and M. Ruben, *Inorg. Chem.* **45**, 10019 (2006).
- [131] Y. Bodenthin, U. Pietsch, H. Möhwald, and D. G. Kurth, *J. Am. Chem. Soc.* **127**, 3110 (2005).
- [132] L. Margheriti, M. Mannini, L. Sorace, L. Gorini, D. Gatteschi, A. Caneschi, D. Chiappe, R. Moroni, F. B. De Mongeot, A. Cornia, F. M. Piras, A. Magnani, and R. Sessoli, *Small* **5**, 1460 (2009).
- [133] J. C. Love, L. A. Estroff, J. K. Kriebel, R. G. Nuzzo, and G. M. Whitesides, *Chem. Rev.* **105**, 1103 (2005).
- [134] A. Ulman, *Chem. Rev.* **96**, 1533 (1996).
- [135] L. Zobbi, M. Mannini, M. Pacchioni, G. Chastanet, D. Bonacchi, C. Zanardi, R. Biagi, U. Del Pennino, D. Gatteschi, A. Cornia, and R. Sessoli, *Chem. Commun.* 1640 (2005).
- [136] M. Mannini, F. Pineider, C. Danieli, F. Totti, L. Sorace, P. Sainctavit, M.-A. Arrio, E. Otero, L. Joly, J. C. Cezar, A. Cornia, and R. Sessoli, *Nature* **468**, 417 (2010).
- [137] M. Pacchioni, A. Cornia, A. C. Fabretti, L. Zobbi, D. Bonacchi, A. Caneschi, G. Chastanet, D. Gatteschi, and R. Sessoli, *Chem. Commun.* 2604 (2004).
- [138] D. K. Aswal, S. Lenfant, D. Guerin, J. V Yakhmi, and D. Vuillaume, *Anal. Chim. Acta* **568**, 84 (2006).
- [139] H. Ma, O. Acton, D. Hutchins, N. Cernetic, and A. Jen, *Phys. Chem. Chem. Phys.* **14**, 14110 (2012).
- [140] J. Lach, A. Jeremies, D. Breite, B. Abel, B. Mahns, M. Knupfer, V. Matulis, O. A. Ivashkevich, and B. Kersting, *Inorg. Chem.* **53**, 10825 (2014).
- [141] Y. Journaux, T. Glaser, G. Steinfeld, V. Lozan, and B. Kersting, *Dalt. Trans.* 1738 (2006).
- [142] T. Young, *Phil. Trans. R. Soc. Lond.* **95**, 65 (1805).
- [143] B. S. Sumerlin, A. B. Lowe, P. a Stroud, P. Zhang, M. W. Urban, and C. L. McCormick, *Langmuir* **19**, 5559 (2003).
- [144] J. W. Ciszek, M. P. Stewart, and J. M. Tour, *J. Am. Chem. Soc.* **126**, 13172 (2004).
- [145] P. van der Heide, *X-Ray Photoelectron Spectroscopy: An Introduction to Principles and Practices* (Wiley, 2011).
- [146] S. Hüfner, *Photoelectron Spectroscopy: Principles and Applications* (Springer Science & Business Media, 2013).
- [147] R. G. Copperthwaite and J. Lloyd, *Dalt. Trans.* **11**, 1117 (1977).
- [148] J. Chastain and R. C. King, *Handbook of X-Ray Photoelectron Spectroscopy: A*

Reference Book of Standard Spectra for Identification and Interpretation of XPS Data
(Eden Prairie, MN: Perkin-Elmer, 1992).

- [149] C. M. Whelan, M. R. Smyth, C. J. Barnes, N. M. Brown, and C. A. Anderson, *Appl. Surf. Sci.* **134**(1), 144 (1998).
- [150] D. G. Castner, K. Hinds, and D. W. Grainger, *Langmuir* **12**(21), 5083 (1996).
- [151] S. A. Best, P. Brant, R. D. Feltham, T. B. Rauchfuss, D. M. Roundhill, and R. A. Walton, *Inorg. Chem.* **16**(8), 1976 (1977).
- [152] K. A. Lee, V. Lozan, J. Langford, and B. Kersting, *Dalt. Trans.* 7481 (2009).
- [153] A. M. Emmanuel, R. K. Castellano, and F. Diederich, *Angew. Chemie - Int. Ed.* **42**, 1210 (2003).
- [154] S. Käss and B. Kersting, *Eur. J. Inorg. Chemistry* 2389 (2012).
- [155] A. H. Al Mamun, S. B. Son, and J. R. Hahn, *Bull. Korean Chem. Soc.* **32**, 281 (2011).
- [156] G. Yang, N. A. Amro, and G. Liu, *Proc. SPIE* **5220**, 52 (2003).
- [157] F. Mirjani, J. M. Thijssen, G. M. Whitesides, and M. A. Ratner, *ACS Nano* **8**, 12428 (2014).
- [158] M. Bode, a. Kubetzka, O. Pietzsch, and R. Wiesendanger, *Appl. Phys. A Mater. Sci. Process.* **72**, 149 (2001).
- [159] C. Kittel, *Introduction to Solid State Physics*, 8th ed. (Wiley, 2005).
- [160] H. Bethge, D. Heuer, C. Jensen, K. Reshöft, and U. Köhler, *Surf. Sci.* **331-333**, 878 (1995).
- [161] H. J. Elmers, J. Hauschild, H. Höche, and U. Gradmann, *Phys. Rev. Lett.* **73**, 898 (1994).
- [162] R. Kurzawa, K.-P. Kämper, W. Schmitt, and G. Güntherodt, *Solid State Commun.* **60**, 777 (1986).
- [163] O. Hjortstam, K. Baberschke, J. M. Wills, B. Johansson, and O. Eriksson, *Phys. Rev. B* **55**, 15026 (1997).
- [164] H. Fritzsche, J. Kohlhepp, and U. Gradmann, *Phys. Rev. B* **51**, 15933 (1995).
- [165] H. . Elmers, *J. Magn. Magn. Mater.* **185**, 274 (1998).
- [166] H. J. Elmers, *Phys. Rev. B* **59**, 3688 (1999).
- [167] H. J. Elmers, J. Hauschild, H. Fritzsche, G. Liu, U. Gradmann, and U. Köhler, *Phys. Rev. Lett.* **75**, 2031 (1995).
- [168] M. Bode, A. Kubetzka, S. Heinze, O. Pietzsch, R. Wiesendanger, M. Heide, X. Nie, G. Bihlmayer, and S. Blügel, *J. Phys. Condens. Matter* **15**, S679 (2003).
- [169] A. Kubetzka, O. Pietzsch, M. Bode, and R. Wiesendanger, *Phys. Rev. B* **63**, 1 (2001).
- [170] M. Bode, A. Wachowiak, J. Wiebe, A. Kubetzka, M. Morgenstern, and R. Wiesendanger, *Appl. Phys. Lett.* **84**, 948 (2004).

- [171] M. Bode, S. Krause, S. Heinze, and R. Wiesendanger, *Surf. Sci.* **601**, 3308 (2007).
- [172] M. S. J. Marshall and M. R. Castell, *Chem. Soc. Rev.* **43**, 2226 (2014).
- [173] A. Wachowiak, Aufbau Einer 300mK-Ultrahochvakuum-Rastertunnelmikroskopie-Anlage Mit 14 Tesla Magnet Und Spinpolarisierte Rastertunnelspektroskopie an Ferromagnetischen Fe-Inseln, Dissertation, Universität Hamburg, 2003.
- [174] P. Ferriani, C. Lazo, and S. Heinze, *Phys. Rev. B - Condens. Matter Mater. Phys.* **82**, 1 (2010).
- [175] M. Bode, a. Kubetzka, O. Pietzsch, and R. Wiesendanger, *Surf. Sci.* **514**, 135 (2002).
- [176] M. Pratzner, H. J. Elmers, M. Bode, O. Pietzsch, A. Kubetzka, and R. Wiesendanger, *Phys. Rev. Lett.* **87**, 127201 (2001).
- [177] M. Golecki, J. Lach, A. Jeremies, F. Lungwitz, M. Fronk, G. Salvan, D. R. T. Zahn, J. Park, Y. Krupskaya, V. Kataev, R. Klingeler, B. Büchner, B. Mahns, M. Knupfer, P. F. Siles, D. Grimm, O. G. Schmidt, A. Reis, W. R. Thiel, D. Breite, B. Abel, and B. Kersting, *Chem. - A Eur. J.* **19**, 7787 (2013).

Conferences

- 4th Scientific TMS (Towards Molecular Spintronics) workshop, Burgstädt, Germany (2012). Contribution: *STM/STS on magnetic organic molecules*.
- 5th Scientific TMS (Towards Molecular Spintronics) workshop, Chemnitz, Germany (2012). Contribution: *Scanning tunneling microscopy of self-assembled paramagnetic molecules on gold*.
- TMS (Towards Molecular Spintronics) Winterschool, Zakopane, Poland (2013). Contribution: *STM of self-assembled paramagnetic molecules and spin sensitive STM measurements on iron films*.
- Frühjahrstagung der Deutschen Physikalischen Gesellschaft, Regensburg, Germany (2013). Contribution: *Self-assembled monolayers of paramagnetic molecules on gold revealed by scanning tunneling microscopy*.
- 6th Scientific TMS (Towards Molecular Spintronics) workshop, Burgstädt, Germany (2013). Contribution: *STM of self-assembled paramagnetic molecules and spin-polarized STM measurements on iron films*.
- Frühjahrstagung der Deutschen Physikalischen Gesellschaft, Dresden, Germany (2014). Contribution: *STM investigations of iron thin films on W(110)*.
- 7th Scientific TMS (Towards Molecular Spintronics) workshop, Neukirchen/Pleiße, Germany (2014). Contribution: *SP-STM for investigations on magnetic molecules*.
- 8th Scientific TMS (Towards Molecular Spintronics) workshop, Burgstädt, Germany (2015). Contribution: *Spin-polarized scanning tunneling microscopy for investigations of magnetic molecules*.
- 9th Scientific TMS (Towards Molecular Spintronics) workshop, Burgstädt, Germany (2015). Contribution: *STM study of Au(111) surface-grafted macrocyclic complexes $[Ni_2L(Hmba)]^+$ via ambidentate ligands*.

Publication

- Christian Salazar, Jochen Lach, Florian Rückerl, Danny Baumann, Sebastian Schimmel, Martin Knupfer, Berthold Kersting, Bernd Büchner, and Christian Hess. *STM study of Au(111) surface-grafted paramagnetic macrocyclic complexes $[Ni_2L(Hmba)]^+$ via ambidentate ligands*. *Langmuir* **32**, 4464 (2016)

Acknowledgements

Without the contribution of many people and institutions, I would not be at this stage of my life. Therefore, I would like to express my deep gratitude to:

Prof. Bernd Büchner, who gave me the possibility to work at the Leibniz Institute for Solid State Research (IFF). I found an excellent scientific environment with unique experimental tools and highly qualified scientists.

Christian Hess, my supervisor, who supported me to conclude the doctoral work, although multiple experimental problems appeared in the path. His experience on science and as a group leader was a great support.

Prof. Berthold Kersting. His valuable knowledge and his friendly disposal to answer questions were very important for the successful investigations on molecular complexes.

Prof. Knupfer and Florian Ruckerl for the important contribution with measurements and analysis of the XPS data.

my colleagues of the STM group: Rico, Pranab, Sebastian, Tim, Danny, Martha, Ronny. We spent a lot of time of our lives together in the lab, I learned and enjoyed.

my colleagues of IFW-Dresden. It was a pleasure to share with you during the Ph.D.-seminars, conferences, workshops, lectures,...etc. A lot of interesting discussions not only on science, but also on life enriched me.

Towards Molecular Spintronics (TMS)-Research-Unit for the multidisciplinary academic environment and the economic support.

DAAD (Deutscher Akademischer Austausch Dienst) for the scholarship of doctoral studies and all the benefits.

IFW (Leibniz-Institute für Festkörper- und Werkstoffforschung Dresden) for all the scientific facilities, worthy of a world-class institution.

TUD (Technische Universität Dresden) for providing an excellent academic environment to the students.

My family: Nidia, Tomás, Milena, Maria for dreaming with me....

DAAD

Deutscher Akademischer Austauschdienst

